Design of a Small Fast Steering Mirror for Airborne and Aerospace Applications

by

Michael Thomas Boulet

B.S., Mechanical Engineering, Rensselaer Polytechnic Institute (2001)

Submitted to the Department of Mechanical Engineering
in partial fulfillment of the requirements for the degree of

Master of Science in Mechanical Engineering

at the

MASSACHUSETTS INSTITUTE OF TECHNOLOGY

June 2008

Author .....
Department of Mechanical Engineering
May 9, 2008

Certified by .....
David L. Trumper
Professor of Mechanical Engineering
Thesis Supervisor

Accepted by .....
Lallit Anand
Chairman, Department Committee on Graduate Students

This work was sponsored by the Unted States Air Force under Air Force Contract FA8721-05-C-002. Opinions, interpretations, conclusions and recommendations are those of the author and are not necessarily endorsed by the United States Government.

Design of a Small Fast Steering Mirror for Airborne and Aerospace Applications

by

Michael Thomas Boulet

Submitted to the Department of Mechanical Engineering
on May 9, 2008, in partial fulfillment of the
requirements for the degree of
Master of Science in Mechanical Engineering

Abstract

This thesis presents the analysis and design of a small advanced fast steering mirror (sAFSM) for airborne and aerospace platforms. The sAFSM provides feedback-controlled articulation of two rotational axes for precision optical pointing. The design, useful for both disturbance rejection and high-speed scanning applications, incorporates a flux steering actuator with a ring core magnetic configuration. The novel magnetic concept enables a dramatic size reduction compared with heritage systems. The moving armature is supported with a combination of elastomer sheets and active position control. Local angular and mirror-normal displacement is sensed with integrated capacitive sensors.

Analysis content includes specification of performance requirements based on a realistic deep-space laser communication mission, magnetic equivalent circuit and three-dimensional magnetostatic finite element analysis of the actuator, and a 3D structural optimization of the moving armature modal frequencies. The resulting design is one iteration removed from a flight-ready model. The sAFSM hardware is in fabrication, and anticipated performance exceeds $10\,^{\mathrm{krad}}/_{\mathrm{s}^2}$ angular acceleration, 10 mrad range, and 9 kHz closed-loop bandwidth.

Thesis Supervisor: David L. Trumper
Title: Professor of Mechanical Engineering

.

Acknowledgments

Many people have provided suggestions, support, and encouragement throughout my Master's degree effort. I owe them all my sincere gratitude.

Discussions with my thesis adviser, Professor David Trumper, led to the electromagnetic concept developed in this thesis. Professor Trumper's persistent encouragement to consider new ideas greatly improved the fast steering mirror design. I especially appreciate Professor Trumper's willingness to explain the principals and practices of precision machine design and electromagnetics, as I had very little experience with either subject at the outset of this project. Although I still can't match Professor Trumper's mastery or seemingly effortless recollection of the fields' concepts, I am now able to contribute to a discussion of the subjects with some degree of confidence.

Dan Kluk, a former graduate student, designed the AFSM prototype upon which much of this effort is based. The success of the AFSM is indicative of Kluk's talent and thoroughness as an engineer. Working with Kluk was always an enjoyable and productive experience. Professor Markus Zahn of MIT's EECS department and Alex Prengel with MIT IST were very helpful and responsive to my queries regarding MIT's available magnetic finite element analysis software. Leslie Regan in the MIT mechanical engineering graduate office has saved me from administrative jams on several occasions.

At Lincoln Laboratory, Ed Corbett and Bruce Bray, the leadership of the Control Systems Engineering Group, have been supportive since I began to pursue a Master's degree in late 2004. Ed and Bruce have arranged hardware development funding, attended application and progress meetings, and have repeatedly offered their encouragement. Jamie Burnside, my Lincoln thesis adviser, provided advice and data for modeling platform disturbances and made several beneficial design suggestions. Annmarie Gorton gave assistance with procurement and other administrative tasks, enabling me to concentrate on the technical issues. Jeff Connolly, Bob Gemma, Jeanne Clarke, and Joe Orender helped fabricate FSM parts and test equipment.

Jeanne's ability to manipulate and solder tiny thermistors is particularly appreciated. Al Pillsbury's insightful review of an early FSM mechanical design iteration resulted in a number of improvements. Mark Padula offered a number of helpful suggestions for modeling the FSM armature structure for modal analysis. Ron Skinner arranged the outside procurement of a large number of custom machined FSM metal parts.

I would also like to thank the Lincoln Scholars Committee and Roger Khazan, my LSP mentor, for their support.

Chris Aiello, a friend and fellow mechanical engineer from my undergraduate class, reviewed my detailed design drawings and gave constructive criticism of my amateur attempt at GD&T.

I am also thankful for my family's and in-law's long-distance support and understanding when I've had to miss holidays or dinners in order to work on my thesis project.

Finally, I would like to thank my wife Sarah. Sarah's support, encouragement, and patience have been amazing and invaluable over the past two years. I am forever grateful. LU2 100.

Contents

THIS PAGE INTENTIONALLY LEFT BLANK

List of Figures

List of Tables

THIS PAGE INTENTIONALLY LEFT BLANK

Chapter 1

Introduction

1.1 Fast Steering Mirrors

Although definitions vary between vendor product lines, a fast steering mirror (FSM) is generally considered to be a mirror with one or two rotational degrees of freedom that are controlled with high bandwidths and accelerations. The word "controlled" is key as articulated mirrors that simply resonate at their natural frequency are, for the purposes of this thesis, considered "scanners". The rotational degrees of freedom, frequently called tip and tilt in two axis FSMs, are usually limited in range from ± 5 to ± 100 mrad [$\pm 0.3°$ to $\pm 6°$]. Likewise, mirror sizes vary widely among implementations - from a few millimeters to tens of centimeters. This thesis is focused on small FSMs with diameters between 10 and 30 mm. The meaning of "fast" generally depends upon the size of the mirror. For large mirrors, "fast" might mean closed-loop bandwidth in the tens of hertz. But for smaller FSMs, like those considered in the thesis, "fast" bandwidths are typically greater-than 500 Hz and angular accelerations exceed $1000\,^{rad}/_{s^2}$. Lastly, fast steering mirrors have high pointing accuracies with resolutions commonly better-than 0.5% of full scale.

FSMs are employed in a wide variety of military, commercial, and research optical applications. Such applications could include LIDAR[1] beam pointing for autonomous vehicle navigation, aligning the collimated output of an astronomical telescope to an

[1] LIDAR : LIght Detection And Ranging, used to identify distances to a remote object

adaptive optics vibration isolation table, or long-range reconnaissance image stabilization. FSMs could even conceivably be used to produce an entertaining laser light show[2]. Free space optical communication beam pointing and disturbance rejection is a particularly important fast steering mirror application and is additionally discussed in Section 1.2.

Regardless of the application, fast steering mirrors perform one or a combination of three basic roles: scanning, offset pointing, and disturbance rejection. When scanning, an FSM tracks a precomputed and typically cyclic path. Examples of scanning paths include spirals, Lissajous curves, and raster patterns. Larry Hawe discusses scanning paths for the acquisition of free space optical communication signals in his 2006 Master's thesis[20]. Scanning frequently requires very high angular accelerations in order to complete the cyclic path as fast as possible. The offset pointing function maintains steady state or slowly changing pointing to some angle within the FSM's range. Lastly, the disturbance rejection role moves the beam to counteract undesirable motion within the optical path.

1.1.1 High Bandwidth Steering Mirror

Greg Loney, a former member of Lincoln Laboratory's technical staff, developed a High Bandwidth Steering Mirror (HBSM) in the early 1990's[25]. A photograph of an HBSM is shown in Figure 1-1. The HBSM mirror is suspended with a planar, spider-like metal flexure that constrains radial translation (perpendicular to the mirror normal direction) and torsional rotation (about the mirror normal) but is compliant in tip and tilt rotation and mirror normal translation. A long, thin, cylindrical metal flexure, not visible in the photograph, is attached to the back of the mirror structure and additionally constrains mirror normal translation. Thus, only the tip and tilt rotational degrees of freedom remain relatively compliant. A set of four Lorentz force, moving coil actuators are positioned in a square pattern behind the mirror. Opposite pairs of actuators are driven differentially to apply a torque to the mirror structure. Four inductive, i.e. eddy current, sensors provide mirror

[2]Laser light shows normally utilize a pair of single-axis galvanometers.

displacement signals to an analog controller designed by Professor James Roberge.

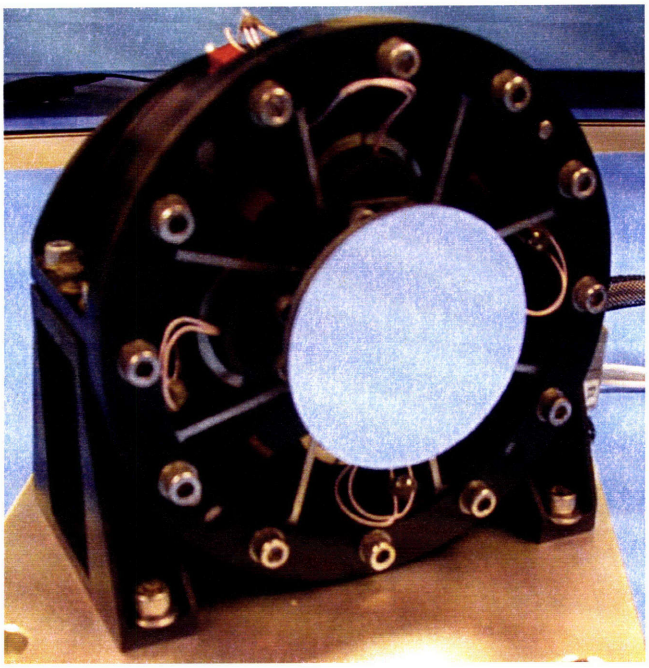

Figure 1-1: High Bandwidth Steering Mirror

Loney's technical reports claim that the HBSM achieves a closed-loop bandwidth of 10 kHz and peak accelerations of 13 $^{krad}/_{s^2}$. Hawe found, for the HBSM model studied in his thesis, that closed loop bandwidth was limited to 2.2 kHz with a moderately aggressive controller. The controlled bandwidth is limited by non-rigid modes in the mirror structure.

1.1.2 Advanced Fast Steering Mirror

In 2005, Professor David Trumper and Xiaodong Lu, then a PhD student, proposed a fast steering mirror concept based upon technologies developed for Lu's PhD project. Daniel Kluk, then a graduate student in Professor Trumper's Precision Motion Control Laboratory, flushed-out the concept into a hardware prototype for his Master's thesis[22]. Kluk named the design an Advanced Fast Steering Mirror (AFSM) to denote its advanced performance compared to the HBSM or commercially available fast steering mirrors. A photograph of Kluk's assembled prototype is shown in Figure 1-2.

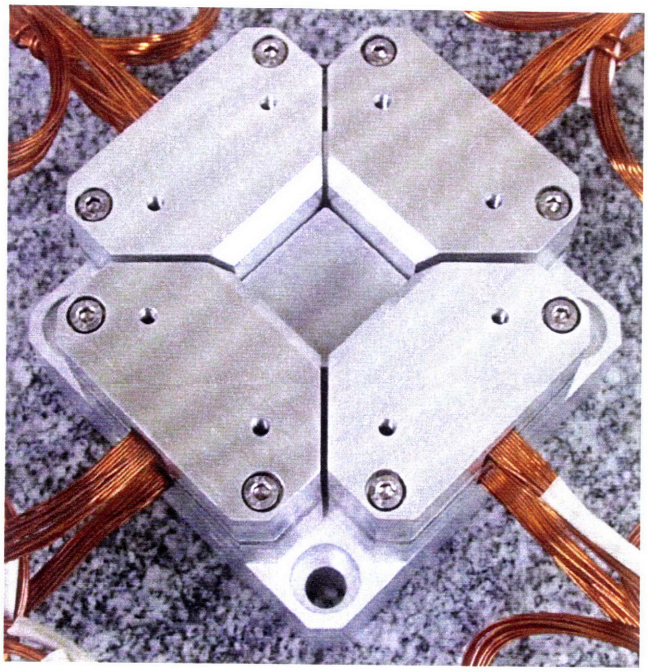

Figure 1-2: Advanced Fast Steering Mirror

The AFSM's actuators and flexure supports are discussed in detail in subsequent chapters with a brief introduction given here. The design incorporates four bias-linearized flux steering actuators. Compared with voice coil motors, flux steering actuators give higher force output per mass of copper wiring. Kluk's design utilizes rubber pads to provide radial rigidity and tip/tilt compliance in place of the planar flexure. Rubber bearings are advantageous because of their small size and inherent damping.

Kluk demonstrated closed-loop, -3 dB bandwidths approaching 10 kHz using optical position feedback and mirror angular accelerations surpassing 1×10^5 $^{rad}/_{s^2}$. While the AFSM's design proved overwhelmingly successful for a prototype, Kluk did encounter two difficulties. First, the rubber bearings were stiffer than expected due to preloading and ultimately limited the actuator's range to one-third of the desired extent. Secondly, an epoxy joint affixing the magnetic armature to the mirror base structure failed after a closed-loop instability drove the armature into a stator pole.

It is important to note that Kluk designed the AFSM as a proof-of-concept technology demonstrator. Thus, he made no attempt to minimize system size or mass, nor

did Kluk attempt to optimize its performance for any particular application scenario.

1.1.3 Small Advanced Fast Steering Mirror

With the AFSM operating concepts validated by Kluk's successful demonstrations, the next logical development is to migrate the AFSM technology into a more flight-like design with performance turned for a specific mission profile. This thesis presents a design for such a fast steering mirror. The intent of this effort is to produce a design that is, at most, one iteration away from a flight-ready model. The design is named the small Advanced Fast Steering Mirror (sAFSM) to simultaneously denote its AFSM heritage and a focus on reducing the FSM's physical size.

1.2 Free Space Optical Communication

Free space optical communication (FSOC) is the use of light radiation to transmit signals across some distance without employing any dedicated propagation medium such as fiber optic wire. Free space optical communication is also called free space laser communication, laser communication, or simply lasercom. Many forms of free space optical communication systems exist and are used to communicate over distances ranging from a few decimeters to millions of kilometers. For instance, the IrDA ports on many laptops, personal digital assistants, and mobile phones use light emitting diodes (LEDs) to transfer data between consumer devices. IrDA is limited in range to a meter and speeds of up-to 16 $^{\text{Mbit}}/_{\text{s}}$. A number of commercial and hobbyist FSOC systems are designed to provide Ethernet-like links between buildings as an alternative to running or leasing physical cables (optical or copper). Presently available systems offer data rates of up-to 1.25 $^{\text{Gbit}}/_{\text{s}}$ across distances exceeding 2 kilometers.[23] Terrestrial FSOC systems are generally limited in distance by atmospheric phenomena, especially fog, that can dramatically reduce the transmission of laser light. In fact, many medium range systems (1 to 2 km) must reduce their link data bandwidth when operating in adverse conditions. Optical transmissions through space (in the exoatmospheric sense of the word) are not, of course, subject to atmospheric attenua-

tion. Therefore, extremely long range laser communication links are possible in space making space-based lasercom a very promising application of FSOC.

Since the early 1990s, several experiments have successfully demonstrated space/Earth and space/space free space optical communication. During the Galileo spacecraft's cruise to Jupiter, it turned its CCD camera towards Earth and detected laser pulses sent from Earth-based telescopes at a distance of over six million kilometers. Despite its simplicity, this Galileo Optical Experiment (GOPEX) was an early demonstration of the feasibility of interplanetary optical communication. The Ground/Orbiter Lasercom Demonstration (GOLD) program achieved a 1.024 $^{\text{Mbit}}/_{\text{s}}$ data rate between the Japanese ETS-VI spacecraft and Earth-based telescopes at JPL's Table Mountain facility - a distance of greater than 35,000 km. The European Space Agency demonstrated a 50 $^{\text{Mbit}}/_{\text{s}}$ low-earth-orbit (LEO) to geosynchronous orbit (GEO) optical link in the early 2000s with its SPOT 4 and ARTEMIS satellites. Additional details of these experiments can be found in Chapter 1 of JPL's overview of deep space optical communication.[16]

The use of laser communication in space is expected to continue to grow. In 2004, NASA initiated an ambitious program to integrate a free space optical communication terminal on the Mars Telecom Orbiter. The program, known as the Mars Laser Communications Demonstration (MLCD), aimed to establish a 1 to >30 $^{\text{Mbit}}/_{\text{s}}$ link between the Mars-orbiting MTO and Earth-based receives at distances surpassing 300 million kilometers.[5] MIT Lincoln Laboratory was tasked with designing, building, and testing the space-based terminal. Unfortunately the MLCD program was discontinued in 2005 along with the MTO due to shifting NASA priorities. However, the MLCD program serves as a prototype mission for the fast steering mirror designed in this thesis. Most of the terminal specifications that affect the FSM requirements, such as the transmit laser wavelength and telescope size, are copied directly from published MLCD documents.[5][34][3] The MLCD system is an ideal prototype mission because it is realistic, has challenging pointing requirements, is well documented, and is widely-known amongst the space lasercom community. Also, since future lasercom development programs could be based on MLCD, an FSM designed to meet its

requirements will likely satisfy the needs of any such evolutionary system.

Optical wireless links provide a number of advantages over radio-frequency (RF) alternatives. An often cited advantage, especially for military applications and ground-to-ground links, is increased security since jamming or eavesdropping on a narrow light beam is likely more difficult and detectable than setting up an antenna to intercept RF radiation. Ground-to-ground commercial FSOC system vendors also market freedom from spectrum licensing as an advantage because eye-safe light radiation is not subject to regulation like radio frequency emissions. Also, the target facing frontal area of optical communication terminals is usually smaller than that of a directional RF antenna. For space-based applications, however, the predominant advantage of laser communication is the potential for greatly increased data bandwidth without an inordinate increase in communication system mass or power consumption.

Optical communication enables high data rates due to two related factors. First, lasercom electromagnetic frequencies are much greater than those of typical spacecraft RF communications systems (e.g. $\approx$ 280,000 GHz for the MLCD vs. 32 GHz for Ka-band). In general, higher carrier frequencies permit larger channel bandwidth which leads, per information theory, to increased data rate. According to [37], optical bandwidths can be 1000 times greater than those of RF systems.

Second, given reasonably sized transmitting apertures, the energy beamed from an optical communication system diverges much less than an RF system. All electromagnetic waves (including perfectly focused collimated laser beams) spread as they travel through free-space due to diffraction according to the formula[29]:

$$\theta_{BW} = C\frac{\lambda}{a}, \tag{1.1}$$

where θ_{BW} is the full-cone angular beamwidth, λ is the wavelength, a is the transmitting telescope aperture, and C is a constant that depends upon the aperture shape and the precise definition of a beamwidth[3]. For the hypothetical laser communication system considered in this thesis, a 30.6 cm [12 in] diameter diffraction-limited

[3]Commonly the $1/e^2$ point

telescope, a 1.06 μm transmitting wavelength, and C equal to 1.2 are assumed. Thus, the transmit beam angular beamwidth is approximately 3.5 μrad. For comparison, the beamwidth of a Ka-band RF transmitter with a 3.2 m antenna is about 3,500 μrad [$\approx 0.2°$].

Since optical beamwidths are small, the beam spreads less as it propagates through space. Thus, the energy at the distant receiver is denser than if it had been transmitted with the same power and aperture at radio frequencies. The comparatively large optical transmit efficiency enables communication system designers to increase data rates due to greater signal levels, decrease the transmit aperture, or reduce transmitter power (usually a combination of all three). However, pointing such narrow beams becomes a significant challenge.

Most host spacecraft provide attitude control systems (ACS) to point instruments, sensors, and antennas in various directions as required by their functions. However, no present spacecraft are capable of maintaining sufficient stability required for deep space optical communication. Many sources of dynamic motion (jitter) on the spacecraft have magnitudes greater-than or roughly equal-to the required pointing performance. These sources may include solar array gimbals, cyropumps, reaction wheels, and ACS error and deadband. Therefore, secondary isolation and stabilization systems (sensors and actuators) are necessary for pointing long-range, low-divergence optical communication beams. Fast steering mirrors are critical components in such active stabilization systems.

1.3 Thesis Overview

The content of this thesis begins in Chapter 2 with an analysis of a hypothetical but realistic spacecraft-based, free-space optical communication mission. An assumed spacecraft disturbance, modeled from previous spaceflight measurements, is transmitted through a passive vibration isolation system to an optical bench on which the FSM is mounted. Modeling the isolation system as a parallel spring-damper pair, the effect of the isolator's natural frequency on transmitted base motion is presented.

Similarly, the effect of FSM control bandwidth on residual, i.e. unrejected, object-space beam jitter is explored, assuming a simple, gain+lead controlled, type-2 plant. The resulting plot, copied here as Figure 1-3, helps determine a specification for required FSM bandwidth given a desired level of disturbance rejection performance. A minimum angular acceleration requirement is then derived based upon the predicted optical table motion profile and FSM bandwidth.

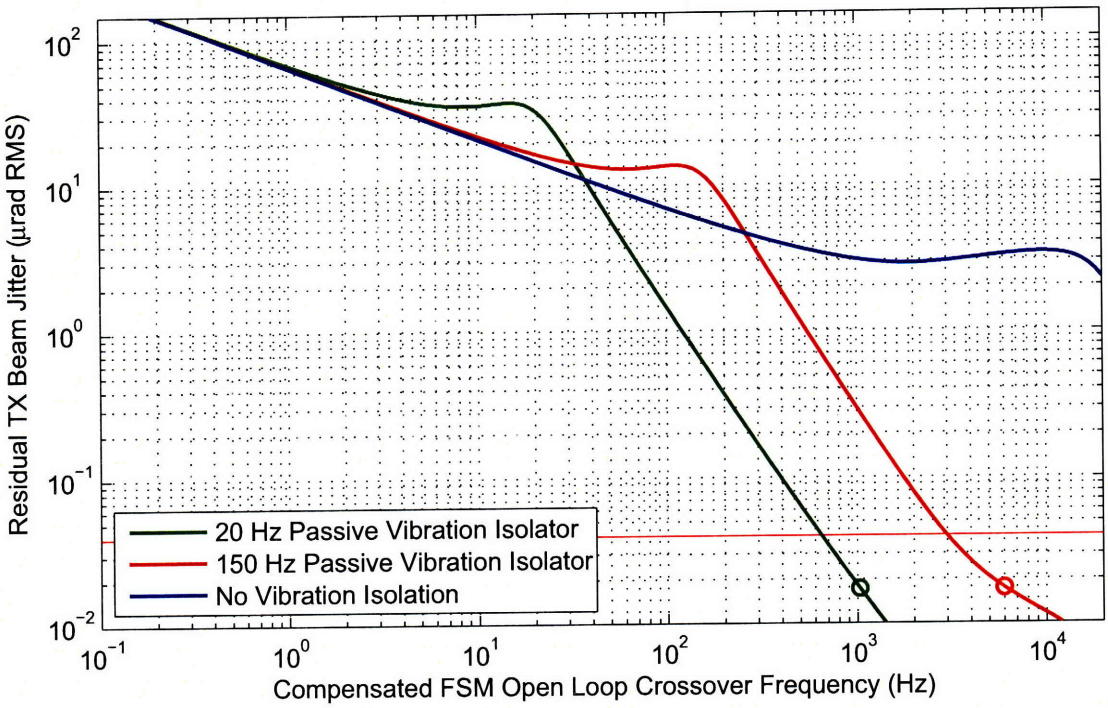

Figure 1-3: Residual Beam Jitter RMS as a Function of Compensated FSM Open Loop Crossover Frequency

Chapter 2 additionally gives, with justification, requirements for FSM optical parameters like mirror aperture, field of view, and angular resolution. Also, I list size and mass goals, along with a visual comparison of the sAFSM size objective with outlines of heritage systems (see Figure 1-4).

Chapter 3 starts with a review of the Ultra Fast Motor (UFM) flux steering actuators used in the AFSM. Leaving many of the details to Lu's and Kluk's theses, I show that the UFM force output is, remarkably, a linear function of both armature displacement and coil current. However, Kluk's UFM-based electromagnetic configuration proved difficult to miniaturize to a size appropriate for the small FSM. Instead,

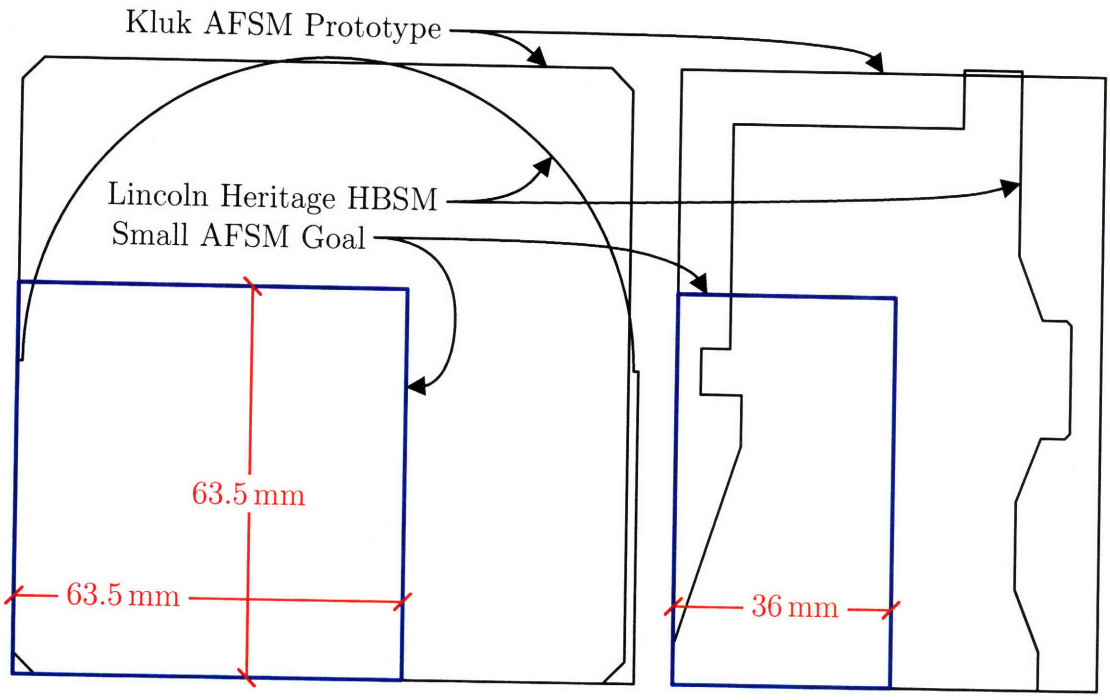

Figure 1-4: sAFSM Size Comparison ($\approx 4/5$'s scale on 8.5"$\times$11" paper)

a new "ring armature" flux steering electromagnetic configuration, conceived from one of Professor Trumper's suggestions, is developed. The concept, illustrated in Figure 1-5, is analyzed with an idealized, i.e. leakage-free, magnetic equivalent circuit. I derive a set of linear expressions for torque as a function of differential-mode current and armature rotation as well as force versus common-mode current, differential current, and armature translation. The force and torque equations are presented with both magnetic circuit variables (e.g. reluctance, magnetomotive force) and design parameters (area, length, etc.).

The 4$^{\text{th}}$ chapter introduces a second-order mass/spring/damper model of the FSM in order to specify design values for actuator torque and bearing stiffness. Plots of torque versus spring constant show that increasing the bearing stiffness above $1\,^{\text{N·m}}/_{\text{rad}}$ drives the torque requirement beyond what is required to move the inertia at maximum acceleration. However, the consequence of a more compliant bearing in the articulated degrees of freedom (DOFs) is reduced stiffness to spurious forces in the constrained DOFs. Ultimately, I specified the actuator torque to be $>0.04\,\text{N·m}$

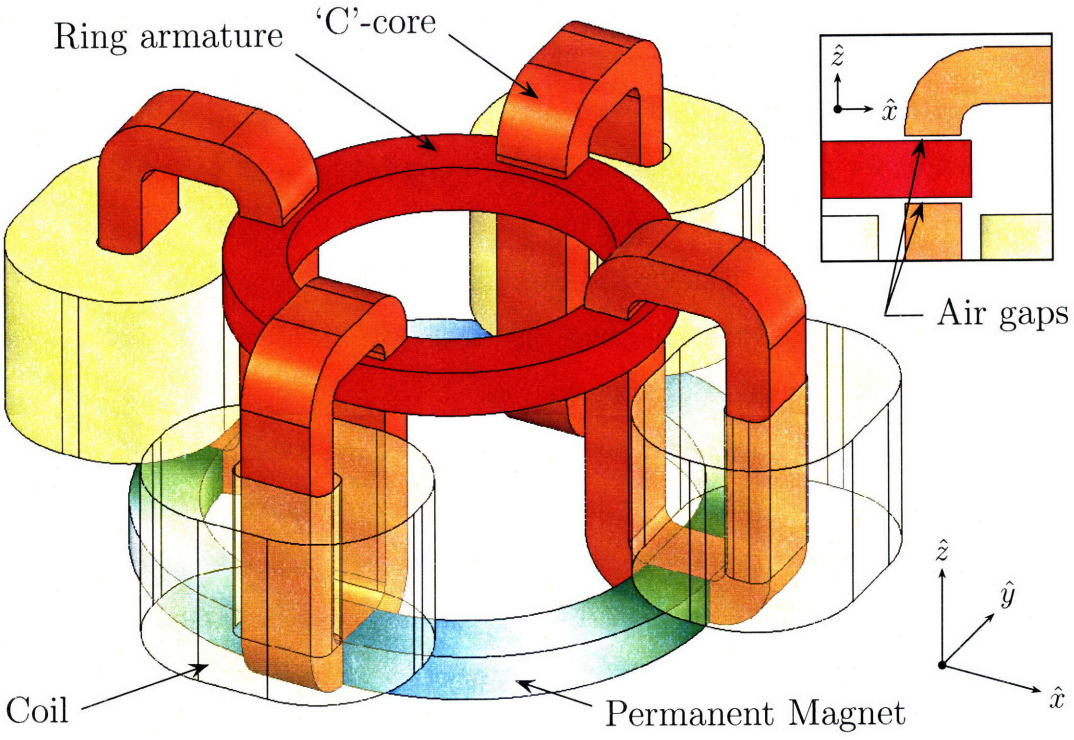

Figure 1-5: Ring Armature Concept

and a stiffness between 1 and 3 $^{\mathrm{N\cdot m}}/_{\mathrm{rad}}$.

The second-half of Chapter 4 details the design's bearing implementation, beginning with a discussion of Kluk's rubber pad and axial flexure hybrid solution. I show that Kluk's cylindrical axial flexure, which constrains the armature translation in the mirror normal direction, will not work in the smaller sAFSM. Instead, the sAFSM's control system is additionally tasked with actively maintaining zero mirror normal translation. The linear displacement control uses the same sensors and actuators that control tip and tilt. Kluk's rubber pads are, however, retained as they provide good rigidity in non-actuated degrees of freedom and because their small size is superior to metal flexures. I present expressions for the rubber bearing rotational, axial, and radial stiffness as functions of pad geometry and material properties. The chapter concludes with a bar plot of achievable rotational stiffs versus discrete pad thickness.

While Chapters 3 and 4 discuss the sAFSM design with ideal, parameterized equations, Chapter 5 presents rationale for specific design decisions like the selection

of a soft magnetic material and component sizes. Magnetic material flux saturation, a nonlinear effect ignored in earlier chapters, leads to a specification for stator pole area. Choices for permanent magnet strength and frontal area as well as required coil magnetomotive force follow. Section 5.4.2 compares the high-frequency benefits of thin-wire coils against the improved packing efficiency of large-diameter wire. The decision to use relatively large 16-gauge wire in the sAFSM is supported with a two-dimensional time-harmonic magnetic analysis.

The ring armature magnetic concept is tested with a three-dimensional magneto-static finite element analysis. Resulting plots of actuator torque and force as functions of armature displacement and coil current validate the magnetic equivalent model. However, the FEA-derived torque and force constants are significantly smaller than predicted from the evaluation of the linear expressions. The discrepancy is shown to result from large permanent magnet flux leakage. Chapter 5 also presents a structural finite element analysis and optimization of the armature's modal frequencies. The tape wound ring core, a composite made from relatively compliant epoxy and stiff nickel-iron metal, is modeled as a transversely isotropic material. The final armature geometry's first non-rigid natural frequency, 18.4 kHz, is sufficient to permit a 6 kHz open-loop crossover frequency for control. The chapter concludes with an illustration of the as-design sAFSM, which is also shown in Figure 1-6.

A final chapter describes the current state of the sAFSM effort, presents a couple of ideas for future investigation, and offers a conclusion. Appendix chapters give details of calculations and supporting figures that were not appropriate for inclusion with the body material.

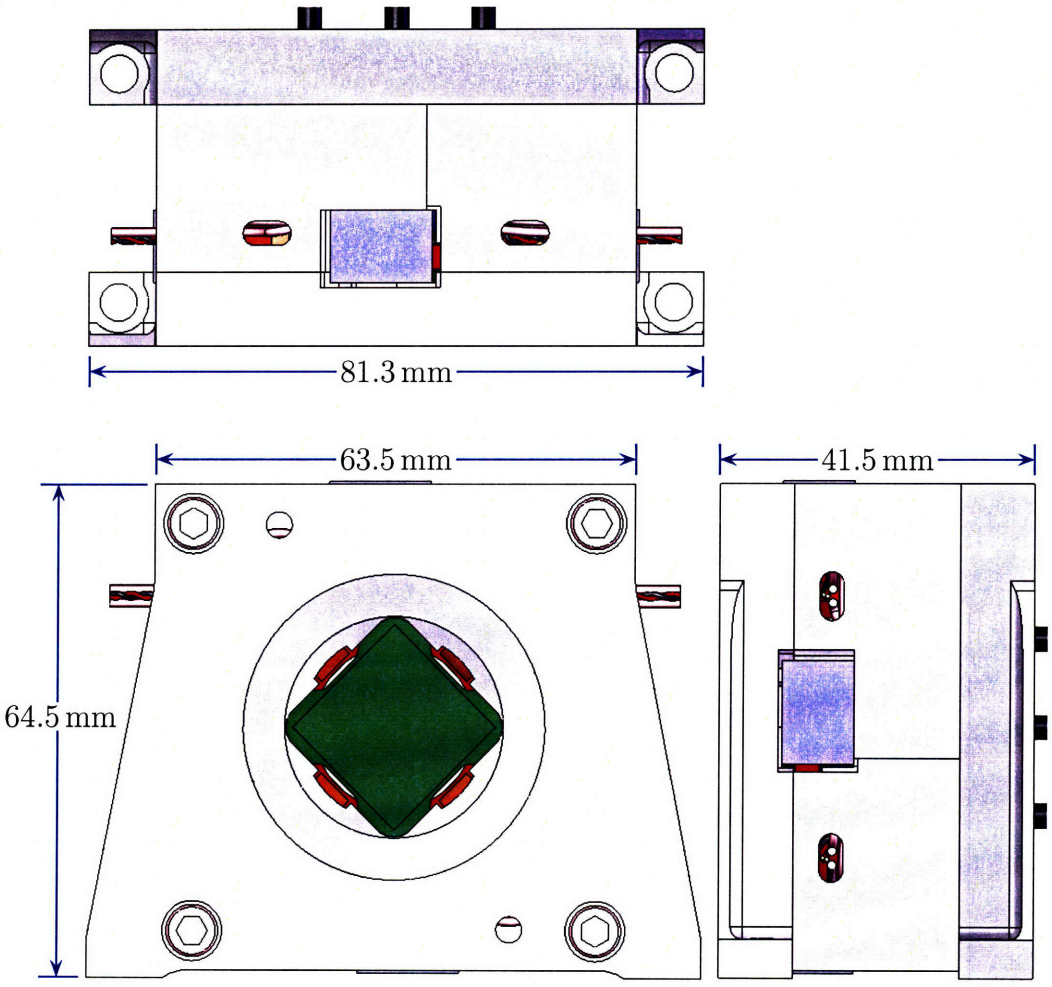

Figure 1-6: sAFSM Solid Model (actual size on 8.5"×11" paper)

THIS PAGE INTENTIONALLY LEFT BLANK

Chapter 2

System Performance Specification

Fast steering mirrors are used in a wide variety of applications as discussed in Section 1.1. Each application necessitates the optimization of different FSM performance characteristics. An FSM that performs a scanning function, for example, might require a large stroke, high angular acceleration, excellent open-loop pointing resolution, but relatively limited bandwidth. The FSM developed in this thesis is targeted for inertial disturbance rejection for free-space optical communication. In general, this application calls for very high bandwidth but limited acceleration and stroke. The fast steering mirror's size and weight are additional critical performance parameters since the FSM will be used on space or airborne platforms. This chapter developers a set of quantitative performance criteria for an FSM based on a hypothetical, MLCD-like application scenario.

2.1 Pointing Requirements

The effect of pointing error (mispointing) on optical communication data rate is actually quite complex as it depends upon the beam profile and the optical signal coding[36]. Since the objective of this thesis isn't designing a lasercom system and since a discussion of beam profiles and coding schemes is far outside the intended scope, I've relied on published MLCD documentation to provide a pointing performance specification. However, the rationale for pointing requirements that are much

smaller than a beamwidth might not be obvious to every reader (as it wasn't for the author). Thus, a naive example for a simple pointing system is presented below to illustrate the analysis without delving too deeply into the details.

Assume that a planar pointing system's pointing error is a normally distributed random variable with non-zero mean and standard deviation (square root of variance). Also assume that the beam's power is uniform across the entire beamwidth and zero outside of it. The probability that the transmit beam intercepts the target is found by integrating the Gaussian function between plus and minus one-half of a beamwidth. Suppose, for example, that both the standard deviation and mean are equal to a beamwidth. The resulting probability that the beam hits the target at any particular instant is a paltry 48%. The communications system designers, who usually push for every possible bit of channel capacity, would likely be aghast at the thought of loosing 52% of throughput to mispointing. Note that signal coding, which I've ignored here, could potentially reduce or exacerbate the loss. Therefore, both the dynamic (standard deviation) and static (mean) pointing performance must be a fraction of a beamwidth - typically less than one-fifth.

It is often convenient to treat non-planar or "two-axis" pointing error (θ_e) as the vector sum of two orthogonal, Cartesian components θ_x and θ_y. "Single-axis" pointing errors θ_x and θ_y are independent random variables with distributions that are commonly presumed to be normal to simplify the stochastic analysis. The variances of θ_x and θ_y are assumed to be equal (i.e. variance is independent of direction) and are assigned the label σ^2. The means of θ_x and θ_y, which are not necessarily equal, can be combined with the Pythagorean theorem to give a radial mean η. In [36], Vilnrotter shows that the resulting probability density function (PDF) for the two-axis pointing error θ_e is the Rice distribution:

$$p(\theta_e) = \frac{\theta_e}{\sigma^2} \exp\left[-\frac{1}{2\sigma^2}\left(\theta_e^2 + \eta^2\right)\right] \mathrm{I}_0\left(\frac{\theta_e \eta}{\sigma^2}\right), \tag{2.1}$$

where I_0 is the modified Bessel function of zeroth order.

The probability that the pointing error is less than an angular threshold δ is found

by integrating the above PDF over the interval from zero to δ. Values for η and σ are semi-independently chosen to yield a sufficiently high probability of pointing to the target within the threshold radius. For example, Figure 2-1 shows the two-axis pointing error PDF for $\eta = \theta_{BW}/5$ and $\sigma = \theta_{BW}/5$, where θ_{BW} is the downlink full-cone angular beamwidth. The shaded area, representing the integral between zero and a threshold of $\delta = \theta_{BW}/2$, is the probability of pointing to within $\theta_{BW}/2$ of the target at any instant, in this case about 87.9%. Assuming that the threshold cannot be relaxed (increased), improving the probability above 95% requires either decreasing the radial mean η to about $1/20$'th of a beamwidth or decreasing standard deviation σ to about $1/7$'th of a beamwidth (or some combination of both).

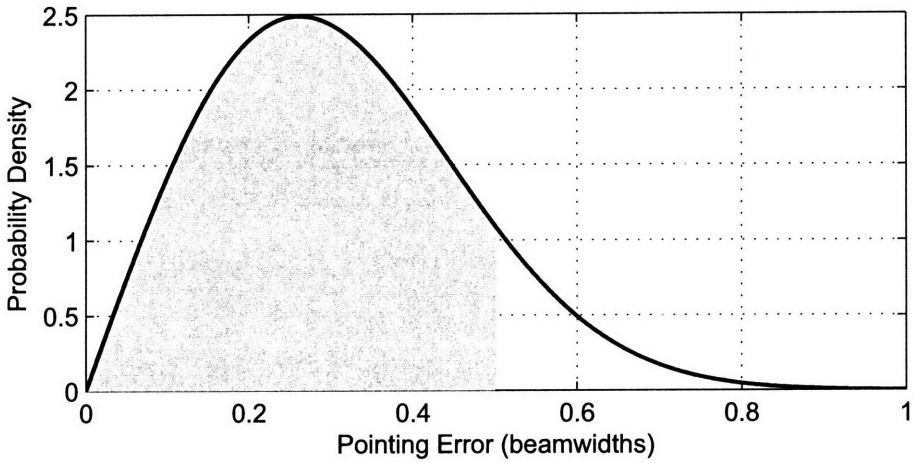

Figure 2-1: Two Axis Probability Density; $\eta = \theta_{BW}/5$, $\sigma = \theta_{BW}/5$, $\delta = \theta_{BW}/2$

The MLCD pointing analysis given in [4] uses a threshold of $\approx$1.6 µrad with corresponding values for η and σ of 0.36 µrad and 0.36 µrad respectively. Unlike the naive planar example, the transmitted power in a real system fades with increasing mispointing angle. The MLCD threshold angle, which is slightly less than a half of a beamwidth, was chosen to limit the effective reduction in transmitter gain to 2 dB. Plugging the values into (2.1) and integrating from zero to $\approx$1.6 µrad gives 0.9988. Thus, if the MLCD pointing system meets the specifications for η and σ, then the pointing loss should be less than 2 dB 99.88% of the time.

The non-static parts of θ_x and θ_y are themselves composed of independent random

variables representing numerous sources of pointing error. Sources of pointing error can be classified by their correlation time. Quasi-static error sources have relatively long correlations times, as in sensor bias offsets, changes to optical alignment, and telescope calibration error. Dynamic error sources, such as sensor noise and unrejected jitter, have considerably shorter correlation times. Tables 2.1 and 2.2 give standard deviation values for quasi-static and dynamic pointing error sources allocated in the MLCD pointing error budget[7].[1] Since the noise sources are assumed to be uncorrelated and zero-mean, they combine power-wise (i.e. the standard deviations sum via the root-sum-square function). RSS-ing the error sources in the MLCD pointing budget yields an overall error standard deviation of $\approx 0.4\,\mu$rad, slightly greater than the $0.36\,\mu$rad goal for σ listed above.

Table 2.1: MLCD Dynamic Pointing Error Budget

Dynamic pointing error sources	Residual jitter (nrad)
MIRU linear motion coupled noise	200
Telescope and optical bench jitter	150
Point ahead mirror sensor noise	130
FPA tracking error	100
Quad-cell noise	60
MIRU quiescent sensor noise	50
Unrejected angular base motion	40
MIRU off-axis coupling	40
Acceleration coupled error	17

The seventh line in Table 2.1 allocates 40 nrad for pointing error due to unrejected base motion. In other words, the secondary beam pointing and stabilization system must be designed to limit residual jitter caused by spacecraft dynamic motion to a maximum standard deviation of 40 nrad. Thus, this thesis use 40 nrad as the desired performance when determining actuator bandwidth and acceleration requirements in Sections 2.3 and 2.4.

[1]Note that several items from the tables are specific to the MLCD pointing system (e.g. "MIRU linear motion coupled noise") and will not be explained here; readers should consult the reference for additional detail.

Table 2.2: MLCD Quasi-static Pointing Error Budget

Quasi-static pointing error sources	Residual bias (nrad)
Optical aberration calibration residual	144
FPA transmit track bias	100
FPA beacon track bias	100
Uncalibrated environmental error	85
Point-ahead calculation errors	80
Spacecraft velocity error	70
Spacecraft attitude (roll) sensor error	40
Alignment mechanism calibration error	40
Spacecraft position error	10

2.2 FSM Size and Mass

Mass is an obviously important optimization parameter in spaceflight systems (critically so in interplanetary missions) as the launch costs per kilogram of spacecraft dry mass are astronomical (i.e. >$30,000 per kg for a Mars orbiter[38]). Mass constraints are especially severe for the communication subsystem since it typically accounts for only a small fraction of the total spacecraft mass (e.g. 8.3% on Mars Global Surveyor[37]). However, existing fast steering mirror designs are not all that massive (on the order of a couple of kilograms) and therefore the potential direct savings from mass reduction might not be sufficient to offset cost and risks associated with a new design.

Decreasing FSM size, however, provides significant dividends beyond the corresponding mass reduction of the FSM itself. A smaller fast steering mirror permits a more compact optical arrangement, possibly leading to significant mass reductions in the structure supporting the optical components. Additionally, a small FSM (and the resulting small optical bench) might enable new applications of free-space optical communications for which the heritage FSMs would have been too large. Also, smaller FSM size leads to higher achievable bandwidths and accelerations. Thus, a primary objective of this design effort is to dramatically reduce the size of the FSM relative to either the Lincoln heritage HBSM or the Kluk prototype AFSM. Specifically, the size and mass goals for the sAFSM are 63.5 mm [2.5 in] in height, by 63.5 mm in width, by 36 mm [1.42 in] in thickness, and 0.8 kg in mass. Figure 2-2 below compares the

outlines of existing fast steering mirrors with the design goal.

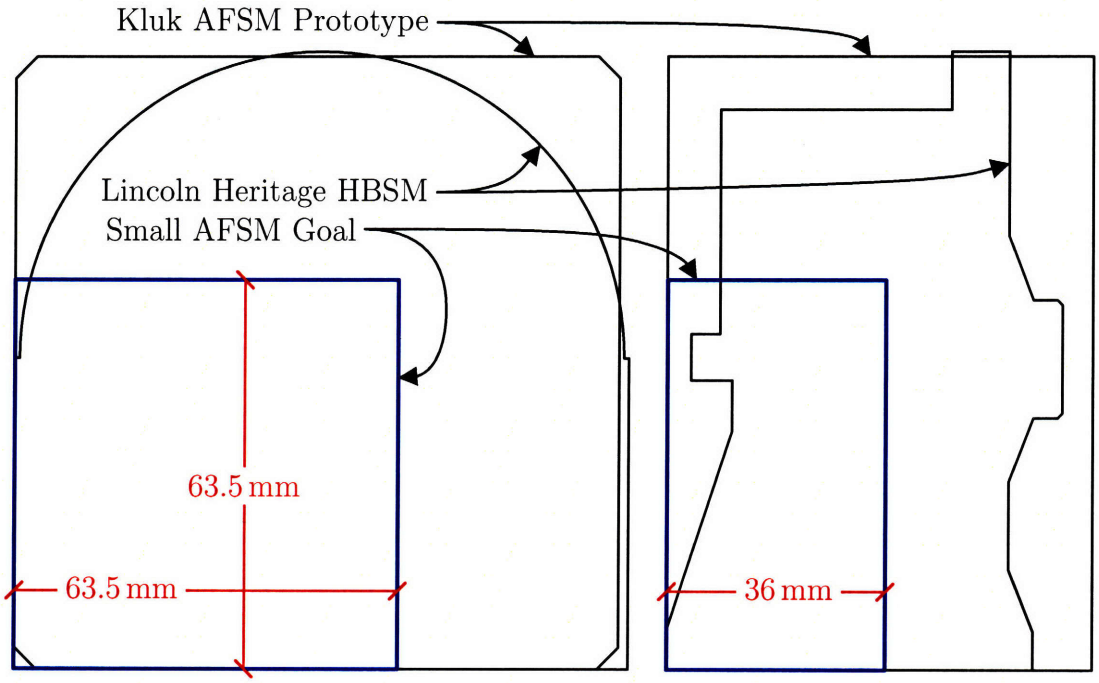

Figure 2-2: sAFSM Size Comparison ($\approx 4/5$'s scale on 8.5" $\times$11" paper)

2.3 Fast Steering Mirror Bandwidth

Figure 2-3 is a cartoon of a pointing system for the hypothetical free space optical communication terminal. Many components required for a realistic laser pointing system, most notably feedback sensors, are excluded from the drawing for simplicity. An optical table (C) is attached to the host spacecraft (A) with multiple passive vibration isolators (B). A laser and lens (D) produce a collimated beam that is reflected off a fast steering mirror (E) into a telescope (F). An expanded laser beam exits the telescope and travels towards the distant target.

Assume that the spacecraft (SC), optical table, and telescope are quasi-static aligned such that the transmit beam is perfectly collinear with the desired pointing vector when the FSM is held at its neutral position. Also assume that feedback sensors for controlling the FSM position are perfect (error-less, noiseless, and infi-

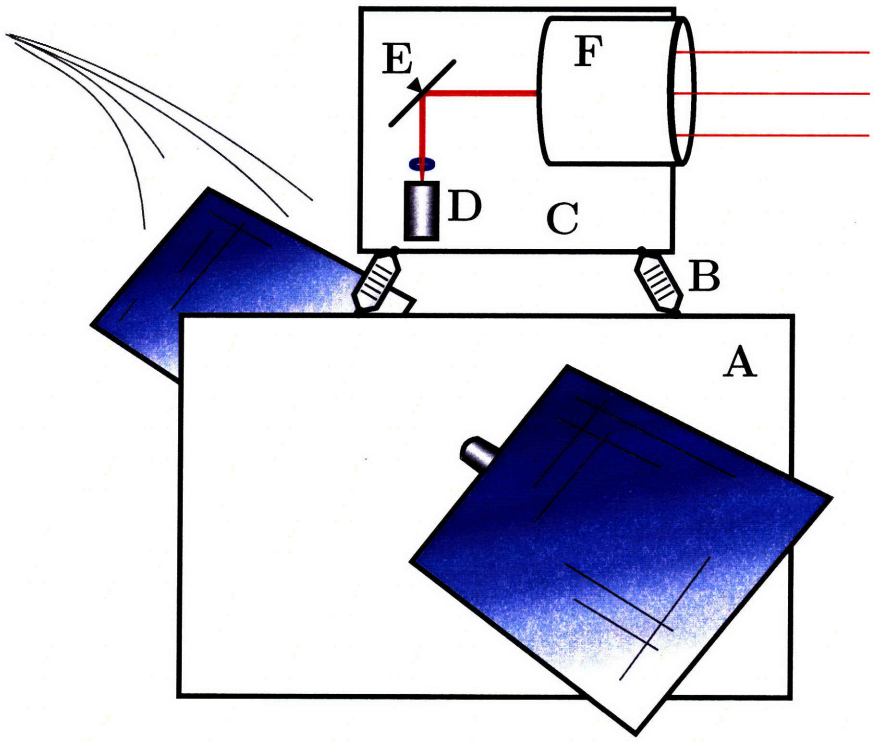

Figure 2-3: Pointing System Cartoon

nite bandwidth) and that all structures are rigid. Thus, uncompensated dynamic motion (jitter) is the only potential source of mispointing. The FSM must move to counteract optical table jitter in order to keep the transmit beam aligned with the desired pointing vector. Fast steering mirror bandwidth requirements, and subsequently acceleration requirements, are derived by assuming a particular jitter profile and calculating the FSM motion required to satisfactorily reject the disturbance.

Power spectral density (PSD) plots of angular displacements are a common characterization of jitter on optical communication platforms. PSD plots are useful because they show the frequency content of the disturbance signal and they can be integrated to give a single-value figure of the motion's severity - the root-mean-square (RMS). Additionally, PSD curves can be easily transformed through linear transfer functions to give jitter characteristics at other points in the system, as will be done below. Appendix A gives a brief introduction to spectral analysis, including a definition of the power spectral density function, and provides references to relevant sources. The appendix also presents a useful algorithm for integrating a PSD when it is plotted

with straight-line segments on log-log axes.

For the FSM designs considered in this thesis, the mirror structure's center of mass is approximately collocated with the FSM's effective pivot. Therefore, linear accelerations mechanically couple loosely, if at all, into the transmit beam pointing vector. Additionally, given the long baseline between optical terminals, linear displacement disturbances negligibly contribute to pointing error. Thus, linear platform jitter is ignored in this analysis.

Experiments on previous spaceflights have measured dynamic motion. Figure 2-4 is a plot of envelopes of typical angle displacement power spectral densities for a few platforms. Real PSD curves (as opposed to envelopes) would appear somewhat different as spacecraft natural modes and other sources of vibration (e.g. momentum wheels) would result numerous peaks that might equal, but not exceed, the envelope curve. Specifying FSM acceleration based on an envelope PSD is a conservative approach as the resulting requirement should be sufficient, with margin, to reject the jitter of any platform that contributed to the envelope. For the hypothetical system considered in this thesis, the "MLCD" jitter profile is assumed.

Professor Trumper suggested an alternative plot for jitter characterization. Figure 2-5 is a plot of the signal's (angular displacement) RMS value over the bandwidth between f_0 and f as a function of f. f_0 is the minimum frequency considered in the analysis (and usually, but not necessarily, the frequency axis' origin). Essentially, this plot shows how the signal's RMS value accumulates with frequency. Two nice features of this "cumulative RMS" plot are that the y-axis units are comprehensible (e.g. μrad instead of $\mu rad^2/Hz$) and that the reader does not need to mentally integrate the area under a curve (a difficult task on a log-log plot) to gauge the signal's severity.

Figures 2-4 and 2-5 show that the MLCD platform is more benign than either an aircraft or a space shuttle platform, as one would expect. The plots also show that the jitter signal is dominated by low-frequency (<1 Hz) content. The MLCD's platform jitter (151 μrad RMS) is much greater than the transmit beamwidth and 1000 times larger than the pointing error budget allocated for jitter. Thus, passive

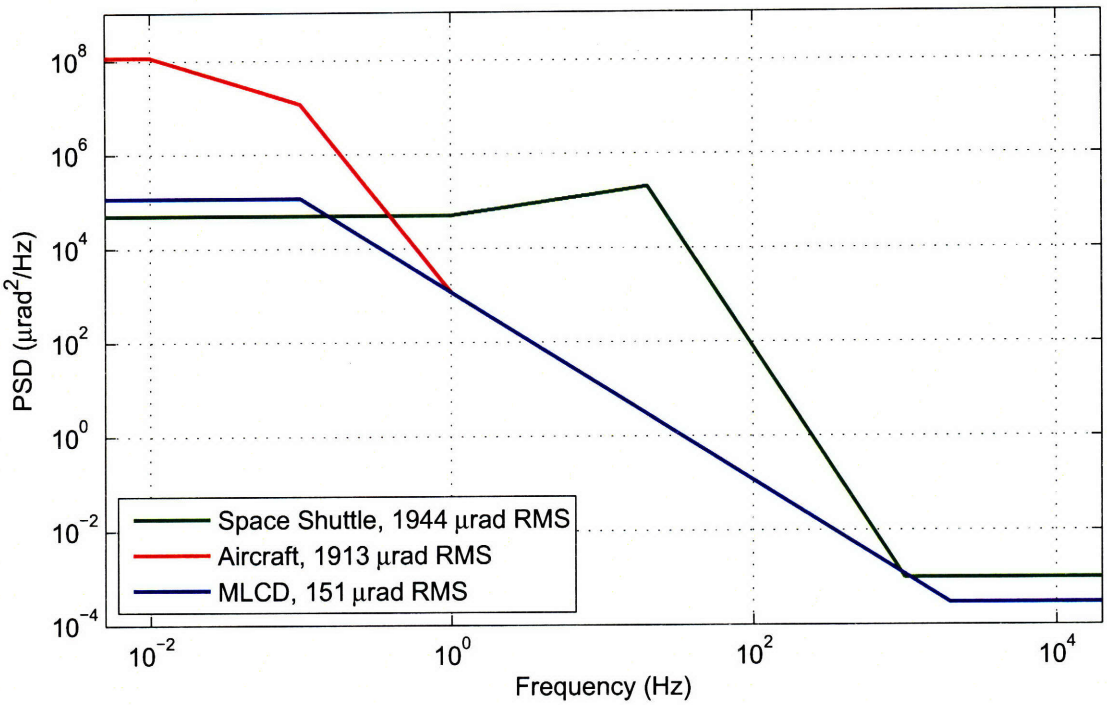

Figure 2-4: Angle Displacement (Jitter) Power Spectral Density for Various Platforms[6][16]

and/or active suppression of disturbance motion is obviously necessary. As a sanity check, note that the MLCD jitter is comparable to a spacecraft vendor's published pointing performance.[19]

Referring back to Figure 2-3, assume that the platform jitter is generated entirely on the spacecraft side of the SC / optical table interface. Furthermore, assume that the platform jitter is not affected by the response of the optical table, that is, the disturbance motion is "stiff". The resulting jitter at the optical table is then found by transforming the base disturbance profile through a transfer function modeling the dynamics of the vibration isolators. The vibration isolation system is modeled as a single spring-damper pair (a "two parameter" isolation model) with a specified natural frequency and quality factor. Figure 2-6 is a graphical representation of the vibration isolator dynamics where $\theta_{SC}(t)$ is the spacecraft disturbance angular displacement, $\theta_{OT}(t)$ is the displacement of the optical table, K_{VI} and B_{VI} are the vibration isolator's spring and damping constants respectively, and I_{OT} is the optical table rotational inertia.

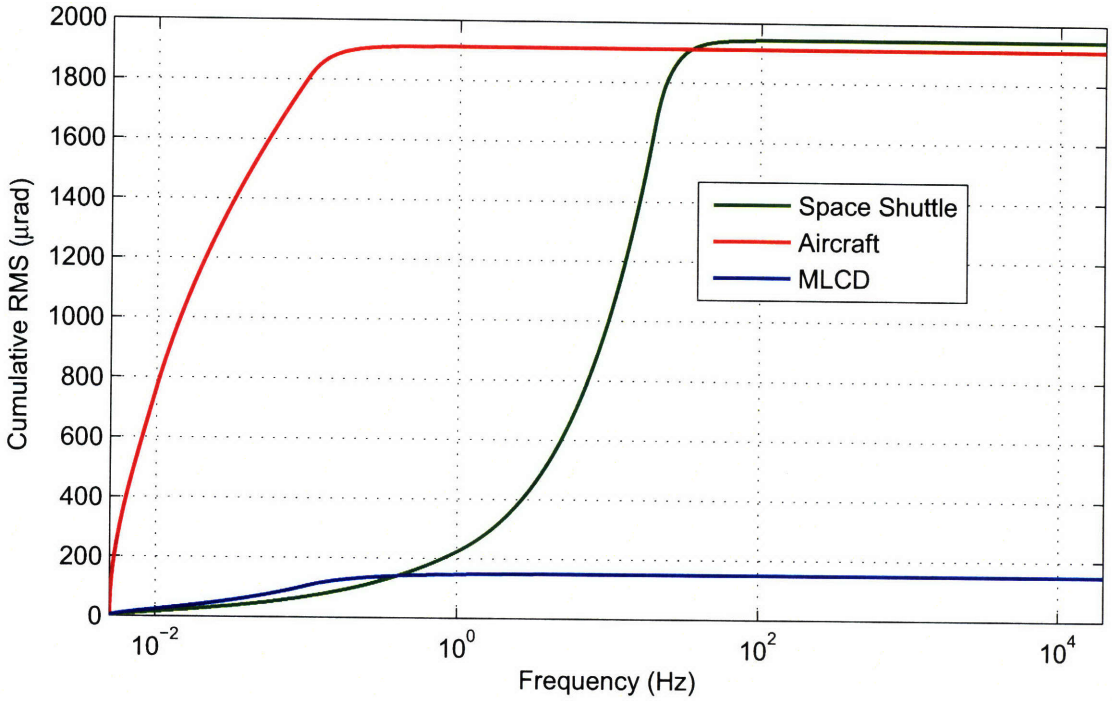

Figure 2-5: Angle Displacement (Jitter) Cumulative RMS for Various Platforms

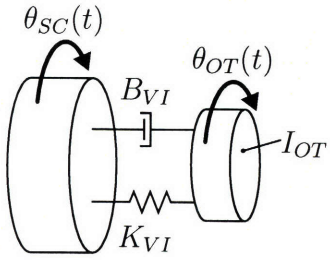

Figure 2-6: Vibration Isolator Dynamic Model

Using Newton's dot notation to represent time derivatives, the vibration isolator dynamic equation is:

$$I_{OT}\ddot{\theta}_{OT}(t) = -K_{VI}\big(\theta_{OT}(t) - \theta_{SC}(t)\big) - B_{VI}\big(\dot{\theta}_{OT}(t) - \dot{\theta}_{SC}(t)\big). \tag{2.2}$$

Transforming (2.2) to the Laplace domain and collecting terms gives:

$$\theta_{OT}(s)\big(s^2 I_{OT} + sB_{VI} + K_{VI}\big) = \theta_{SC}(s)\big(sB_{VI} + K_{VI}\big), \tag{2.3}$$

which is then manipulated into a spacecraft angular displacement to optical table

angular displacement transfer function in (2.4).

$$\frac{\theta_{OT}(s)}{\theta_{SC}(s)} = \frac{sB_{VI} + K_{VI}}{I_{OT}s^2 + sB_{VI} + K_{VI}} = \frac{s^{B_{VI}/I_{OT}} + {}^{K_{VI}/I_{OT}}}{s^2 + s^{B_{VI}/I_{OT}} + {}^{K_{VI}/I_{OT}}} \tag{2.4}$$

The ratios ${}^{K_{VI}/I_{OT}}$ and ${}^{B_{VI}/I_{OT}}$ are determined from the specified natural frequency, ω_n in ${}^{\text{rad}}/_{\text{s}}$ or f_n in hertz, and a unitless quality factor, Q, per:

$$\frac{K_{VI}}{I_{OT}} = \omega_n^2 = (2\pi f_n)^2, \tag{2.5}$$

and

$$\frac{B_{VI}}{I_{OT}} = \frac{\omega_n}{Q} = \frac{2\pi f_n}{Q}. \tag{2.6}$$

Examining the transfer function polynomials reveals that at low frequencies ($s = \text{j}\omega = \text{j}2\pi f \approx 0$) the constant term ${}^{K_{VI}/I_{OT}}$ dominates both the numerator and denominator; hence, the optical table moves with the spacecraft. At high frequencies the s^2 term grows large compared to the other denominator and numerator terms and very little spacecraft disturbance is transmitted to the optical table. At intermediate frequencies, the effect of the vibration isolator parameters on disturbance rejection performance is best explained by visualizing the asymptotic magnitude response of the numerator and denominator individually. That is, transfer function (2.4) is split into the products of canonical transfer functions $(s^{B_{VI}/I_{OT}} + {}^{K_{VI}/I_{OT}})$ and $(s^2 + s^{B_{VI}/I_{OT}} + {}^{K_{VI}/I_{OT}})^{-1}$. The asymptotic magnitude response of each canonical transfer function is plotted on a log-log plot. Summing the individual magnitude responses on logarithmic axes gives the response for the original transfer function. Most every introductory control systems textbook, [32] for example, describes sketching magnitude response plots from canonical transfer functions. Also, note that we do not care about the isolator's phase response.

Let's first consider the second order Laplace equation in the denominator. Its asymptotic magnitude slope is flat at low frequencies and changes to -2 (-40 ${}^{\text{dB}}/_{\text{decade}}$) above the isolator's natural frequency. Therefore, lowering the isolator's natural frequency specification results in improved attenuation of high frequency ($> f_n$) distur-

bance inputs. For a given platform inertia then, a low natural frequency translates into a small spring constant. A small spring constant is troublesome, however, because it requires a large stroke to accommodate significant variations in platform accelerations (1 g during Earth assembly and testing, multiple g's at launch, and micro-g's in space). Therefore, selecting an optimal passive vibration natural frequency is a tradeoff between rejection performance and suspension stroke.

The magnitude response of the zero (numerator) changes from a flat slope at low frequencies to a $+1$ ($+20\,^{\mathrm{dB}}/_{\mathrm{decade}}$) slope at frequencies above a zero frequency ω_z, equal to ${}^{K_{VI}}/_{B_{VI}}$ in radians per second (equivalently f_z in hertz, equal to ${}^{K_{VI}}/_{B_{VI}} \cdot {}^{1}/_{2\pi}$). Using (2.5) and (2.6), it is easy to show that the zero frequency is equal to the product of natural frequency and quality factor:

$$\omega_z = \frac{K_{VI}}{B_{VI}} = \frac{\omega_n^2 I_{OT}}{\frac{\omega_n}{Q} I_{OT}} = \omega_n Q. \tag{2.7}$$

The zero's positively sloped magnitude decreases the passive isolator's rejection performance above the zero frequency. Increasing the specified quality factor, thereby raising the zero frequency, diminishes the influence of the zero and, as a result, improves optical table isolation from base disturbances. However, Q's value cannot be set arbitrarily high. The second-order denominator's magnitude response peaks, surpassing unity, near the system's natural frequency for quality factors greater-than 0.5. Thus, high-Q vibration isolators will actually amplify base disturbances. The severity of the peaking is a monotonically increasing nonlinear function of increasing quality factor. Therefore, selecting an optimal Q value is a tradeoff between disturbance amplification at the natural frequency and improved rejection at frequencies above ω_n.

The FSM designed here conservatively assumes a relatively stiff 150 Hz passive isolation system with a quality factor of 4. For comparison, the MLCD system was designed with a 15 to 20 Hz natural frequency isolation system.

Transforming a PSD profile through a transfer function requires multiplying the PSD by the square of the transfer function's gain[35]. The resulting optical table

jitter power spectral density, for both a 20 and 150 Hz passive vibration isolation system, is plotted in Figure 2-7. The resulting RMS values for each curve are listed in the figure legend. Note that the passive isolation does not seem to improve optical table jitter in the RMS sense - in fact, the RMS value actually increases slightly for the 20 Hz isolator. The benefit of the passive isolator system is masked by the jitter's overwhelming low frequency content. Revisiting the cumulative spectra of Fig. 2-5 confirms that all of the RMS value is accumulated below 1 Hz, where the isolation system has no attenuation. At 151 μrad, the optical table RMS jitter remains much larger than a beamwidth. Therefore, the fast steering mirror is required to actively reject the disturbance motion.

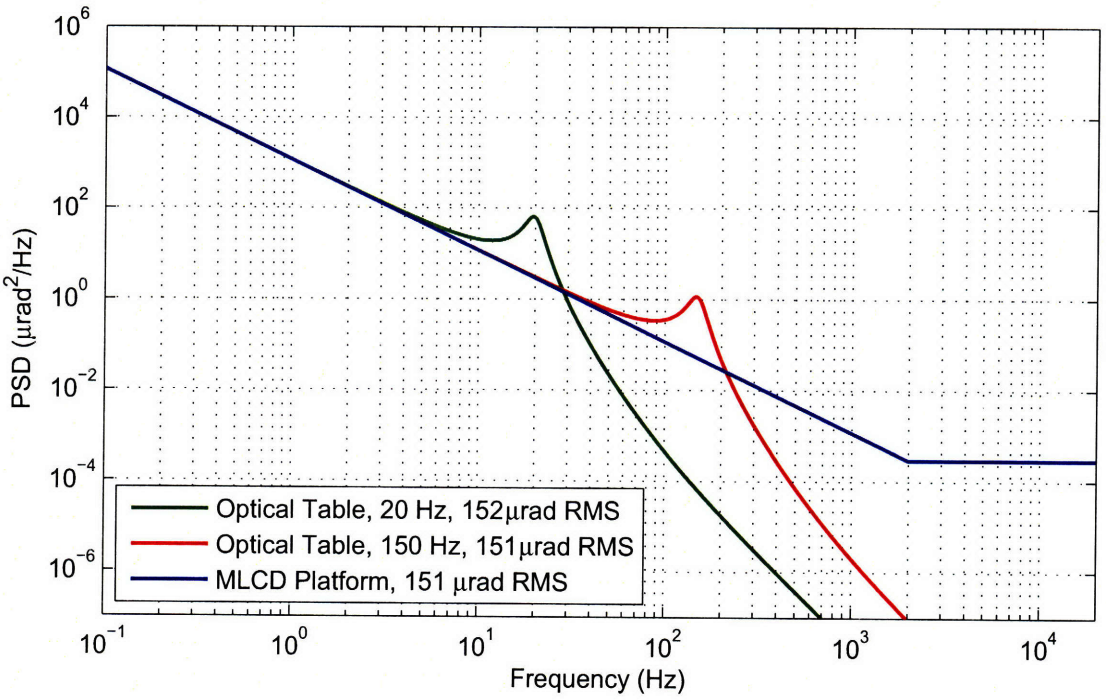

Figure 2-7: Optical Table Angle Displacement (Jitter) Power Spectral Density

For perfect disturbance rejection, the ratio of FSM displacement (θ_{FSM}) to optical table displacement (θ_{OT}) is *not* 1:1 because of (a), the mirror doubling effect and (b), telescope magnification. The mirror doubling effect is a consequence of the well-known "law of reflection": the angle between a reflected beam and the mirror's normal vector (θ_R) is equal to the angle between the incident beam and mirror normal (θ_I). If the

incident beam is stationary, rotating the mirror by θ_{FSM} increases the incident angle by θ_{FSM} and, because $\theta_R = \theta_I$, also increases the reflected angle by θ_{FSM}. Thus, the total reflected beam rotation is twice θ_{FSM}. The afocal telescope's magnification bends the transmit beam towards the telescope's optical axis, similar to the refraction of a light beam entering a media with a greater refractive index. If θ_{IS} and θ_{OS} are the angles of the transmit beam entering and exiting the telescope with respect to the optical axis then the ratio of θ_{IS} to θ_{OS} is equal to (actually, the definition of) the telescope's angular magnification. Figure 2-8 is a detail view of the optical bench illustrating these effects. The dashed and solid red lines are transmit beam ray traces with the FSM in the neutral and slightly displaced position respectively.

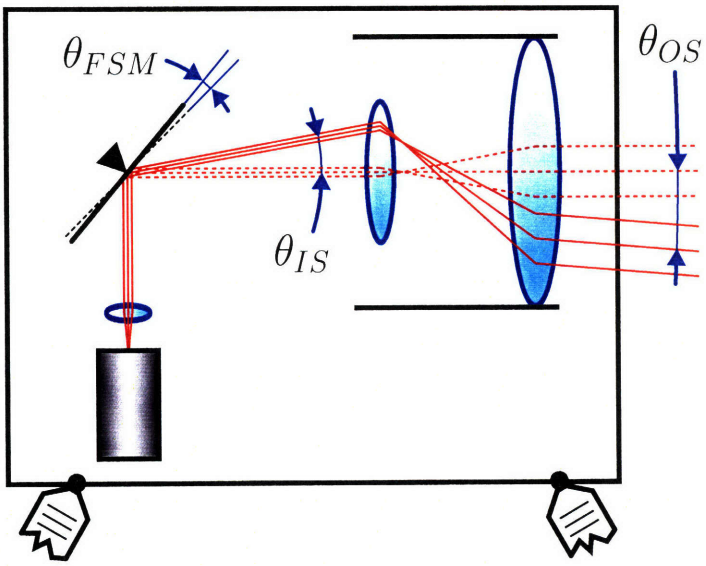

Figure 2-8: Displaced FSM Optical Ray Trace

Before proceeding further, note that the purpose of the optical analysis presented in this chapter is to derive requirements for the fast steering mirror. The analysis is vastly simplified from the myriad of complex issues encountered in a realistic space lasercom system. Interested readers are referred to Hemmati[16] for a thorough discussion of FSOC optics. Also note that most lasercom terminals are designed with reflective, Cassegrain-like telescopes; the drawings here show refractive optics for simplicity of illustration. Following conventional telescope nomenclature, the region on the expanded-beam side of the telescope is referred to as "object-space" whereas the

small-beam side is called "image-space". The nomenclature is commonly associated with angles, as in "10 mrad in object-space". In addition, FSM displacement angles will occasionally be referred to as "mirror-space". The reader should understand that an angle cited in one space will typically be a different value in a second space.

Specifically, the algebraic relationships between the fast steering mirror angle (θ_{FSM}), image space angle (θ_{IS}), and the object-space angle (θ_{OS}) are expressed below where M is the telescope magnification. The sign is deliberately left ambiguous as it depends upon the specific optical system implementation.

$$\theta_{IS} = 2\theta_{FSM} \tag{2.8}$$

$$\theta_{OS} = \pm\frac{1}{M}\theta_{IS} = \pm\frac{2}{M}\theta_{FSM} \tag{2.9}$$

Thus, for a telescope magnification of 15X (equivalent to the MLCD telescope), the FSM must move 7.5 μrad to counteract every 1 μrad of optical table displacement. The resulting FSM displacement PSD is determined from the optical table jitter PSD by multiplying by the square of the optical gain:

$$\mathrm{PSD}\big(\theta_{FSM}(t)\big) = \left|\frac{M}{2}\right|^2 \mathrm{PSD}\big(\theta_{OT}(t)\big). \tag{2.10}$$

The perfect rejection of disturbance motion implied by the equations above is not possible for several reasons, such as sensor noise and quantization, sensor errors, and control effort saturation. One of the greatest contributors to imperfect disturbance compensation is limited control bandwidth. Control bandwidth can be restricted by a number of factors like feedback sensor bandwidth, destabilizing structural modes, or digital processing update rate. Later chapters will explore how the sAFSM design addresses these limiting factors while the remainder of this section focuses on determining a minimum acceptable bandwidth based on pointing requirements.

A simple block diagram of a single-axis FSM control system is shown in Figure 2-9. Transfer function $G(s)$ is a model of the fast steering mirror and controller dynamics combined. $G(s)$'s output is the FSM's local displacement angle θ_{FSM} (that is, the

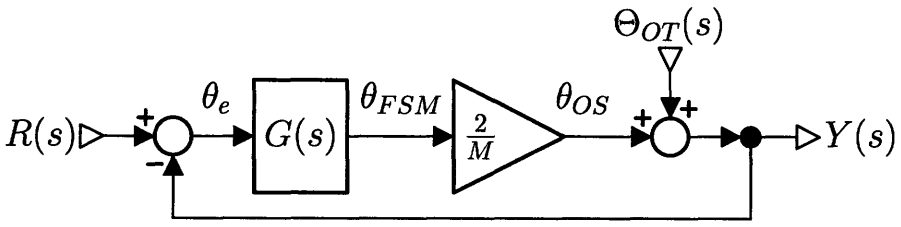

Figure 2-9: Simple FSM Control System Block Diagram

angle with respect to the FSM's neutral position). A transmit beam is reflected off of the FSM and through a telescope producing an optical gain of $2/M$. The transmit beam local object-space angle θ_{OS} is summed with the inertially referenced optical table jitter signal $\Theta_{OT}(s)$ to yield the inertial transmit beam angle signal $Y(s)$. We assume that a unity gain, infinite bandwidth sensor, the details of which are ignored here, feeds back the transmit beam inertial angle to a junction that subtracts it from an inertial command angle signal $R(s)$.

Assume that $G(s)$ is the product of a simple plant transfer function $P(s)$, given in equation (2.11), and proportional+lead controller $C(s)$, given in equation (2.12).

$$P(s) = \frac{1}{s^2 I_{FSM}} \tag{2.11}$$

Variable I_{FSM} is the fast steering mirror's rotational inertia about the actuated axis. For bandwidth specification purposes, the double integrator plant model in (2.11) is a simplified but reasonable approximation of the FSM dynamics. The fast steering mirror should behave like a force-actuated inertia over much of the relevant frequency range. Where it doesn't, at low frequencies for example, compensation will typically be added to shape the magnitude response into something like $1/s^2$.

$$C(s) = K\frac{\alpha Ts + 1}{Ts + 1} \tag{2.12}$$

Controller variables α and T determine the lead compensator's maximum phase and frequency at maximum phase respectively for $\alpha > 1$ [32]. Constant K is the controller's proportional gain. For convenience, the system's open-loop dynamics are

concatenated into a loop transmission transfer function $LT(s)$ below:

$$LT(s) \equiv G(s)\frac{2}{M} = C(s)P(s)\frac{2}{M} = K\frac{\alpha Ts+1}{Ts+1}\frac{1}{s^2 I_{FSM}}\frac{2}{M}. \tag{2.13}$$

Let the controller constants be set such that the loop transmission unity magnitude crossover frequency (the frequency at which $|LT(s)|$ decreases below unity) is ω_{OLX} in $^{rad}/_{s}$ ($f_{OLX} = \omega_{OLX}/2\pi$ in hertz). Note that for second-order or approximately second-order systems like the assumed $G(s)$, the closed-loop bandwidth is roughly one and a half times (1.5×) the open-loop crossover frequency. Also, the phase response of $LT(s)$ peaks with a maximum value of -150° at ω_{OLX}, corresponding to a phase margin of 30°. For a robust controller design, 30° is about the minimum acceptable phase margin. I've chosen to use the lower-bound for phase margin because it is the conservative case for specifying FSM acceleration and because control system designers tend to push bandwidth performance to the phase margin limit (see, for example, Kluk's thesis[22]). Functions for calculating the controller constants as a function of open-loop crossover frequency are given below:

$$\alpha = -\frac{\sin(\phi)+1}{\sin(\phi)-1}, \tag{2.14}$$

$$T = \frac{1}{\omega_{OLX}\sqrt{\alpha}}, \tag{2.15}$$

$$K = \frac{\omega_{OLX}^2 I_{FSM} M}{2\sqrt{\alpha}}, \tag{2.16}$$

where ϕ is the lead compensator maximum phase, equal to $\pi/6$ rad [30°]. Bode diagrams of $LT(s)$ for several values of f_{OLX} are plotted in Figure 2-10. The thin, dashed lines in the magnitude plot show 0° phase margin responses to emphasize the curves in the 30° phase margin solid traces.

The following expression for $\Theta_e(s)$, the Laplace s-domain transmit beam object space error, is derived from block diagram 2-9:

$$\Theta_e(s) = R(s) - Y(s) = R(s) - \left(\Theta_{OT}(s) + \frac{2}{M}G(s)\Theta_e(s)\right). \tag{2.17}$$

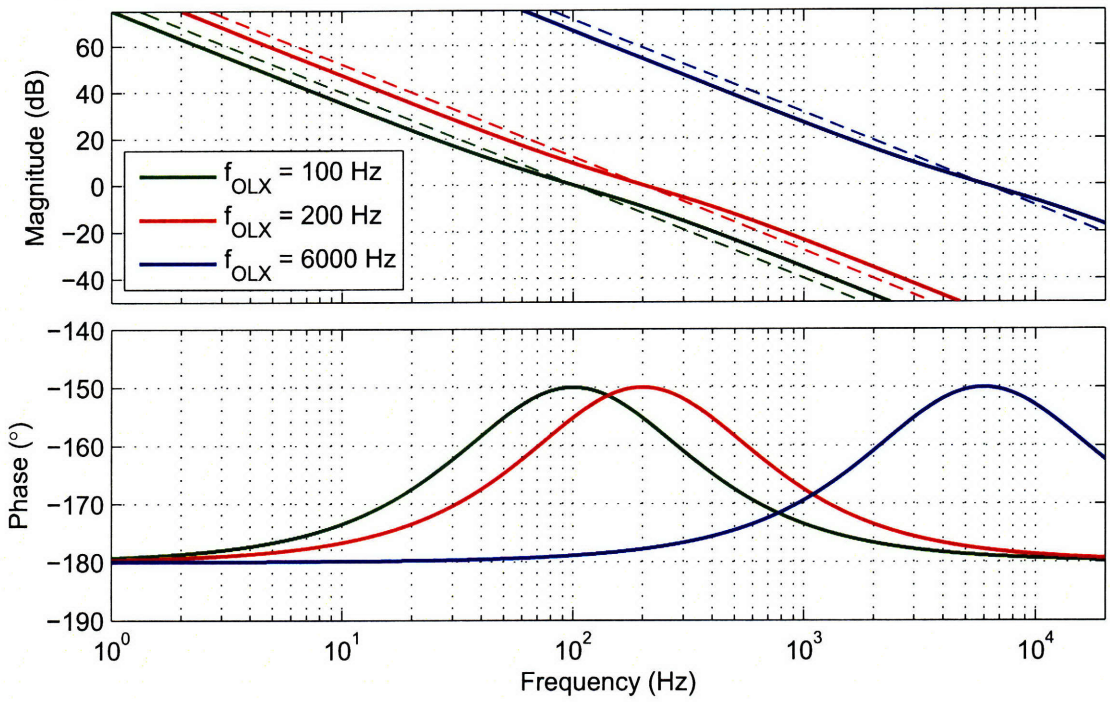

Figure 2-10: Simple FSM Loop Transmission Bode Plot

Manipulating (2.17) to isolate $\Theta_e(s)$ on the left-hand side and substituting $LT(s)$ for $2/M \cdot G(s)$ yields:

$$\Theta_e(s) = \big(R(s) - \Theta_{OT}(s)\big)\frac{1}{1+LT(s)}. \tag{2.18}$$

Assume that the beam's target is aligned with the inertial reference. The command, in this case, will be null. Dividing the resulting equation by $\Theta_{OT}(s)$ gives the active attenuation transfer function between the disturbance and the residual pointing error. The transfer function is assigned the symbol A:

$$A(s) \equiv \frac{\Theta_e(s)}{\Theta_{OT}(s)} = \frac{-1}{1+LT(s)}. \tag{2.19}$$

In order to reduce the residual pointing error, the magnitude of $A(s)$ should be small ($\ll 1$) over the frequency range in which the optical table disturbance is significant. Consequently, per (2.19), the magnitude of $LT(s)$ must be large ($\gg 1$) over the same frequency range. Figure 2-10 shows that doubling the controlled FSM's open-loop crossover frequency quadruples (increases by $\approx$12 dB) the magnitude of

$LT(s)$. Thus, increasing open-loop crossover frequency improves active attenuation performance.

The PSD of the object-space error angle is found by multiplying the optical table disturbance PSD by the square of the magnitude of $A(s)$:

$$\mathrm{PSD}\big(\theta_e(t)\big) = \big|A(s = \mathrm{j}2\pi f)\big|^2 \,\mathrm{PSD}\big(\theta_{OT}(t)\big). \tag{2.20}$$

Figure 2-11 is a combination PSD and cumulative RMS plot of the residual pointing error for a system with a 150 Hz passive vibration isolator and an active FSM with 100 Hz (green trace) or 500 Hz (red trace) open-loop crossover frequency. A trace for a passive-only system (blue) is included for comparison.

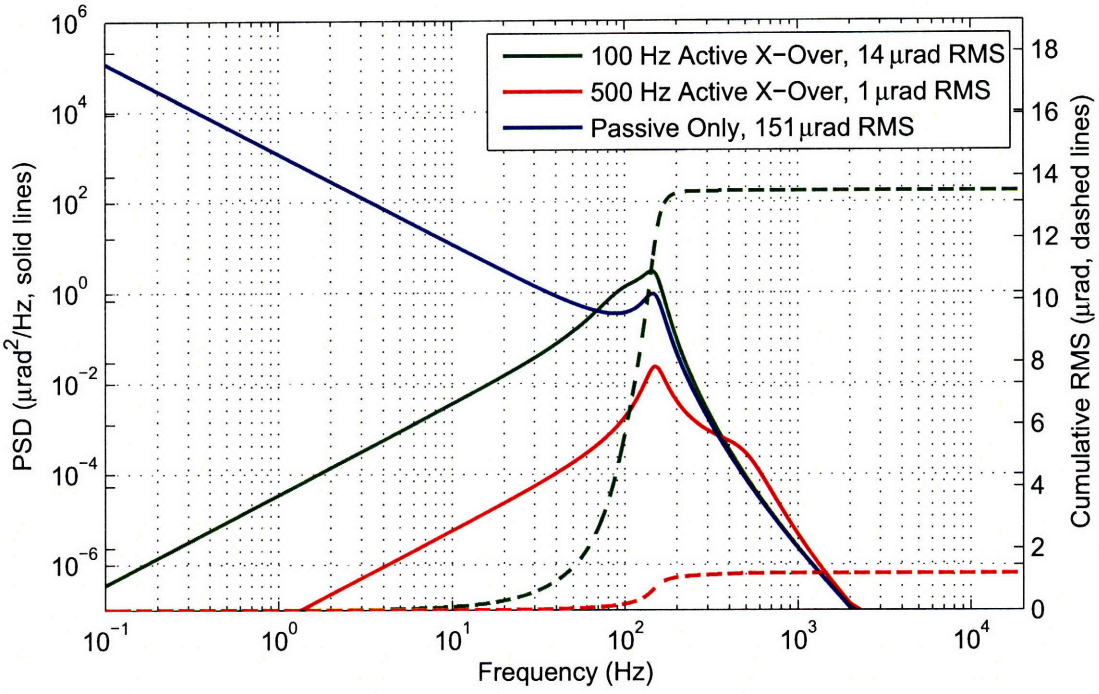

Figure 2-11: Residual Beam Jitter PSD with Active and Passive Rejection

The figure clearly shows that active rejection greatly reduces the beam jitter - from 151 µrad RMS to 14 µrad RMS for the FSM with 100 Hz open-loop crossover frequency. Since the 500 Hz FSM is shown to further reduce the jitter to 1 µrad RMS, the plot supports the above statement that increasing open-loop crossover frequency improves performance. However, while 1 µrad RMS is less than a beamwidth, the per-

formance does not meet the 40 nrad requirement. Thus, the FSM open-loop crossover frequency must be increased beyond 1000 Hz - but by how much?

Figure 2-12 provides the answer. It is a plot of the residual jitter as a function of the FSM open-loop crossover frequency. Traces for the nominal 150 Hz, the MLCD 20 Hz, and an unreasonably stiff (>20 kHz) vibration isolation systems are shown. The thin red line denotes the 40 nrad requirement. Comparing the curves for the different vibration isolators reveals that softer isolators relax the bandwidth requirement placed upon the FSM design. Whereas the benefit of the vibration isolators was masked in Figure 2-7, it is now apparent. Observe that for the stiff isolator case (i.e. the optical table hard-mounted to the spacecraft), the jitter performance doesn't meet the specification even with a 20 kHz FSM.

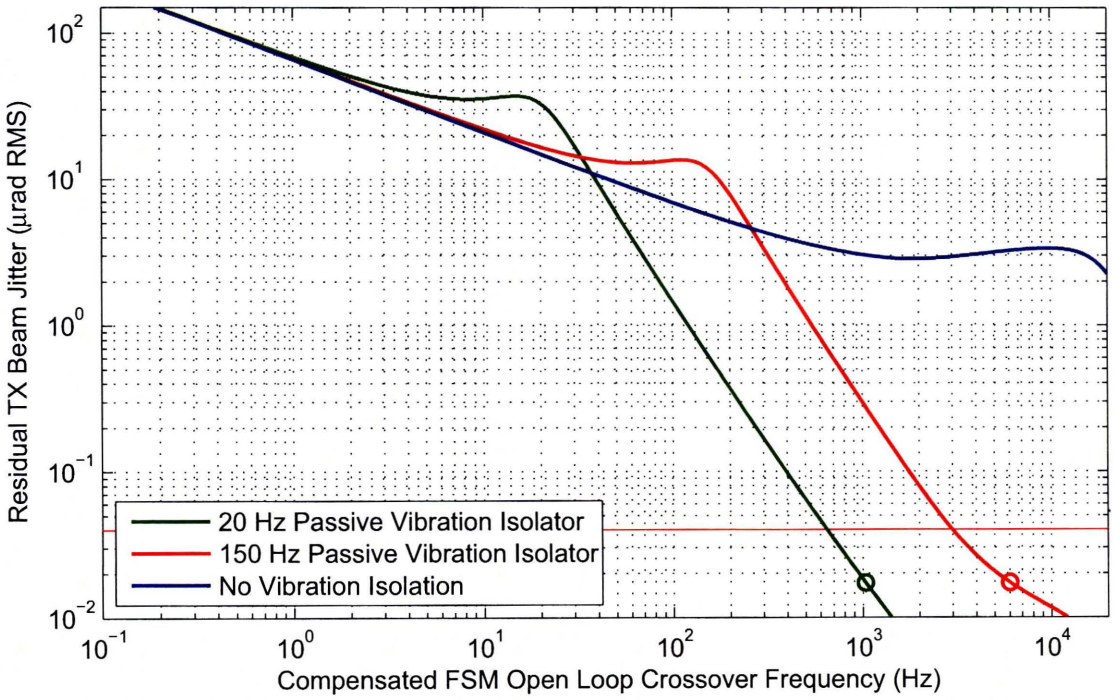

Figure 2-12: Residual Beam Jitter RMS as a Function of Compensated FSM Open Loop Crossover Frequency

The 150 Hz curve intersects the requirement line at approximately 3 kHz. Adding margin, the sAFSM open-loop crossover frequency goal is set at 6 kHz and is marked with a red circle in the plot. Alternatively, using the approximation that closed-loop bandwidth is 1.5 times the open-loop crossover frequency, the sAFSM closed-loop

bandwidth requirement is 9 kHz. Note that for a soft, 20 Hz vibration isolator, the same level of residual jitter is achieved with a 1.03 kHz open-loop crossover frequency FSM (marked with a green circle).

2.4 FSM Acceleration

Fast steering mirror acceleration is, of course, the second derivative of FSM displacement. Referring back to Figure 2-9, FSM displacement is the output of the $G(s)$ block, which models the combined FSM and compensator dynamics. Instead of manipulating the block diagram again to solve for $\Theta_{FSM}(s)$, the equations for $\Theta_e(s)$ found in the previous section are leveraged here as a shortcut. FSM acceleration is determined by transforming $\Theta_e(s)$ through $G(s)$ and then by multiplying by s^2, the second derivative in the Laplace domain (assuming the function is zero-valued at t=0). Using (2.13) and (2.19), an expression for $\ddot{\Theta}_{FSM}(s)$ is thus:

$$\ddot{\Theta}_{FSM}(s) = s^2 G(s)\Theta_e(s) = s^2 LT(s)\frac{M}{2}A(s)\Theta_{OT}(s) = s^2\frac{M}{2}\frac{-LT(s)}{1+LT(s)}\Theta_{OT}(s). \tag{2.21}$$

Dividing (2.21) by $\Theta_{OT}(s)$ gives the transfer function from optical table disturbance to mirror acceleration, assigned to variable F:

$$F(s) \equiv \frac{\ddot{\Theta}_{FSM}(s)}{\Theta_{OT}(s)} = s^2\frac{M}{2}\frac{-LT(s)}{1+LT(s)}. \tag{2.22}$$

The power spectral density of the FSM acceleration is found, as before, by multiplying the optical table disturbance PSD by the squared magnitude of the above transfer function:

$$\mathrm{PSD}\big(\ddot{\theta}_{FSM}(t)\big) = \big|F(s = \mathrm{j}2\pi f)\big|^2\,\mathrm{PSD}\big(\theta_{OT}(t)\big). \tag{2.23}$$

Figure 2-13 is a plot of the power spectral density (solid lines) and cumulative RMS (dashed lines) of the compensated fast steering mirror's acceleration. The plot includes traces for three cases: the nominal 150 Hz vibration isolation system with a

6 kHz open-loop crossover frequency FSM, a 20 Hz isolation system and a 1.03 kHz FSM, and a hard-mounted optical table with a 20 kHz FSM.

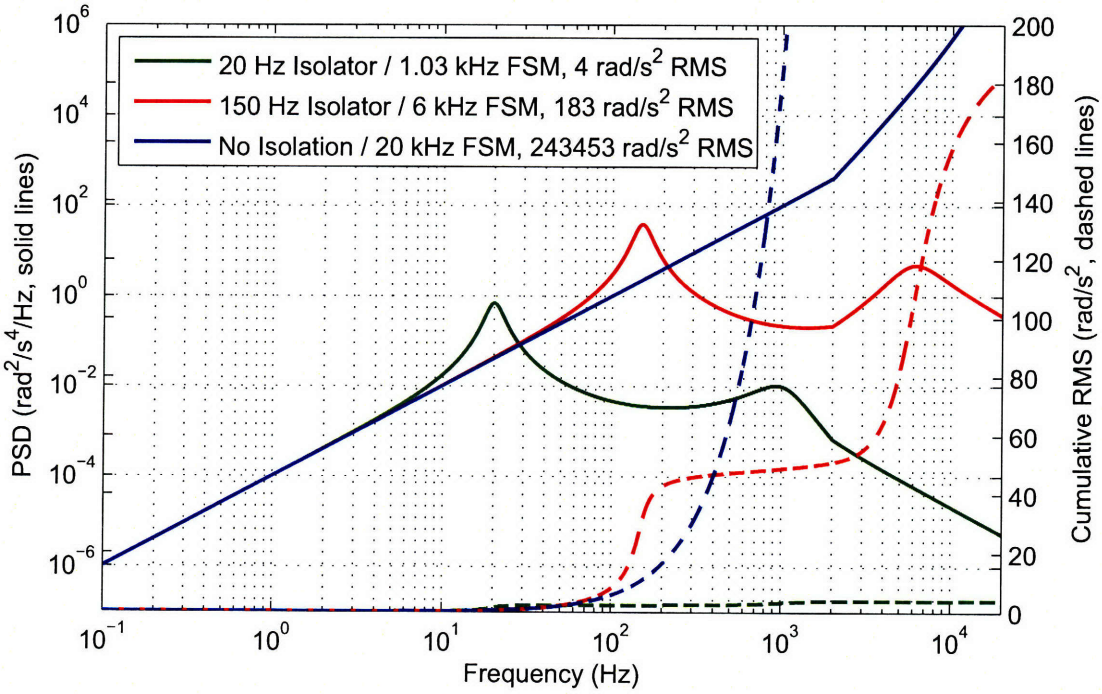

Figure 2-13: FSM Acceleration Power Spectral Density and Cumulative RMS

The RMS acceleration value for the 150 Hz isolation / 6 kHz FSM case is 183 $^{rad}/_{s^2}$. If the required acceleration is assumed to be zero-mean with a normal distribution, then the maximum expected FSM acceleration is 604 $^{rad}/_{s^2}$ (3.3σ; 99.9%). The sAFSM angular acceleration requirement is specified at 10,000 $^{rad}/_{s^2}$, however. Acceleration margin is reserved for compensating for the effects of unmodeled jitter sources in the real system. For example, the assumption that all structures are infinitely stiff is especially unrealistic considering that the telescope and optical bench are light-weighted for space travel. In [13], Doyle shows that non-stiff vibrational modes in the MLCD telescope and isolators contribute significantly to jitter at frequencies between 200 and 800 Hz. Thus, additional FSM acceleration is needed.

The "extra" acceleration performance is also useful if the FSM performs a scanning function. If the FSM is limited to 604 $^{rad}/_{s^2}$ acceleration, for example, each sAFSM axis is able to scan over its full range of travel (see Section 2.5) at a maximum of

39 Hz. At $10\,^{krad}/_{s^2}$, however, the FSM is capable of scanning over the same range at 159 Hz.

2.5 FSM Stroke, Field of View, and Aperture

Minimum FSM stroke is a function of the telescope's field of view (FOV, α_{TS}) and magnification. It is determined using previously established optical relations, equations (2.8), (2.9), by solving for the fast steering mirror angle when the object-space angle is equal to the telescope half-field of view angle (see Figure 2-14).

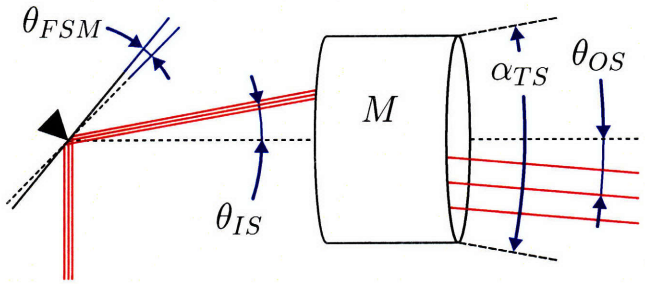

Figure 2-14: FSM Stroke

$$\theta_{OS} = \pm\frac{\alpha_{TS}}{2} = \frac{1}{M}\theta_{IS} = \frac{2}{M}\theta_{FSM} \tag{2.24}$$

$$\theta_{FSM} = \pm\frac{M}{4}\alpha_{TS} \tag{2.25}$$

The assumed telescope FOV is 1.5 mrad (identical to the MLCD system) resulting in a minimum FSM stroke requirement of ±5.6 mrad. However, stroke margin is needed to compensate for optical system alignment error and alignment drift. Therefore, the FSM designed here shall have a minimum stoke of ±10 mrad.

A large FSM field of view (α_{FSM}, see Figure 2-15) is beneficial because it provides the optical system designers with flexibility in choosing the nominal beam incident angle and thus greater freedom in locating optical components. The field of view requirement for the FSM designed in this thesis is 100°, giving a 50° maximum incident angle. For comparison, the nominal FSM incident angle in the MLCD optical arrangement is 45°.

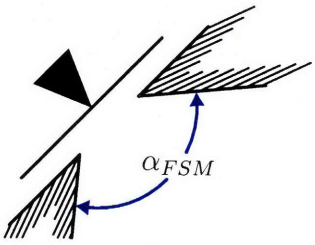

Figure 2-15: FSM Field of View

Minimum mirror aperture is a function of the telescope's aperture, magnification, and the FSM incident angle. The telescope aperture (D_{TS}) limits the maximum diameter of the near-field object-space transmit beam - 30.6 cm [12 in] for the MLCD telescope. The corresponding beam diameter at the small optics side of the telescope is reduced by the telescope magnification. For the 15X telescope, the small-optics beam is concentrated into a diameter just over 20 mm. As illustrated in Figure 2-16, the beam is elongated in one axis when it strikes the fast steering mirror from a non-zero incident angle. The beam is stretched by the secant of the incident angle (θ_I). The resulting minimum FSM aperture is an ellipse with a minor and major diameter (D_{MINOR} and D_{MAJOR} respectively):

$$\begin{aligned} D_{MINOR} &= \frac{D_{TS}}{M}, \\ D_{MAJOR} &= \frac{D_{MINOR}}{\cos\theta_I} = \frac{D_{TS}}{M\cos\theta_I}. \end{aligned} \tag{2.26}$$

Thus, for the MLCD optical system the minimum aperture is 20.4 x 28.9 mm. However, the sAFSM aperture requirement is 16 mm circular. The aperture specification for the FSM designed in this thesis differs from the MLCD system requirement because the sAFSM design objective of dramatically reduced size necessitates reducing mirror aperture.

2.6 Sensor Resolution

FSOC systems typically utilize multiple sources of feedback for fast-steering mirror position control. These sensors can be categorized by the measurement reference

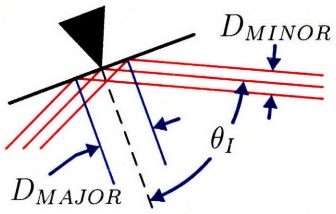

Figure 2-16: FSM Aperture

frame: "local" and "far-field". Far-field sensors measure mirror position with respect to an inertially pseudo-stationary object. Tracking an image of the Earth reflected off of the FSM is one example of a far-field feedback strategy employed by the MLCD project. When viewed from Mars, the Earth appears inertially stationary because of the great distance between the planets. Far-field sensors are usually separate subsystems from the FSM and are therefore not considered in the design of the sAFSM.

"Local" sensors measure mirror position with respect to the FSM body or a reference surface hard-coupled to the FSM (e.g. the optical table). For free-space optical communication applications, local sensors are used primarily for scanning the field of view to acquire a far-field source and/or for generating a pointing offset for transmit beam look-ahead. For either the scanning or pointing offset roles, local mirror position sensor resolution must be approximately equal-to the desired pointing performance (i.e. a fraction of a beamwidth). Referring back to Table 2.1, the MLCD pointing error budget allocates 0.13 µrad (object-space) to point-ahead sensor noise. Converting to mirror-space by multiplying by the inverse optical gain yields the local position sensor noise specification used in this thesis: 0.97 µrad.

Of course, sensor noise specifications are meaningless without designating a corresponding bandwidth. Pointing functions that utilize local sensors for feedback typically require less control bandwidth than the inertial disturbance rejection application. Thus, the local mirror position sensor is given a -3 dB bandwidth requirement of DC to 2 KHz. Note that the sensor bandwidth requirement is considerably less than the FSM bandwidth specification determined in Section 2.3. The high-bandwidth performance of the FSM will be demonstrated with far-field sensor simulators with high sensor bandwidths.

2.7 Size and Performance Requirements Summary

The sAFSM size and performance objectives are summarized in Table 2.3 for convenience.

Table 2.3: sAFSM Size and Performance Requirements

Parameter	Design Goal
Size	$63.5 \times 63.5 \times 36\,\text{mm}$
Mass	0.8 kg
Open-loop Unity Crossover Frequency	6 kHz
Closed Loop -3 dB Bandwidth	*9 kHz*
Maximum Acceleration	$10\,^{\text{krad}}/_{s^2}$
Stroke	± 10 mrad
Field of View	$\pm 50\,^{\circ}$
Aperture	16 mm Circular
Local Sensor Noise	0.97 µrad, 0 to 2 kHz

Chapter 3

Actuator Concept

The genesis of the electromechanical actuator presented in this thesis is Advanced Fast Steering Mirror (AFSM), designed by Dan Kluk for his 2007 Master's thesis project[22]. Kluk's design, in turn, employs four independent "ultra fast motors" (UFM) developed by Xiaodong Lu for his 2005 PhD thesis[26]. Using Lu's terminology, the UFM is a type of hard-linearized normal stress motor[1]. "Hard-linearized" signifies that the electromagnetic topology linearizes the force-per-displacement and force-per-current relationships[2]. "Normal stress" means that the actuator force is generated by the normal (diagonal) elements of the Maxwell stress tensor[3]. This chapter gives a brief overview of the UFM operating principals, shows how Kluk applied the UFM to a fast steering mirror application, and finally presents and analyses the electromechanical concept developed for this thesis.

3.1 Ultra Fast Motor Concept

Both Lu and Kluk provide thorough analyzes of the ultra fast motor in their respective thesis papers. Therefore, this thesis gives only an overview of the concept with an emphasis on the force generation equations. Interested readers should consult these

[1]Motor and actuator are used interchangeably.

[2]Thus, biased current and position feedback are considered "soft-linearized" techniques.

[3]In contrast to motors that rely upon the MST shear stress elements, like conventional rotary motors, or motors that utilize the Lorentz force, as in voice coils.

references for additional detail.

A cross section of the canonical ultra fast motor is shown in Figure 3-1. The red block is the actuator's moving armature; all other items in the figure are stationary. The armature is restricted to $\hat{z}$-axis motion by a bearing (not shown). The orange shape is called a 'C'-core, named for its resemblance to the letter. Both the armature and 'C'-core are made from highly permeable magnetic material. The spaces surrounding the armature (e.g. between the armature and the 'C'-core) are called "air gaps". The yellow shapes represent regions occupied by coiled windings of wire. The coils conduct current around the 'C'-core, inducing the magnetic flux indicated by the blue lines and arrows. Reversing the current direction will, of course, reverse the coil flux direction. A permanent magnet (silver), located between the armature and the "throat" of the 'C', generates a magnetic flux which nominally follows the path indicated by the green lines and arrows. The permanent magnet (PM) flux is also referred to as a "bias" flux since it increases the flux density (flux per unit area) magnitude in the air gaps regardless of the coil current or armature position.

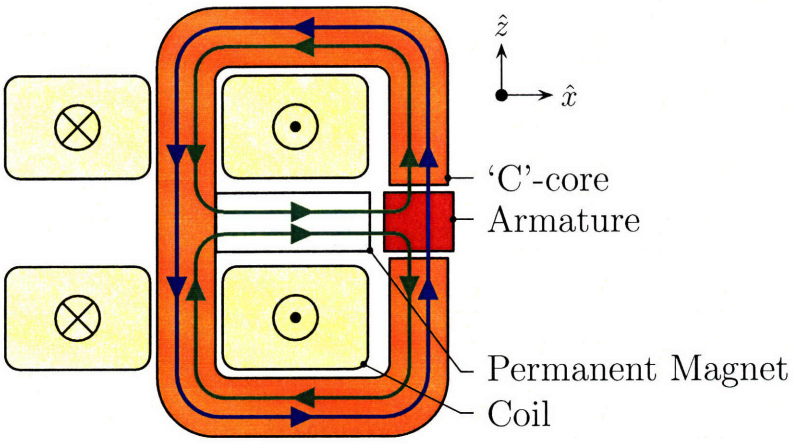

Figure 3-1: Ultra Fast Motor Concept

Figure 3-2 is a magnified view of the armature. The flux from the individual sources (permanent magnet and coils) are combined at each armature face into top air gap flux (Φ_T), bottom air gap flux (Φ_B), and side air gap flux (Φ_S). The forces imparted upon the armature by the magnetic flux can be calculated by integrating the Maxwell stress tensor over the surface S. Ideally, surface S is coincident with the

armature's surface; it is offset in the figure for clarity. Lu additionally derives the forces using energy and co-energy methods in his thesis[26].

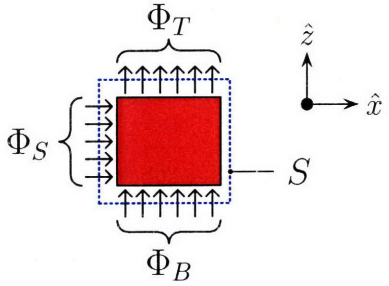

Figure 3-2: Ultra Fast Motor Armature Flux Detail

Since the permeability of the armature is much greater than that of the air surrounding it, the flux vectors can be assumed to be perpendicular to the armature faces (as implied by the figure). Thus, the Maxwell stress tensor's off-diagonal (tangential) elements are zero (we ignore edge effects in this analysis). The Maxwell stress tensor is additionally simplified with the assumption that no electric fields exist along surface S. Furlani[14] shows that for such conditions the force exerted upon the armature is:

$$\mathbf{\Lambda} = \frac{1}{2\mu_0} \oint_S B^2 \hat{\boldsymbol{n}} \mathrm{d}s, \tag{3.1}$$

where $\mathbf{\Lambda}$ is a Cartesian force vector, μ_0 is the permeability of free space, $\hat{\boldsymbol{n}}$ is the vector normal to the surface, and B is the flux density. Performing the integration using $B_k = {}^{\Phi_k}/_{A_k}$, where Φ_k is the total flux over an armature face with area A_k, gives:

$$\mathbf{\Lambda} = \left(\frac{\Phi_T^2}{2\mu_0 A_T} - \frac{\Phi_B^2}{2\mu_0 A_B} \right) \hat{z} + \frac{-\Phi_S^2}{2\mu_0 A_S} \hat{x}. \tag{3.2}$$

Here A_T, A_B, and A_S are the top, bottom, and side areas of the armature respectively. Let both the top and bottom areas be equal to A. The vertical ($\hat{z}$) component of the force vector then simplifies to:

$$F_Z = \frac{1}{2A\mu_0} \left(\Phi_T^2 - \Phi_B^2 \right). \tag{3.3}$$

Note that, because the flux terms are squared, the direction of the flux is irrelevant

for calculating the force.

Using magnetic equivalent circuit analysis, Lu[26] and Kluk[22] show that under the basic assumptions above, the top and bottom air gap fluxes are linear functions of armature $\hat{z}$-axis displacement (z) and coil current (i) in the form:

$$\Phi_T = \alpha i + \beta z + \gamma, \tag{3.4}$$

$$\Phi_B = \alpha i + \beta z - \gamma, \tag{3.5}$$

where α, β, and γ are constants that depend upon actuator geometry (gap length, permanent magnet length and area) and number of coil turns. The constant γ, which has opposite signs in the expressions for top and bottom flux, is the PM bias flux. When (3.4) and (3.5) are substituted into equation (3.3), the nonlinear terms (due to the flux squaring) cancel yielding:

$$\begin{aligned} F_Z &= \frac{1}{2A\mu_0}\big((\alpha i + \beta z + \gamma)^2 + (ai + \beta z - \gamma)^2\big) \\ &= \frac{1}{2A\mu_0}\big((4\alpha\gamma)i + (4\beta\gamma)z\big). \end{aligned} \tag{3.6}$$

Thus, the vertical force on the armature is a linear function of both armature displacement and coil current. Note that both coefficients preceding i and z include the PM bias flux magnitude as a gain factor. Thus, increasing the bias flux gives a more efficient actuator (with respect to current) but also results in greater attraction to the 'C'-core (negative magnetic spring).

3.2 Kluk AFSM Actuator Design

Kluk's AFSM design utilizes four independent UFMs to actuate a fast steering mirror in two rotational degrees of freedom (tip and tilt). Figure 3-3 is a three-dimensional cartoon illustrating the AFSM electromechanical concept, where the dark gray bars between red armatures represent a stiff, non-magnetic, mechanical linkage. Several components in the figure are shown as transparent to reveal detail that would oth-

erwise be obscured. Geometrically opposed UFMs impart a torque on the moving structure by oppositely driving their respective coils. For example, to impart a $+\hat{y}$ torque, the $-\hat{x}$ coil is driven with clockwise (viewed from above) current and the $+\hat{x}$ coil is driven with counterclockwise current.

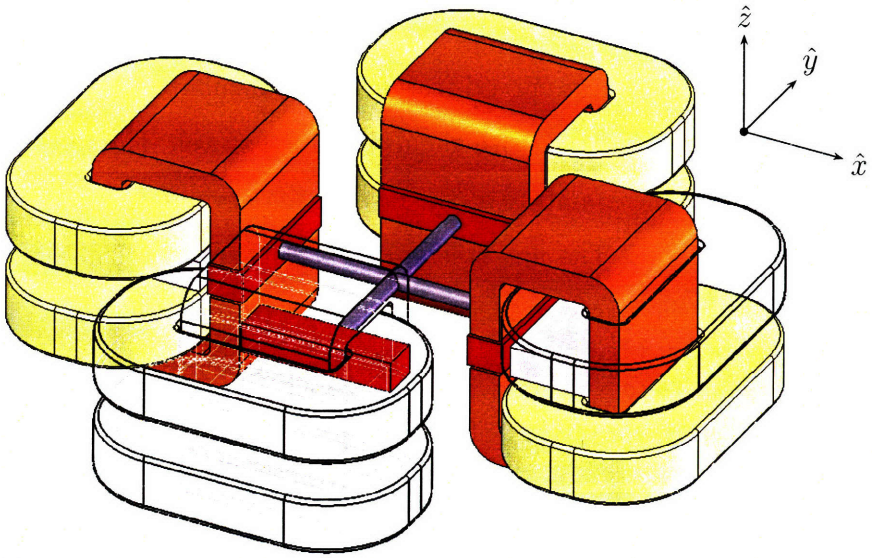

Figure 3-3: Kluk's Advanced Fast Steering Mirror Concept

Let variable r be the radius about the $\hat{z}$-axis from the effective pivot of the armature structure (nominally the center of mass of the four armatures plus connecting mechanical linkages) to the UFMs' force vertically-directed vector. The torque developed by two oppositely driven actuators is thus:

$$T = 2rF_Z = \frac{r}{A\mu_0}\left(\Phi_T^2 - \Phi_B^2\right). \tag{3.7}$$

3.3 Ring Armature Concept

Recall from Section 2.2 that a primary objective of this design effort is to reduce the fast steering mirror size. Simply scaling-down Kluk's design is not a viable solution, however, as it fails to meet the mirror field-of-view requirement and some of its parts cannot be reduced in size. I attempted to shrink the AFSM size by reconfiguring the shape and locations of components, but that also proved unsatisfactory for various

reasons (see Section 4.2.1). Finally, several alternative flux steering topologies were considered. One of these concepts, henceforth referred to as the "ring armature" concept, appeared promising and was developed further in this thesis.

Two key insights led to the ring armature electromagnetic topology. First, fundamentally, the flux steering actuator concept requires the bias flux to "enter" a surface surrounding the armature in a direction perpendicular to the armature travel and "exit"[4] the surface in parallel with the direction of travel. The bias flux doesn't necessarily need to exit the armature at the face with a normal pointing into the 'C'-core, as in the Kluk design. The flux steering equations are identical if the bias flux exits the armature at the opposite face, for example, or in any of the other infinite number of directions perpendicular to the alternating flux. Secondly, each magnetic junction with the armature requires a considerable volume of material (steel or permanent magnet) to guide the flux in the desired direction. And, the location of such additional material is likely in a region that is either space-constrained or could be occupied by some other essential FSM component. In the Kluk design for example, the biasing permanent magnet occupies volume that could have been filled with coil windings. The ring armature concept exploits these ideas to reduce the FSM size.

Note that unlike Lu's and Kluk's actuator designs, the ring armature electromagnetic concept has flux paths which are inherently three dimensional. Hence, illustrating the device's principles of operation is somewhat more challenging.

Figure 3-4 is a three-dimensional cartoon of the ring armature concept's electromagnetic components. The continuous red ring in the center of the drawing is the moving armature (hence the concept's "ring armature" name). All other parts in the figure are stationary. The ring is surrounded by an even number of evenly spaced 'C'-cores - four, in this case - positioned such that the gap in the 'C' is aligned with the ring's flat faces.[5] Nominally equal air gaps separate the 'C'-cores' cut faces from the ring (see figure inset). Note that the ring will occasionally be called the

[4] "Enter" and "exit" are in quotations because they imply that flux direction is relevant, which is not the case.

[5] The projections of the 'C'-cores' cut faces lie entirely within the ring's flat (top and bottom) faces.

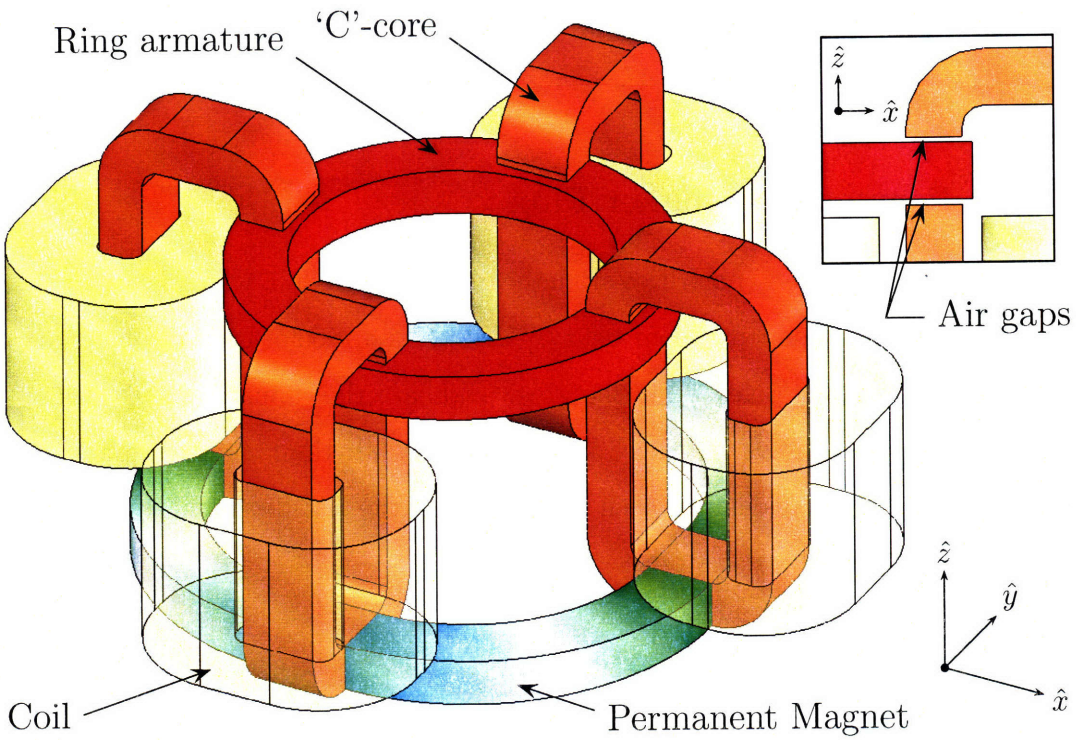

Figure 3-4: Ring Armature Concept

"ring-core". When used alone, "core" or "cores" shall refer to both the ring and the 'C'-cores. Curved permanent magnets (blue/white/green gradient) span the space between adjacent 'C'-cores. The yellow shapes represent wire coils wound around the outside segment of each 'C'-core. The two coil windings closest to the viewer are shown partially transparent to expose the interface between the permanent magnets and 'C'-cores beneath them. The coil windings could extend all the way to the inside top of the 'C'-cores; they are shortened here for illustration purposes.

In the analysis below, the ring and 'C'-cores are assumed to be made from infinitely permeable, zero conductivity soft magnetic material. Realistic properties of magnetically soft metals and the actual selection of the sAFSM's core material are discussed in a subsequent chapter. The coil windings are made from an electrically conductive material such as copper. We assume that windings, the actuator's supporting structure (not shown), and the surrounding environment have a permeability equal to that of free-space (μ_0). Lastly, the slope of the permanent magnets' B-H

curve in the second quadrant is assumed to be equal to μ_0, as is typical of rare-earth type magnets.

3.3.1 Permanent Magnet Flux

The permanent magnets' polarities are indicated in Figure 3-5, which is a view of the electromagnetic components from below. The poles are color-coded: blue ends are the magnets' "north" poles while the green ends are the "south" poles. Note that "like" poles face each other at each of the 'C'-cores. If the magnets were arranged such that "unlike" poles met at each 'C'-core, then the PM flux would just uselessly encircle the base of the actuator.

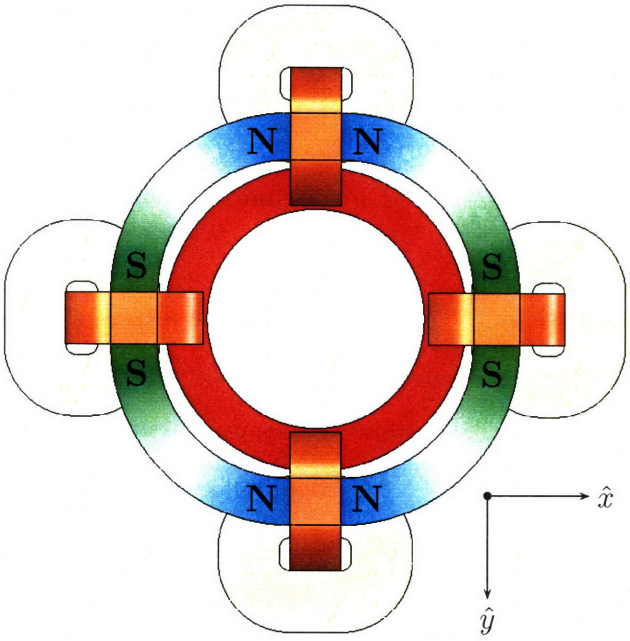

Figure 3-5: Permanent Magnet Polarity (viewed from below)

Ignoring the coils for a moment, Figure 3-6 shows the notional paths of the bias magnetic flux generated by the permanent magnets. Only half of the paths are drawn for clarity as the most distant paths would be obscured by components in the foreground. If plotted, the hidden paths would be a reflection of the visible paths about the $\hat{x}$-$\hat{z}$ plane. Also, only the nominal flux lines are shown; that is, the leakage paths are ignored. Tracing the paths starting with the $-\hat{y}$ 'C'-core, the PM flux lines

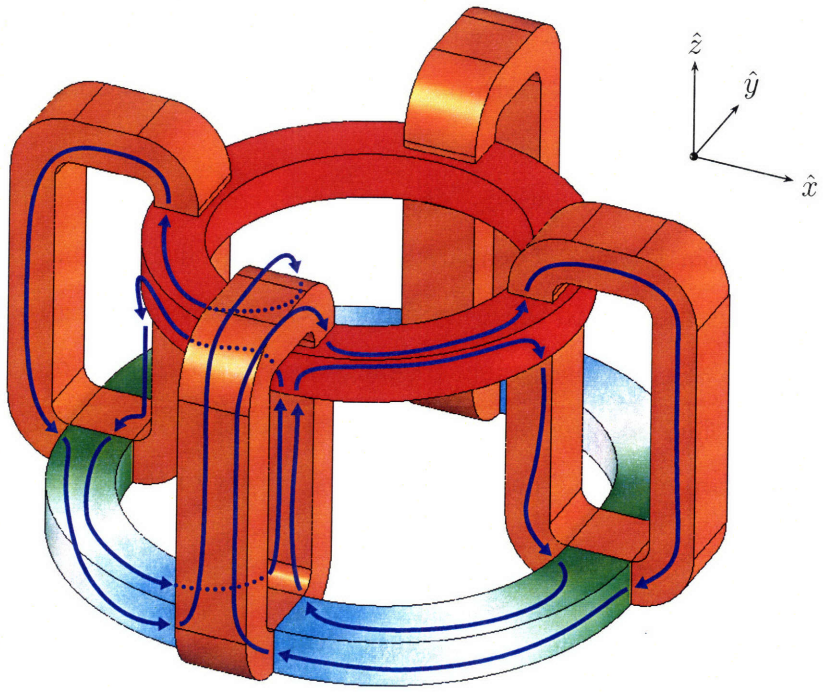

Figure 3-6: Nominal Permanent Magnet Flux Lines

from "like"-facing magnets converge in the base of the 'C'-core. Since the permeability of the core is assumed to be infinite and the air gaps are identical, an equal amount of flux travels up the inside and outside segments of the 'C', even through the outside path length is longer. The flux then jumps across the gaps and into the ring-core. The flux separates and flows along the ring to the $-\hat{x}$ and $+\hat{x}$ 'C'-cores. It then jumps back across the air gaps, again balanced equally between the top and bottom, and into the 'C'-core. The paths are closed with the flux running down both segments of the $\pm\hat{x}$ 'C'-cores and reentering the permanent magnets. Actuator forces will be discussed in later sections; as a preview, note that in the centered position shown, the PM bias flux does not exert any net force upon the armature because the top and bottom gap lengths, areas, and flux densities are equal. If the ring rotates about the $\hat{x}$ or $\hat{y}$ axes or translates along $\hat{z}$, then the PM bias flux will generate torques and vertical force respectively.

An alternative and perhaps simpler mental model of the PM flux is that the "like"-facing permanent magnets effectively turn each 'C'-core into a magnet with a polarity

equal to that of the mating PM faces. The $-\hat{y}$ 'C'-core is treated as a "north" pole magnet, for instance. Flux flows through the air gaps and ring from the "north" 'C'-cores to the "south" 'C'-cores.

Figure 3-6 also illustrates how the ring armature concept takes advantage of the key insights mentioned above. Compared with the Kluk design, the concept eliminates one magnetic interface to the armature per 'C'-core by directing the bias flux to the adjacent 'C'-cores. The permanent magnets are relocated to an otherwise underutilized section of the FSM, freeing up volume inside of the 'C'-cores for coil windings and enabling the top of the 'C'-core to be brought closer to the armature.

3.3.2 Coil Flux

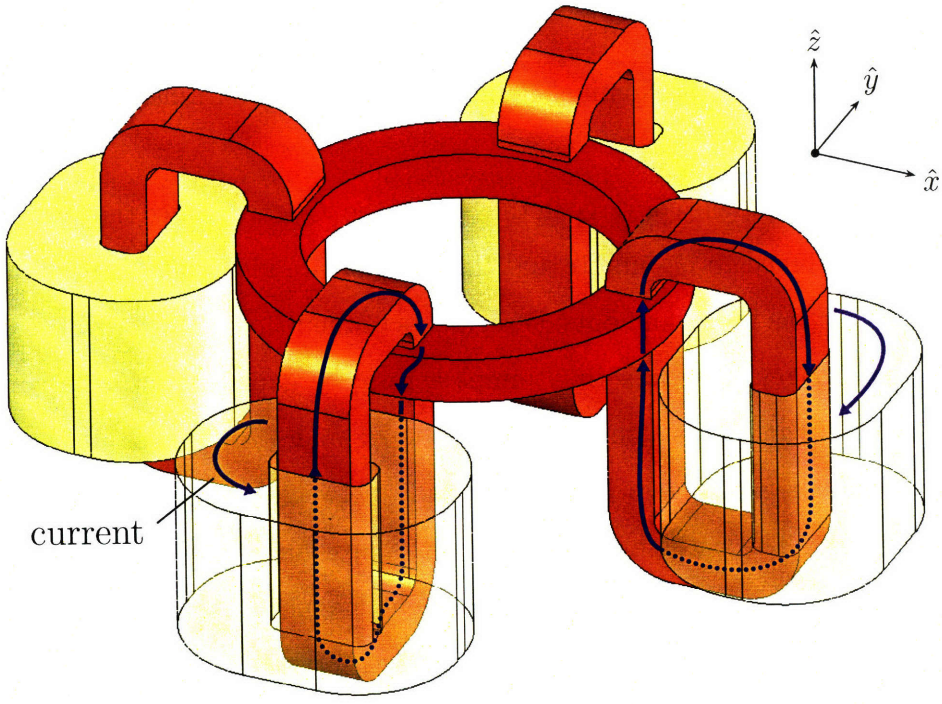

Figure 3-7: Nominal Coil Flux Lines

When energized, the coils generate a magnetic field with nominal flux paths shown in Figure 3-7. The permanent magnets have been hidden in the figure to reflect their free-space-like response to external magnetic fields (a consequence of their μ_0 demagnetization curve slope). In this figure, the coils wrapped around the $-\hat{x}$ and

$+\hat{y}$ 'C'-cores are turned-off (no current flow). Thus, those coils do not produce flux lines; which is convenient as they would have been difficult to illustrate. If the coils were energized, the flux paths would be similar to those for the $+\hat{x}$ and $-\hat{y}$ 'C'-cores.

The polarity of the magnetic field depends, of course, upon the direction of the coil's current flow according to the familiar right-hand rule. Let's follow the course of the flux generated by the $-\hat{y}$ coil. The counterclockwise current (viewed from above) creates an upward (by convention) flux that travels through the top segment of the 'C'-core. The flux jumps the top gap, flows through the armature, and then jumps the bottom gap to the lower inside segment of the 'C'-core. Ideally, none of the coil flux travels through the ring to the adjacent 'C'-cores since the flux would have to return via a lengthy path through air (or through the PM, which acts like air to the coil flux). In reality, a small amount of leakage flux will take such a route through the actuator. Finally, the flux returns to the coil by traveling through the lower segment of the 'C'-core.

3.3.3 Combined PM and Coil Flux

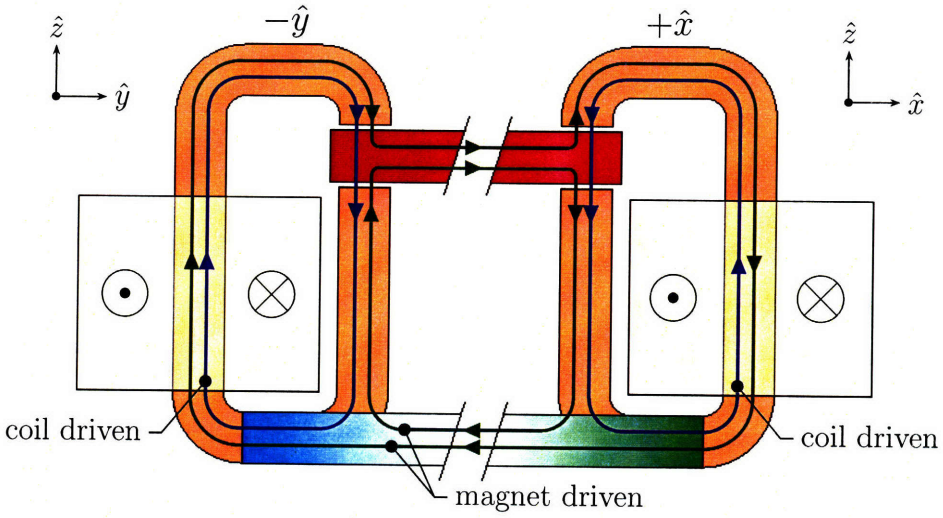

Figure 3-8: Nominal PM and Coil Flux Lines Between $-\hat{y}$ & $+\hat{x}$ 'C'-cores

Illustrating the combined permanent magnet and coil flux on a three-dimensional drawing is difficult. Therefore, Figure 3-8 is the composite of two planar views of

the ring armature concept showing the $-\hat{y}$ and $+\hat{x}$ 'C'-cores. The other 'C'-cores are hidden in this figure. Both of the $-\hat{y}$ and $+\hat{x}$ 'C'-core coils are driven with a counterclockwise current when viewed from above (i.e. the currents rotate about the $+\hat{z}$ axis per right-hand-rule convention). The nominal permanent magnet flux lines are traced with the green lines and arrows and the nominal coil-induced flux lines are traced with blue lines and arrows.

3.3.4 Magnetic Equivalent Circuit

Figure 3-9 is a magnetic equivalent circuit diagram[6] of the ring armature concept. Leakage flux is, once again, ignored. The circuit nodes, labeled with triangles in the circuit diagram, are mapped to physical locations in the actuator in Figure 3-10. Node zero, for example, is the entire ring core. $\mathscr{R}_{+\hat{x}T}$ is the top air gap reluctance for the $+\hat{x}$ 'C'-core, $\mathscr{R}_{+\hat{x}B}$ is the bottom air gap reluctance for the $+\hat{x}$ 'C'-core, $\mathscr{R}_{-\hat{y}T}$ is the top air gap reluctance for the $-\hat{y}$ 'C'-core, and so on. The permanent magnets are modeled as flux sources in parallel with reluctances (a "Norton equivalent" representation). The PM flux sources and reluctances are labeled Φ_{SN} and $\mathscr{R}_{SN}$ respectively where S and N denote which 'C'-cores the permanent magnet spans from "south" to "north" pole. For instance, $\Phi_{+\hat{x}-\hat{y}}$ is the flux generated by the PM between the $+\hat{x}$ and $-\hat{y}$ 'C'-cores. Coil windings are modeled as magnetomotive force (MMF) sources (a "Thévenin equivalent" representation with zero source impedance) and are labeled $\mathscr{F}_a$ where a identifies the 'C'-core around which the coil is wrapped (e.g. $\mathscr{F}_{-\hat{y}}$ is the MMF generated by the coil wrapped around the $-\hat{y}$ 'C'-core).

Unfortunately, it is not possible to make the circuit diagram planar (free of crossing wires); thus, the loop analysis technique for solving circuit unknowns, the author's preferred method, is unsuitable. The Modified Nodal Analysis[18] (MNA) technique is employed instead. MNA defines a process for generating a system of $n-1+m$ equations in the matrix form below where n is the number of circuit nodes and m is the number of MMF sources. For the ring armature magnetic circuit, n and m are 9 and 4 respectively (with 40 total circuit branches). The ring core (node 0) is an

[6]Some authors call magnetic equivalent circuit analysis the "reluctance method".

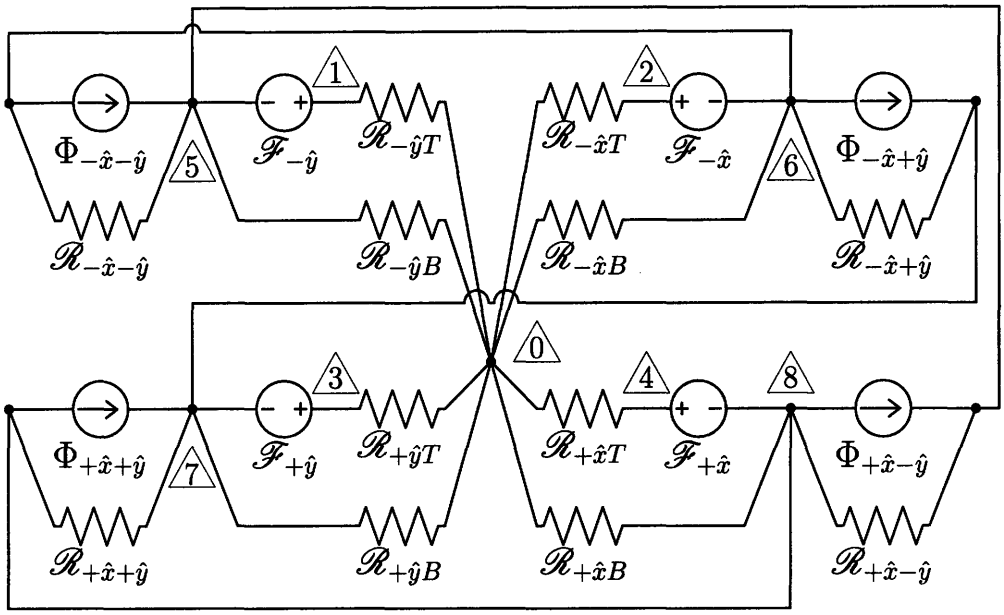

Figure 3-9: Ring Armature Magnetic Equivalent Circuit

obvious choice for the reference ("ground") node since it connects to all other nodes.

$$\mathsf{A}\boldsymbol{x} = \boldsymbol{z} \tag{3.8}$$

$$\begin{bmatrix} \mathsf{Y}_\mathsf{R} & \mathsf{B} \\ \mathsf{C} & \mathsf{D} \end{bmatrix} \begin{bmatrix} \boldsymbol{V} \\ \boldsymbol{I} \end{bmatrix} = \begin{bmatrix} \boldsymbol{J} \\ \boldsymbol{E} \end{bmatrix} \tag{3.9}$$

The "unknowns" vector $\boldsymbol{x}$ represents the MMF at each node with respect to the reference, grouped into $n-1\times1$ subvector $\boldsymbol{V}$, and the flux flowing through each MMF source, collected in the $m\times1$ subvector $\boldsymbol{I}$. Unknown node MMFs are labeled $\mathscr{F}_k$ where k is the node number and unknown MMF source fluxes are designated Φ_a where a once again indicates the coil axis.

$$\boldsymbol{V} = \begin{bmatrix} \mathscr{F}_1 & \mathscr{F}_2 & \mathscr{F}_3 & \mathscr{F}_4 & \mathscr{F}_5 & \mathscr{F}_6 & \mathscr{F}_7 & \mathscr{F}_8 \end{bmatrix}^T \tag{3.10}$$

$$\boldsymbol{I} = \begin{bmatrix} \Phi_{-\hat{y}} & \Phi_{-\hat{x}} & \Phi_{+\hat{y}} & \Phi_{+\hat{x}} \end{bmatrix}^T \tag{3.11}$$

"Excitations" vector $\boldsymbol{z}$ is the concatenation of $n-1\times1$ vector $\boldsymbol{J}$, which represents the flux flowing into each node from the flux sources, and $m\times1$ vector $\boldsymbol{E}$, composed

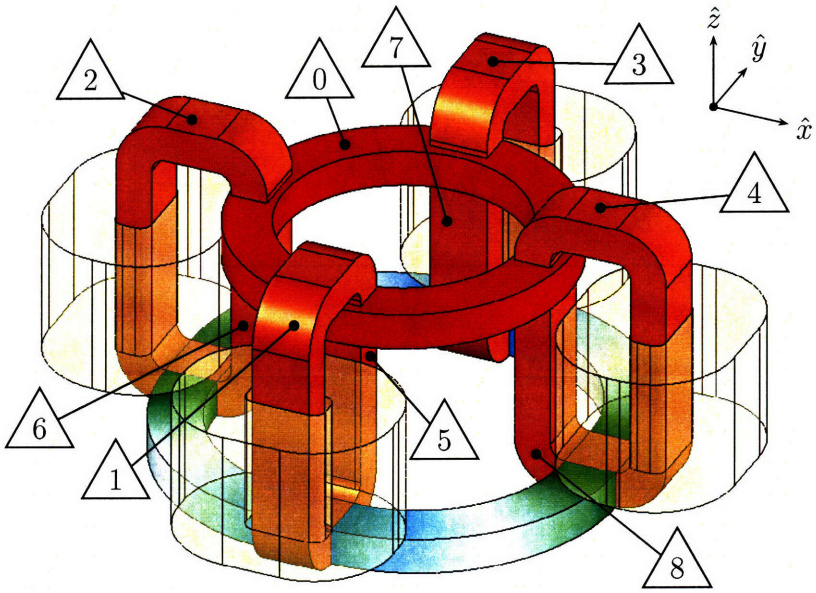

Figure 3-10: Magnetic Circuit Nodes

of the MMF sources' induced MMFs.

$$\boldsymbol{J} = \begin{bmatrix} 0 & 0 & 0 & 0 & \Phi_{-\hat{x}-\hat{y}} + \Phi_{+\hat{x}-\hat{y}} & -\Phi_{-\hat{x}+\hat{y}} - \Phi_{-\hat{x}-\hat{y}} & \Phi_{+\hat{x}+\hat{y}} + \Phi_{-\hat{x}+\hat{y}} & -\Phi_{+\hat{x}-\hat{y}} - \Phi_{+\hat{x}+\hat{y}} \end{bmatrix}^T \tag{3.12}$$

$$\boldsymbol{E} = \begin{bmatrix} \mathscr{F}_{-\hat{y}} & \mathscr{F}_{-\hat{x}} & \mathscr{F}_{+\hat{y}} & \mathscr{F}_{+\hat{x}} \end{bmatrix}^T \tag{3.13}$$

Y_R $(n-1 \times n-1)$ is the node admittance matrix, populated by applying Kirchhoff's current law to each node of the circuit while treating the MMF sources as open terminals. Submatrix B $(n-1 \times m)$, composed entirely of 0 or ± 1 elements, is the partial derivative of the Kirchhoff current equations with respect to the flux through the MMF sources. In other words, B identifies whether MMF source flux flows into or out-from each node. I've adapted the conventional assumption that the MMF source flux flows from the "negative" to "positive" MMF terminal. Submatrix C $(m \times n-1)$ maps the polarities of the MMF sources between nodes. Lastly, since the circuit does not include any dependent current sources, $m \times m$ matrix D is zero.

Many of the elements in A are zero and therefore writing the system of equations

is more concise than printing the matrices. For reference, the full MNA matrices are included in Appendix B. In order to facilitate matrix pivoting, node numbers have been deliberately assigned to produce singletons in the first four rows and columns of matrix A.

Equations (3.14) are Kirchhoff's current law applied at circuit nodes five through eight (MNA matrix rows 5 through 8).

$$\left(\frac{1}{\mathscr{R}_{-\hat{x}-\hat{y}}}+\frac{1}{\mathscr{R}_{+\hat{x}-\hat{y}}}+\frac{1}{\mathscr{R}_{-\hat{y}B}}\right)\mathscr{F}_5-\frac{1}{\mathscr{R}_{-\hat{x}-\hat{y}}}\mathscr{F}_6-\frac{1}{\mathscr{R}_{+\hat{x}-\hat{y}}}\mathscr{F}_8+\Phi_{-\hat{y}}=\Phi_{-\hat{x}-\hat{y}}+\Phi_{+\hat{x}-\hat{y}} \tag{3.14a}$$

$$-\frac{1}{\mathscr{R}_{-\hat{x}-\hat{y}}}\mathscr{F}_5+\left(\frac{1}{\mathscr{R}_{-\hat{x}-\hat{y}}}+\frac{1}{\mathscr{R}_{-\hat{x}+\hat{y}}}+\frac{1}{\mathscr{R}_{-\hat{x}B}}\right)\mathscr{F}_6-\frac{1}{\mathscr{R}_{-\hat{x}+\hat{y}}}\mathscr{F}_7+\Phi_{-\hat{x}}=-\Phi_{-\hat{x}+\hat{y}}-\Phi_{-\hat{x}-\hat{y}} \tag{3.14b}$$

$$-\frac{1}{\mathscr{R}_{-\hat{x}+\hat{y}}}\mathscr{F}_6+\left(\frac{1}{\mathscr{R}_{-\hat{x}+\hat{y}}}+\frac{1}{\mathscr{R}_{+\hat{x}+\hat{y}}}+\frac{1}{\mathscr{R}_{+\hat{y}B}}\right)\mathscr{F}_7-\frac{1}{\mathscr{R}_{+\hat{x}+\hat{y}}}\mathscr{F}_8+\Phi_{+\hat{y}}=\Phi_{+\hat{x}+\hat{y}}+\Phi_{-\hat{x}+\hat{y}} \tag{3.14c}$$

$$-\frac{1}{\mathscr{R}_{+\hat{x}-\hat{y}}}\mathscr{F}_5-\frac{1}{\mathscr{R}_{+\hat{x}+\hat{y}}}\mathscr{F}_7+\left(\frac{1}{\mathscr{R}_{+\hat{x}-\hat{y}}}+\frac{1}{\mathscr{R}_{+\hat{x}+\hat{y}}}+\frac{1}{\mathscr{R}_{+\hat{x}B}}\right)\mathscr{F}_8+\Phi_{+\hat{x}}=-\Phi_{+\hat{x}-\hat{y}}-\Phi_{+\hat{x}+\hat{y}} \tag{3.14d}$$

The expressions above can be simplified significantly by recognizing that the geometries of the permanent magnets are identical and thus their reluctances and applied fluxes are equal. Equations (3.15) and (3.16) define "universal" PM flux and reluctance Φ_{PM} and $\mathscr{R}_{PM}$ respectively.

$$\Phi_{PM}\equiv\Phi_{-\hat{x}-\hat{y}}=\Phi_{-\hat{x}+\hat{y}}=\Phi_{+\hat{x}+\hat{y}}=\Phi_{+\hat{x}-\hat{y}} \tag{3.15}$$

$$\mathscr{R}_{PM}\equiv\mathscr{R}_{-\hat{x}-\hat{y}}=\mathscr{R}_{-\hat{x}+\hat{y}}=\mathscr{R}_{+\hat{x}+\hat{y}}=\mathscr{R}_{+\hat{x}-\hat{y}} \tag{3.16}$$

Substituting Φ_{PM} and $\mathscr{R}_{PM}$ into (3.14) gives:

$$\left(\frac{2}{\mathscr{R}_{PM}}+\frac{1}{\mathscr{R}_{-\hat{y}B}}\right)\mathscr{F}_5-\frac{1}{\mathscr{R}_{PM}}\mathscr{F}_6-\frac{1}{\mathscr{R}_{PM}}\mathscr{F}_8+\Phi_{-\hat{y}}=2\Phi_{PM} \tag{3.17a}$$

$$-\frac{1}{\mathscr{R}_{PM}}\mathscr{F}_5+\left(\frac{2}{\mathscr{R}_{PM}}+\frac{1}{\mathscr{R}_{-\hat{x}B}}\right)\mathscr{F}_6-\frac{1}{\mathscr{R}_{PM}}\mathscr{F}_7+\Phi_{-\hat{x}}=-2\Phi_{PM} \tag{3.17b}$$

$$-\frac{1}{\mathscr{R}_{PM}}\mathscr{F}_6+\left(\frac{2}{\mathscr{R}_{PM}}+\frac{1}{\mathscr{R}_{+\hat{y}B}}\right)\mathscr{F}_7-\frac{1}{\mathscr{R}_{PM}}\mathscr{F}_8+\Phi_{+\hat{y}}=2\Phi_{PM} \tag{3.17c}$$

$$-\frac{1}{\mathscr{R}_{PM}}\mathscr{F}_5-\frac{1}{\mathscr{R}_{PM}}\mathscr{F}_7+\left(\frac{2}{\mathscr{R}_{PM}}+\frac{1}{\mathscr{R}_{+\hat{x}B}}\right)\mathscr{F}_8+\Phi_{+\hat{x}}=-2\Phi_{PM}. \tag{3.17d}$$

Applying Kirchhoff's current law to nodes one through four (MNA matrix rows 1 through 4) yields a comparatively simple set of equations since each of these nodes are connected to "ground" through a single reluctance:

$$\frac{1}{\mathscr{R}_{-\hat{y}T}}\mathscr{F}_1-\Phi_{-\hat{y}}=0 \tag{3.17e}$$

$$\frac{1}{\mathscr{R}_{-\hat{x}T}}\mathscr{F}_2-\Phi_{-\hat{x}}=0 \tag{3.17f}$$

$$\frac{1}{\mathscr{R}_{+\hat{y}T}}\mathscr{F}_3-\Phi_{+\hat{y}}=0 \tag{3.17g}$$

$$\frac{1}{\mathscr{R}_{+\hat{x}T}}\mathscr{F}_4-\Phi_{+\hat{x}}=0. \tag{3.17h}$$

The final set of equations relate the magnetomotive sources to the unknown node MMFs (MNA matrix rows 9 through 12):

$$\mathscr{F}_1-\mathscr{F}_5=\mathscr{F}_{-\hat{y}} \tag{3.17i}$$

$$\mathscr{F}_2-\mathscr{F}_6=\mathscr{F}_{-\hat{x}} \tag{3.17j}$$

$$\mathscr{F}_3-\mathscr{F}_7=\mathscr{F}_{+\hat{y}} \tag{3.17k}$$

$$\mathscr{F}_4-\mathscr{F}_8=\mathscr{F}_{+\hat{x}}. \tag{3.17l}$$

Solving for vector $\boldsymbol{x}$ yields values for the flux through the MMF sources and the magnetomotive force at each circuit node. Determining actuator forces, however, requires knowing the flux through the air gaps. Conveniently, air gap flux is found by dividing the MMF at the 'C'-cores' top and bottom nodes by the top and bottom air gap reluctances respectively. Let $\boldsymbol{\Phi_{AG}}$ be a vector of air gap flux with elements Φ_X where subscript X has the same meaning as the air gap reluctance subscripts (e.g. $\Phi_{-\hat{x}B}$ is the bottom air gap flux at the $-\hat{x}$ 'C'-core). $\boldsymbol{\Phi_{AG}}$ is calculated from $\boldsymbol{x}$ with

the matrix below:

$$\boldsymbol{\Phi_{AG}} \equiv \begin{bmatrix} \Phi_{-\hat{y}T} \\ \Phi_{-\hat{y}B} \\ \Phi_{+\hat{y}T} \\ \Phi_{+\hat{y}B} \\ \Phi_{-\hat{x}T} \\ \Phi_{-\hat{x}B} \\ \Phi_{+\hat{x}T} \\ \Phi_{+\hat{x}B} \end{bmatrix} = \begin{bmatrix} \frac{1}{\mathscr{R}_{-\hat{y}T}} & \cdot & \cdot & \cdot & \cdot & \cdot & \cdot & \cdot & \cdot & \cdot & \cdot \\ \cdot & \cdot & \cdot & \cdot & \frac{1}{\mathscr{R}_{-\hat{y}B}} & \cdot & \cdot & \cdot & \cdot & \cdot & \cdot \\ \cdot & \cdot & \frac{1}{\mathscr{R}_{+\hat{y}T}} & \cdot & \cdot & \cdot & \cdot & \cdot & \cdot & \cdot & \cdot \\ \cdot & \cdot & \cdot & \cdot & \cdot & \cdot & \frac{1}{\mathscr{R}_{+\hat{y}B}} & \cdot & \cdot & \cdot & \cdot \\ \cdot & \frac{1}{\mathscr{R}_{-\hat{x}T}} & \cdot & \cdot & \cdot & \cdot & \cdot & \cdot & \cdot & \cdot & \cdot \\ \cdot & \cdot & \cdot & \cdot & \cdot & \frac{1}{\mathscr{R}_{-\hat{x}B}} & \cdot & \cdot & \cdot & \cdot & \cdot \\ \cdot & \cdot & \cdot & \frac{1}{\mathscr{R}_{+\hat{x}T}} & \cdot & \cdot & \cdot & \cdot & \cdot & \cdot & \cdot \\ \cdot & \cdot & \cdot & \cdot & \cdot & \cdot & \cdot & \frac{1}{\mathscr{R}_{+\hat{x}B}} & \cdot & \cdot & \cdot \end{bmatrix} \boldsymbol{x} \tag{3.18}$$

Since they are in series, the flux through a 'C'-core's top air gap will equal the flux through its MMF source (i.e. $\Phi_{-\hat{y}} = \Phi_{-\hat{y}T}$). Therefore, calculating top air gap flux from the top node MMF, as in rows 1, 3, 5, and 7 of the above, is unnecessary. However, the MMF source and top air gap will not be in series once leakage flux is taken into account. Thus, the above MMF to gap flux transformation is introduced and used now to avoid subsequent confusion or mistakes.

Calculating the difference between top and bottom air gap flux is occasionally interesting because the complexity in the analytic flux expressions tends to cancel out. However, the result isn't very useful since the actuator force depends upon the differences of the squares of the top and bottom flux. The net flux is calculated from the air gap flux vector with the matrix below:

$$\boldsymbol{\Phi_{NET}} \equiv \begin{bmatrix} \Phi_{-\hat{y}T} - \Phi_{-\hat{y}B} \\ \Phi_{+\hat{y}T} - \Phi_{+\hat{y}B} \\ \Phi_{-\hat{x}T} - \Phi_{-\hat{x}B} \\ \Phi_{+\hat{x}T} - \Phi_{+\hat{x}B} \end{bmatrix} = \begin{bmatrix} 1 & -1 & \cdot & \cdot & \cdot & \cdot & \cdot & \cdot \\ \cdot & \cdot & 1 & -1 & \cdot & \cdot & \cdot & \cdot \\ \cdot & \cdot & \cdot & \cdot & 1 & -1 & \cdot & \cdot \\ \cdot & \cdot & \cdot & \cdot & \cdot & \cdot & 1 & -1 \end{bmatrix} \boldsymbol{\Phi_{AG}}. \tag{3.19}$$

The force imparted upon the armature at each 'C'-core is labeled F_a where a denotes the 'C'-core axis. The forces are calculated according to equation (3.3) with the convention that forces in the $+\hat{z}$ direction are positive. The effective pole areas of

each of the air gaps (all 'C'-cores, top and bottom) are assumed to be equal and are given the label A. The individual force elements are concatenated into force vector $\boldsymbol{F}$[7] per the equation below:

$$\boldsymbol{F} \equiv \begin{bmatrix} F_{-\hat{y}} \\ F_{+\hat{y}} \\ F_{-\hat{x}} \\ F_{+\hat{x}} \end{bmatrix} = \frac{1}{2A\mu_0} \begin{bmatrix} \Phi^2_{-\hat{y}T} - \Phi^2_{-\hat{y}B} \\ \Phi^2_{+\hat{y}T} - \Phi^2_{+\hat{y}B} \\ \Phi^2_{-\hat{x}T} - \Phi^2_{-\hat{x}B} \\ \Phi^2_{+\hat{x}T} - \Phi^2_{+\hat{x}B} \end{bmatrix}. \tag{3.20}$$

Summing the force vector gives F_{NET}, the net linear force collectively applied to the armature (in the $+\hat{z}$ direction):

$$F_{NET} \equiv \sum \boldsymbol{F}. \tag{3.21}$$

Assuming each 'C'-core is at distance r from the armature's effective pivot, the torques imparted upon the armature are:

$$T_X \equiv rF_{+\hat{y}} - rF_{-\hat{y}} = r\left(F_{+\hat{y}} - F_{-\hat{y}}\right), \tag{3.22}$$

$$T_Y \equiv rF_{-\hat{x}} - rF_{+\hat{x}} = r\left(F_{-\hat{x}} - F_{+\hat{x}}\right). \tag{3.23}$$

Here T_X and T_Y are the torques about the $\hat{x}$ and $\hat{y}$ axes respectively using right-hand-rule sign convention (see Figure 3-11).

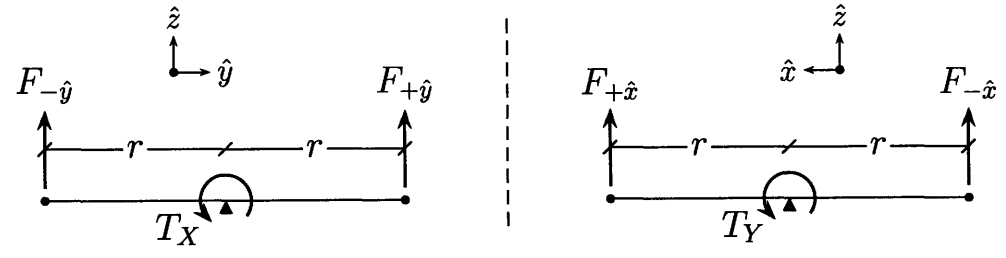

Figure 3-11: Armature Torque Free-Body Diagrams

[7] $\boldsymbol{F}$ is a non-Cartesian vector

The solution to (3.8) simply requires inverting matrix A:

$$\boldsymbol{x} = \mathsf{A}^{-1}\boldsymbol{z}. \tag{3.24}$$

Solving for $\boldsymbol{x}$ symbolically, even with the simplifications given in (3.15) and (3.16), results in equations that are much too lengthy to be useful for parametric analysis. For instance, the numerator of $\mathscr{F}_1$ alone has 100 terms (solved with a computer algebra system). Therefore, further simplifications are required. However, the complete solution for $\boldsymbol{x}$ is useful for numerical analysis and simulations.

3.3.5 Centered Armature

Assume that the openings in the 'C'-cores are all the same length and are aligned such that the openings' top surfaces lie in the same plane[8]. Furthermore, assume that the 'C'-cores' cross sections are equal and that the armature is perfectly centered in the openings. Therefore, all of the air gap reluctances are identical[9]. The value of the centered-armature reluctance is assigned the variable $\mathscr{R}_N$ (subscript 'N' stands for the "nominal" armature position). Plugging in $\mathscr{R}_N$ for each of the individual air gap reluctances in $\boldsymbol{\Phi_{AG}}$ yields a vector for the centered-armature air gap flux:

$$\begin{aligned}\boldsymbol{\Phi_N} \equiv \boldsymbol{\Phi_{AG}}(&\mathscr{R}_{-\hat{y}T} = \mathscr{R}_N,\ \mathscr{R}_{-\hat{x}T} = \mathscr{R}_N,\ \mathscr{R}_{+\hat{y}T} = \mathscr{R}_N,\ \mathscr{R}_{+\hat{x}T} = \mathscr{R}_N,\\ &\mathscr{R}_{-\hat{y}B} = \mathscr{R}_N,\ \mathscr{R}_{-\hat{x}B} = \mathscr{R}_N,\ \mathscr{R}_{+\hat{y}B} = \mathscr{R}_N,\ \mathscr{R}_{+\hat{x}B} = \mathscr{R}_N)\end{aligned}. \tag{3.25}$$

Equations (3.26) give the resulting expression after significant algebraic manipulation (most of which is performed by the Maple®computer algebra system). $\boldsymbol{\Phi_N}$ is interesting because it clearly shows the independent contributions of the coils and permanent magnets to the air gap flux. If the coil-induced MMF is zero (i.e. no coil current), then air gap flux is driven entirely by the permanent magnet (3.26b). Hence, the coefficient preceding the vector in (3.26b) is analogous to the γ term in the UFM flux expressions (3.4) and (3.5). The gain for the PM flux contribution is also

[8]With the implicit assumption that the surface normals are pointed in the same direction

[9]Ignoring leakage flux

interesting as it takes the form of a current divider with input Φ_{PM}, parallel resistor $\mathscr{R}_{PM}$, and output resistor $2\mathscr{R}_N$. However, the origin of the current divider relationship is not obvious from the circuit diagram. This PM flux contribution reappears in much of symbolic analysis of the magnetic circuit. Lastly, note that the flux at each air gap is influenced by the MMF generated by all of the coil windings (in contrast with Figure 3-7) since the modeled PM reluctance isn't infinite[10].

$$\boldsymbol{\Phi_N} = \boldsymbol{\Phi_{N,PM}} + K_{N,MMF}\boldsymbol{\Phi_{N,MMF}} \tag{3.26a}$$

Here $\boldsymbol{\Phi_{N,PM}}$, $K_{N,MMF}$, and $\boldsymbol{\Phi_{N,MMF}}$ are:

$$\boldsymbol{\Phi_{N,PM}} \equiv \Phi_{PM}\frac{\mathscr{R}_{PM}}{\mathscr{R}_{PM}+2\mathscr{R}_N}\begin{bmatrix}1 & 1 & 1 & 1 & -1 & -1 & -1 & -1\end{bmatrix}^T \tag{3.26b}$$

$$K_{N,MMF} \equiv \frac{1}{4\mathscr{R}_N(\mathscr{R}_{PM}+2\mathscr{R}_N)(\mathscr{R}_{PM}+\mathscr{R}_N)} \tag{3.26c}$$

$$\boldsymbol{\Phi_{N,MMF}} = \begin{bmatrix}
(7\mathscr{F}_{-\hat{y}} - \mathscr{F}_{-\hat{x}} - \mathscr{F}_{+\hat{y}} - \mathscr{F}_{+\hat{x}})\mathscr{R}_N^2 + (8\mathscr{F}_{-\hat{y}} - \mathscr{F}_{-\hat{x}} - \mathscr{F}_{+\hat{x}})\mathscr{R}_{PM}\mathscr{R}_N + 2\mathscr{F}_{-\hat{y}}\mathscr{R}_{PM}^2 \\
(-\mathscr{F}_{-\hat{y}} - \mathscr{F}_{-\hat{x}} - \mathscr{F}_{+\hat{y}} - \mathscr{F}_{+\hat{x}})\mathscr{R}_N^2 + (-4\mathscr{F}_{-\hat{y}} - \mathscr{F}_{-\hat{x}} - \mathscr{F}_{+\hat{x}})\mathscr{R}_{PM}\mathscr{R}_N - 2\mathscr{F}_{-\hat{y}}\mathscr{R}_{PM}^2 \\
(-\mathscr{F}_{-\hat{y}} - \mathscr{F}_{-\hat{x}} + 7\mathscr{F}_{+\hat{y}} - \mathscr{F}_{+\hat{x}})\mathscr{R}_N^2 + (-\mathscr{F}_{-\hat{x}} + 8\mathscr{F}_{+\hat{y}} - \mathscr{F}_{+\hat{x}})\mathscr{R}_{PM}\mathscr{R}_N + 2\mathscr{F}_{+\hat{y}}\mathscr{R}_{PM}^2 \\
(-\mathscr{F}_{-\hat{y}} - \mathscr{F}_{-\hat{x}} - \mathscr{F}_{+\hat{y}} - \mathscr{F}_{+\hat{x}})\mathscr{R}_N^2 + (-\mathscr{F}_{-\hat{x}} - 4\mathscr{F}_{+\hat{y}} - \mathscr{F}_{+\hat{x}})\mathscr{R}_{PM}\mathscr{R}_N - 2\mathscr{F}_{+\hat{y}}\mathscr{R}_{PM}^2 \\
-(\mathscr{F}_{-\hat{y}} - 7\mathscr{F}_{-\hat{x}} + \mathscr{F}_{+\hat{y}} + \mathscr{F}_{+\hat{x}})\mathscr{R}_N^2 + (\mathscr{F}_{-\hat{y}} - 8\mathscr{F}_{-\hat{x}} + \mathscr{F}_{+\hat{y}})\mathscr{R}_{PM}\mathscr{R}_N - 2\mathscr{F}_{-\hat{x}}\mathscr{R}_{PM}^2 \\
-(\mathscr{F}_{-\hat{y}} + \mathscr{F}_{-\hat{x}} + \mathscr{F}_{+\hat{y}} + \mathscr{F}_{+\hat{x}})\mathscr{R}_N^2 + (\mathscr{F}_{-\hat{y}} + 4\mathscr{F}_{-\hat{x}} + \mathscr{F}_{+\hat{y}})\mathscr{R}_{PM}\mathscr{R}_N + 2\mathscr{F}_{-\hat{x}}\mathscr{R}_{PM}^2 \\
-(\mathscr{F}_{-\hat{y}} + \mathscr{F}_{-\hat{x}} + \mathscr{F}_{+\hat{y}} - 7\mathscr{F}_{+\hat{x}})\mathscr{R}_N^2 + (\mathscr{F}_{-\hat{y}} + \mathscr{F}_{+\hat{y}} - 8\mathscr{F}_{+\hat{x}})\mathscr{R}_{PM}\mathscr{R}_N - 2\mathscr{F}_{+\hat{x}}\mathscr{R}_{PM}^2 \\
-(\mathscr{F}_{-\hat{y}} + \mathscr{F}_{-\hat{x}} + \mathscr{F}_{+\hat{y}} + \mathscr{F}_{+\hat{x}})\mathscr{R}_N^2 + (\mathscr{F}_{-\hat{y}} + \mathscr{F}_{+\hat{y}} + 4\mathscr{F}_{+\hat{x}})\mathscr{R}_{PM}\mathscr{R}_N + 2\mathscr{F}_{+\hat{x}}\mathscr{R}_{PM}^2
\end{bmatrix} \tag{3.26d}$$

Equation (3.27) is the difference between the top and bottom air gap flux. Note how much of the complexity from equations (3.26) is canceled out. The result -

[10]Repeating the analysis with $\mathscr{R}_{PM} = \infty$ (the condition implied by Figure 3-7) results in the air gap flux depending only upon the PM flux, the "local" coil MMF, and the gap reluctance.

that the difference in flux is equal to the respective coil's MMF divided by one (not two) centered gap reluctance - is identical to the corresponding result for the Kluk geometry.

$$\boldsymbol{\Phi_{N,NET}} = \frac{1}{\mathscr{R}_N}\begin{bmatrix}\mathscr{F}_{-\hat{y}} & \mathscr{F}_{+\hat{y}} & \mathscr{F}_{-\hat{x}} & \mathscr{F}_{+\hat{x}}\end{bmatrix}^T \tag{3.27}$$

The actuator force vector is computed for the centered armature case per eqn. (3.20). The resulting expression is still too complex to give much insight into the system's operating principals. However, it can be split into linear and non-linear (i.e. products of coil MMFs) parts:

$$\boldsymbol{F_N} = \frac{1}{2A\mu_0}\left(\boldsymbol{F_{N,L}} + K_{N,NL}\boldsymbol{F_{N,NL}}\right), \tag{3.28a}$$

where $\boldsymbol{F_{N,L}}$, $K_{N,NL}$, and $\boldsymbol{F_{N,NL}}$ are:

$$\boldsymbol{F_{N,L}} \equiv \Phi_{PM}\frac{\mathscr{R}_{PM}}{\mathscr{R}_{PM}+2\mathscr{R}_N}\frac{2}{\mathscr{R}_N}\begin{bmatrix}\mathscr{F}_{-\hat{y}} & \mathscr{F}_{+\hat{y}} & -\mathscr{F}_{-\hat{x}} & -\mathscr{F}_{+\hat{x}}\end{bmatrix}^T, \tag{3.28b}$$

$$\boldsymbol{K_{N,NL}} \equiv \frac{1}{2\mathscr{R}_N(\mathscr{R}_{PM}+2\mathscr{R}_N)(\mathscr{R}_{PM}+\mathscr{R}_N)}, \tag{3.28c}$$

$$\boldsymbol{F_{N,NL}} \equiv \begin{bmatrix}
\mathscr{F}_{-\hat{y}}\left((2\mathscr{F}_{-\hat{y}}-\mathscr{F}_{-\hat{x}}-\mathscr{F}_{+\hat{x}})\mathscr{R}_{PM}+(3\mathscr{F}_{-\hat{y}}-\mathscr{F}_{-\hat{x}}-\mathscr{F}_{+\hat{y}}-\mathscr{F}_{+\hat{x}})\mathscr{R}_N\right)\\
\mathscr{F}_{+\hat{y}}\left((-\mathscr{F}_{-\hat{x}}+2\mathscr{F}_{+\hat{y}}-\mathscr{F}_{+\hat{x}})\mathscr{R}_{PM}+(-\mathscr{F}_{-\hat{y}}-\mathscr{F}_{-\hat{x}}+3\mathscr{F}_{+\hat{y}}-\mathscr{F}_{+\hat{x}})\mathscr{R}_N\right)\\
-\mathscr{F}_{-\hat{x}}\left((\mathscr{F}_{-\hat{y}}-2\mathscr{F}_{-\hat{x}}+\mathscr{F}_{+\hat{y}})\mathscr{R}_{PM}+(\mathscr{F}_{-\hat{y}}-3\mathscr{F}_{-\hat{x}}+\mathscr{F}_{+\hat{y}}+\mathscr{F}_{+\hat{x}})\mathscr{R}_N\right)\\
-\mathscr{F}_{+\hat{x}}\left((\mathscr{F}_{-\hat{y}}+\mathscr{F}_{+\hat{y}}-2\mathscr{F}_{+\hat{x}})\mathscr{R}_{PM}+(\mathscr{F}_{-\hat{y}}+\mathscr{F}_{-\hat{x}}+\mathscr{F}_{+\hat{y}}-3\mathscr{F}_{+\hat{x}})\mathscr{R}_N\right)
\end{bmatrix}. \tag{3.28d}$$

Despite the complexity, one simple observation can be drawn from centered armature force equations. If the actuators are turned-off (zero induced MMF's), then no forces, and hence no torques, are exerted upon the armature. Further simplifications of the force expressions require making additional assumptions for the magnitudes and directions of the coil drives.

Commonly Driven Coils / $(+\hat{z})$ Force Constant

Continue to assume that the armature is centered in the 'C'-core openings. Additionally assume that all four coils are driven with an equal magnitude ($\mathscr{F}_C$); but, the $+\hat{x}$ and $-\hat{x}$ coils are driven in the opposite direction from their respective polarities indicated in circuit diagram 3-9. This coil drive condition is called "common-mode" since the quantity of flux is common to all 'C'-cores. Thus, the subscript 'C', as in $\mathscr{F}_C$, denotes that the coils are driven in common-mode. The resulting force vector is $\boldsymbol{F_C}$:

$$\boldsymbol{F_C} \equiv \boldsymbol{F_N}\left(\mathscr{F}_{+\hat{y}} = \mathscr{F}_C,\ \mathscr{F}_{-\hat{y}} = \mathscr{F}_C,\ \mathscr{F}_{+\hat{x}} = -\mathscr{F}_C,\ \mathscr{F}_{-\hat{x}} = -\mathscr{F}_C\right). \tag{3.29}$$

Performing the substitutions yields the following relatively simple but still nonlinear vector:

$$\boldsymbol{F_C} = \frac{1}{2A\mu_0}\Phi_{PM}\frac{\mathscr{R}_{PM}}{\mathscr{R}_{PM}+2\mathscr{R}_N}\frac{2}{\mathscr{R}_N}\mathscr{F}_C\begin{bmatrix}1+\frac{\mathscr{F}_C}{\Phi_{PM}\mathscr{R}_{PM}}\\ 1+\frac{\mathscr{F}_C}{\Phi_{PM}\mathscr{R}_{PM}}\\ 1+\frac{\mathscr{F}_C}{\Phi_{PM}\mathscr{R}_{PM}}\\ 1+\frac{\mathscr{F}_C}{\Phi_{PM}\mathscr{R}_{PM}}\end{bmatrix}. \tag{3.30}$$

Note that the forces at all four 'C'-cores are identical in magnitude and sign; hence, no torquing moment is applied to the armature. Also, readers may be curious as to why driving the $\pm\hat{x}$ coils in the opposite direction from the $\pm\hat{y}$ coils produces forces in one direction only. The reason is best explained by examining Figure 3-8. Note how the permanent magnet flux and coil flux are in the same direction on the top $(+\hat{z})$ side of the ring at the $-\hat{y}$ 'C'-core. At the $+\hat{x}$ 'C'-core, however, the PM and coil flux have the same direction on the bottom $(-\hat{z})$ side of the armature. Thus, the $+\hat{x}$ (and equivalently $-\hat{x}$) flux must be reversed to generate more flux in the top gap and consequently impart an upward force.

The net force is thus:

$$F_{C,NET} = \sum \boldsymbol{F_C} = \frac{4}{A\mu_0 \mathscr{R}_N} \Phi_{PM} \frac{\mathscr{R}_{PM}}{\mathscr{R}_{PM} + 2\mathscr{R}_N} \mathscr{F}_C \left(\frac{\mathscr{F}_C}{\underbrace{\Phi_{PM} \mathscr{R}_{PM}}} + 1 \right). \tag{3.31}$$

The nonlinearity ($\mathscr{F}_C^2$) in the net force equation is undesirable as it can complicate the control design. Fortunately its effect is relatively minor. For the geometries considered in this thesis, the product of Φ_{PM} and $\mathscr{R}_{PM}$ is on the order of 10,000 amp-turns whereas the maximum value for $\mathscr{F}_C$ is <400 amp-turns. Thus, the underbraced term in equation (3.31) can be assumed to be zero and dropped from the expression to yield the approximation below[11]. At most, the linear approximation differs from the nonlinear equation by ≈4%.

$$F_{C,NET} \approx \frac{4}{A\mu_0 \mathscr{R}_N} \Phi_{PM} \frac{\mathscr{R}_{PM}}{\mathscr{R}_{PM} + 2\mathscr{R}_N} \mathscr{F}_C, \quad \Phi_{PM} \mathscr{R}_{PM} \gg \mathscr{F}_C \tag{3.32}$$

The coefficient preceding $\mathscr{F}_C$ in the above is collected into actuator mirror normal force constant K_C:

$$K_C \equiv \frac{4}{A\mu_0 \mathscr{R}_N} \underbrace{\Phi_{PM} \frac{\mathscr{R}_{PM}}{\mathscr{R}_{PM} + 2\mathscr{R}_N}}. \tag{3.33}$$

Observe that the underbraced portion of the force constant is the magnitude of the air gap flux contributed by the permanent magnet ($\Phi_{N,PM}$, eqn. (3.26b)). Increasing Φ_{PM} while holding the permanent magnet reluctance steady, by using a stronger magnet for example, increases the force exerted on the ring armature per unit of magnetomotive force.

Differentially Driven Coils / Torque Constants

Now assume, with the armature remaining centered, that the $\pm\hat{y}$ coils are driven with the same magnitudes ($\mathscr{F}_{DX}$) but in opposite directions from each other. In other words, the opposing coils are driven in "differential-mode"; hence, the subscript 'DX' indicates differential-mode about the $\hat{x}$-axis. Also, assume that the $\pm\hat{x}$ coils are

[11] Carrying-out the "proper" linearization of $F_{C,NET}$ about $\mathscr{F}_C = 0$ gives the same result.

turned off. The force vector expression for such a case is assigned the symbol $\boldsymbol{F_{DX}}$:

$$\boldsymbol{F_{DX}} \equiv \boldsymbol{F_N}\left(\mathscr{F}_{+\hat{y}} = \mathscr{F}_{DX},\ \mathscr{F}_{-\hat{y}} = -\mathscr{F}_{DX},\ \mathscr{F}_{+\hat{x}} = 0,\ \mathscr{F}_{-\hat{x}} = 0\right). \tag{3.34}$$

Carrying-out the substitutions reveals the following nonlinear expression:

$$\boldsymbol{F_{DX}} = \frac{1}{2A\mu_0}\Phi_{PM}\frac{\mathscr{R}_{PM}}{\mathscr{R}_{PM}+2\mathscr{R}_N}\frac{2}{\mathscr{R}_N}\mathscr{F}_{DX}\begin{bmatrix}\psi\mathscr{F}_{DX}-1\\ \psi\mathscr{F}_{DX}+1\\ 0\\ 0\end{bmatrix}, \tag{3.35a}$$

where ψ is:

$$\psi \equiv \frac{\mathscr{R}_{PM}+2\mathscr{R}_N}{2\Phi_{PM}\mathscr{R}_{PM}\left(\mathscr{R}_{PM}+\mathscr{R}_N\right)}. \tag{3.35b}$$

The forces at opposing 'C'-cores differ; consequently, a torque is applied to the ring armature. Using equation (3.22), the torque about the $\hat{x}$ axis is:

$$\begin{aligned} T_{DX} &= r\left(F_{DX,+\hat{y}} - F_{DX,-\hat{y}}\right) \\ &= \frac{r}{A\mu_0\mathscr{R}_N}\Phi_{PM}\frac{\mathscr{R}_{PM}}{\mathscr{R}_{PM}+2\mathscr{R}_N}\mathscr{F}_{DX}\left((\psi\mathscr{F}_{DX}+1)-(\psi\mathscr{F}_{DX}-1)\right) \\ &= \frac{2r}{A\mu_0\mathscr{R}_N}\Phi_{PM}\frac{\mathscr{R}_{PM}}{\mathscr{R}_{PM}+2\mathscr{R}_N}\mathscr{F}_{DX}. \end{aligned} \tag{3.36}$$

The nonlinear terms of $\boldsymbol{F_{DX}}$ conveniently cancel in the torque calculation, yielding a linear expression without the need for approximations. The coefficient in front of $\mathscr{F}_{DX}$ is collected into $\hat{x}$-axis torque constant K_{DX}:

$$K_{DX} \equiv \frac{2r}{A\mu_0\mathscr{R}_N}\Phi_{PM}\frac{\mathscr{R}_{PM}}{\mathscr{R}_{PM}+2\mathscr{R}_N}. \tag{3.37}$$

Similarly, a torque is applied about the $\hat{y}$ axis by oppositely driving the $\pm\hat{x}$ coils while the $\pm\hat{y}$ coils are turned off. The resulting force vector is:

$$\boldsymbol{F_{DY}} \equiv \boldsymbol{F_N}\left(\mathscr{F}_{+\hat{y}} = 0,\ \mathscr{F}_{-\hat{y}} = 0,\ \mathscr{F}_{+\hat{x}} = \mathscr{F}_{DY},\ \mathscr{F}_{-\hat{x}} = -\mathscr{F}_{DY}\right), \tag{3.38}$$

and the corresponding expressions for $\hat{y}$-axis torque and torque constant are:

$$T_{DY} = \frac{2r}{A\mu_0 \mathscr{R}_N} \Phi_{PM} \frac{\mathscr{R}_{PM}}{\mathscr{R}_{PM} + 2\mathscr{R}_N} \mathscr{F}_{DY} \tag{3.39}$$

$$K_{DY} \equiv \frac{2r}{A\mu_0 \mathscr{R}_N} \Phi_{PM} \frac{\mathscr{R}_{PM}}{\mathscr{R}_{PM} + 2\mathscr{R}_N}. \tag{3.40}$$

Since the $\hat{x}$-axis and $\hat{y}$-axis torque constants are identical, a single differential-mode torque constant K_D is defined for convenience. Note that K_D is differs from the $\hat{z}$-axis force constant K_C by a factor of $r/2$.

$$K_D \equiv K_{DY} = K_{DX} = \frac{r}{2} K_C \tag{3.41}$$

Normal Force in Response to Torquing MMF

Summing the force vector for the case where opposing coils are driven in opposite directions reveals an interesting effect:

$$\begin{aligned} F_{DX,NET} = \sum \boldsymbol{F_{DX}} &= \frac{1}{2A\mu_0} \Phi_{PM} \frac{\mathscr{R}_{PM}}{\mathscr{R}_{PM} + 2\mathscr{R}_N} \frac{2}{\mathscr{R}_N} \mathscr{F}_{DX} \big((\psi \mathscr{F}_{DX} + 1) + (\psi \mathscr{F}_{DX} - 1) \big) \\ &= \frac{2\psi}{A\mu_0 \mathscr{R}_N} \Phi_{PM} \frac{\mathscr{R}_{PM}}{\mathscr{R}_{PM} + 2\mathscr{R}_N} \mathscr{F}_{DX}^2 \\ &= \frac{1}{A\mu_0 \mathscr{R}_N \left(\mathscr{R}_{PM} + \mathscr{R}_N \right)} \mathscr{F}_{DX}^2. \end{aligned} \tag{3.42}$$

In addition to the previously described torque, the equation above shows that differentially driving opposing coils imparts a force upon the armature in the $+\hat{z}$ direction. This parasitic force is proportional to the square of the coil-induced magnetomotive force. This effect is undesirable for two reasons. First, it couples angular actuation to linear actuation. Ideally angular and linear actuation would be independent from each other for control purposes. Secondly, the effect is nonlinear and is therefore somewhat more difficult to compensate for.

However, the consequences of this nonlinear $+\hat{z}$ force coupling are not fatal to the ring core concept for several reasons. First, spring-like bearing forces (see Chapter

4) will oppose the spurious $+\hat{z}$ force and limit resulting displacement. Secondly, the effect can be minimized by maximizing the permanent magnet reluctance (the effect diminishes to zero when the PM reluctance is assumed to be infinite). Third, alternative electromagnetic configurations (see Section 3.4) can reduce or eliminate the effect. And finally, assuming sufficient control effort exists, the coils can be collectively driven per equation (3.29) to oppose the effect via closed loop control of the armature $\hat{z}$-axis displacement or by some open-loop / feedforward control scheme.

Let's examine the control-effort qualification on last mitigation strategy by summing the linear approximation for intentional $\hat{z}$-axis force (3.32) with the expression for parasitic force and letting the net force be zero:

$$\begin{gathered} F_{C,NET} + F_{DX,NET} = 0 \rightarrow F_{C,NET} = -F_{DX,NET}, \\ \frac{4}{A\mu_0 \mathscr{R}_N} \Phi_{PM} \frac{\mathscr{R}_{PM}}{\mathscr{R}_{PM} + 2\mathscr{R}_N} \mathscr{F}_C = -\frac{1}{A\mu_0 \mathscr{R}_N \left(\mathscr{R}_{PM} + \mathscr{R}_N\right)} \mathscr{F}_{DX}^2. \end{gathered} \tag{3.43}$$

Next, solving for the ratio of the common flux ($\mathscr{F}_N$) to the differential (torquing) flux ($\mathscr{F}_{DX}$) gives:

$$\frac{\mathscr{F}_N}{\mathscr{F}_{DX}} = \frac{\mathscr{R}_{PM} + 2\mathscr{R}_N}{\mathscr{R}_{PM} + \mathscr{R}_N} \frac{\mathscr{F}_{DX}}{4\Phi_{PM}\mathscr{R}_{PM}}. \tag{3.44}$$

$\mathscr{R}_{PM}$ is typically much larger than $\mathscr{R}_N$ and thus $\mathscr{R}_{PM} + 2\mathscr{R}_N \cong \mathscr{R}_{PM} + \mathscr{R}_N$:

$$\frac{\mathscr{F}_N}{\mathscr{F}_{DX}} \approx \frac{\mathscr{F}_{DX}}{4\Phi_{PM}\mathscr{R}_{PM}}. \tag{3.45}$$

As mentioned before, the product of Φ_{PM} and $\mathscr{R}_{PM}$ is much larger than the maximum values for coil MMF (for the geometries considered in this thesis). Thus, only a small fraction ($\approx$1%) of available common-mode MMF is needed to reject the parasitic force caused by even the largest magnitudes of differential MMF.

Note that the effect is also apparent when differentially driving the $\pm\hat{x}$ coils:

$$F_{DY,NET} = \sum \boldsymbol{F_{DY}} = \frac{1}{A\mu_0 \mathscr{R}_N \left(\mathscr{R}_{PM} + \mathscr{R}_N\right)} \mathscr{F}_{DY}^2. \tag{3.46}$$

The differentially-driven nonlinear force coefficient, equal for both $F_{DX,NET}$ and

$F_{DY,NET}$, is collected into variable C_D.

$$C_D \equiv \frac{1}{A\mu_0 \mathscr{R}_N (\mathscr{R}_{PM} + \mathscr{R}_N)}. \tag{3.47}$$

3.3.6 Linearly Displaced Armature

Now assume that, instead of being centered, the ring armature is displaced slightly along the $+\hat{z}$ vector (i.e. upward) with no rotation. If air gap reluctance is assumed to be linear with displacement[12], the reluctance at the top air gaps will decrease by an incremental reluctance $\mathscr{R}_L$ and the bottom air gaps' reluctance will increase by $\mathscr{R}_L$. Thus, $\mathscr{R}_L$ is proportional to armature $+\hat{z}$ translation. Furthermore, assume that the coils are turned off (zero MMF). The resulting air gap flux vector is assigned label $\mathbf{\Phi_L}$ and is mathematically defined in (3.48). The 'L' subscript specifies a linearly (in the geometric sense of the word) displaced armature.

$$\begin{aligned}\mathbf{\Phi_L} \equiv \mathbf{\Phi_{AG}}(&\mathscr{R}_{-\hat{y}T} = \mathscr{R}_N - \mathscr{R}_L,\ \mathscr{R}_{-\hat{x}T} = \mathscr{R}_N - \mathscr{R}_L,\ \mathscr{R}_{+\hat{y}T} = \mathscr{R}_N - \mathscr{R}_L,\ \mathscr{R}_{+\hat{x}T} = \mathscr{R}_N - \mathscr{R}_L,\\ &\mathscr{R}_{-\hat{y}B} = \mathscr{R}_N + \mathscr{R}_L,\ \mathscr{R}_{-\hat{x}B} = \mathscr{R}_N + \mathscr{R}_L,\ \mathscr{R}_{+\hat{y}B} = \mathscr{R}_N + \mathscr{R}_L,\ \mathscr{R}_{+\hat{x}B} = \mathscr{R}_N + \mathscr{R}_L,\\ &\mathscr{F}_{+\hat{y}} = 0,\ \mathscr{F}_{-\hat{y}} = 0,\ \mathscr{F}_{+\hat{x}} = 0,\ \mathscr{F}_{-\hat{x}} = 0)\end{aligned} \tag{3.48}$$

The expansion of $\mathbf{\Phi_L}$ is a complex, nonlinear (in $\mathscr{R}_L$) expression and thus provides little insight into how the air gap flux changes with armature displacement. However, linearization of $\mathbf{\Phi_L}$ about $\mathscr{R}_L = 0$ gives a fairly intuitive result:

$$\begin{aligned}\mathbf{\Phi_L} &\approx \Phi_{PM}\frac{\mathscr{R}_{PM}}{\mathscr{R}_{PM} + 2\mathscr{R}_N}\left(\begin{bmatrix}1 & 1 & 1 & 1 & -1 & -1 & -1 & -1\end{bmatrix}^T\right.\\ &\qquad\left. + \begin{bmatrix}\frac{\mathscr{R}_L}{\mathscr{R}_N} & -\frac{\mathscr{R}_L}{\mathscr{R}_N} & \frac{\mathscr{R}_L}{\mathscr{R}_N} & -\frac{\mathscr{R}_L}{\mathscr{R}_N} & -\frac{\mathscr{R}_L}{\mathscr{R}_N} & +\frac{\mathscr{R}_L}{\mathscr{R}_N} & -\frac{\mathscr{R}_L}{\mathscr{R}_N} & +\frac{\mathscr{R}_L}{\mathscr{R}_N}\end{bmatrix}^T\right)\\ &= \mathbf{\Phi_{N,PM}} + \Phi_{PM}\frac{\mathscr{R}_{PM}}{\mathscr{R}_{PM} + 2\mathscr{R}_N}\frac{\mathscr{R}_L}{\mathscr{R}_N}\begin{bmatrix}1 & -1 & 1 & -1 & -1 & 1 & -1 & 1\end{bmatrix}^T.\end{aligned} \tag{3.49}$$

That is, the change in air gap flux (relative to the centered armature) is equal to

[12] A reasonable assumption for small displacements only

the centered-armature flux multiplied by plus or minus the fraction of incremental reluctance to centered-armature reluctance. For instance, if the armature is displaced upward by a quarter of the gap length, then $\mathscr{R}_L = \mathscr{R}_N/4$ and (3.49) predicts that the top air gap flux will be $5/4$'ths of the centered-armature value and the bottom gap flux will be $3/4$'ths of the centered-armature flux.

The displaced-armature force vector expression, $\boldsymbol{F_L}$, is also nonlinear and not worth displaying here. The linearized force vector (about $\mathscr{R}_L = 0$) is shown in (3.50) below. Note that the error due to the linearization will be examined in subsequent chapters. In general the error is negligible for small displacements.

$$\boldsymbol{F_L} \approx \frac{2}{A\mu_0\mathscr{R}_N}\left(\Phi_{PM}\frac{\mathscr{R}_{PM}}{\mathscr{R}_{PM}+2\mathscr{R}_N}\right)^2 \mathscr{R}_L \begin{bmatrix}1 & 1 & 1 & 1\end{bmatrix}^T \tag{3.50}$$

The forces at each 'C'-core are equal in magnitude and direction and thus no moment is applied to the armature. The net force imparted upon the armature is:

$$F_{L,NET} = \sum \boldsymbol{F_L} \approx \frac{8}{A\mu_0\mathscr{R}_N}\left(\underbrace{\Phi_{PM}\frac{\mathscr{R}_{PM}}{\mathscr{R}_{PM}+2\mathscr{R}_N}}\right)^2 \mathscr{R}_L. \tag{3.51}$$

Note that the net displaced-armature force is non-restoring. Nudging the armature upward results in an upward pulling force which will further displace the armature unless it is balanced by some other force. Therefore, the concept's displaced-armature response is like (and often called) a negative spring. Thus, the coefficient of $\mathscr{R}_L$ in (3.51) is called the negative magnetic spring constant and is given the label K_L. Also, observe that the force depends on the square of the permanent magnet's contribution to air gap flux (underbraced term in (3.51)).

$$K_L \equiv \frac{8}{A\mu_0\mathscr{R}_N}\left(\Phi_{PM}\frac{\mathscr{R}_{PM}}{\mathscr{R}_{PM}+2\mathscr{R}_N}\right)^2 \tag{3.52}$$

3.3.7 Rotationally Displaced Armature

One final displacement / coil-flux case is considered. Assume that the ring armature is first linearly centered in the 'C'-core openings and is then rotated slightly about

the $\hat{x}$-axis. Consequently, the section of armature within the $+\hat{y}$ 'C'-core opening is linearly displaced towards the top 'C'-core face. Likewise, the armature translates towards the bottom face at the $-\hat{y}$ 'C'-core. Assume that the linear displacements at the 'C'-cores again change the air gap reluctances by $\mathscr{R}_{RX}$ and that the change in reluctance due to the change in gap length across the face of the ring core is negligible. Additionally assume that the $\pm\hat{x}$ air gap reluctances don't change from the centered-armature values and that the coil currents are zero. The resulting air gap flux vector is assigned label $\boldsymbol{\Phi_{RX}}$ ('RX' for rotational displacement about the $\hat{x}$-axis):

$$\begin{aligned}\boldsymbol{\Phi_{RX}} \equiv \boldsymbol{\Phi_{AG}}(&\mathscr{R}_{-\hat{y}T} = \mathscr{R}_N + \mathscr{R}_{RX},\ \mathscr{R}_{-\hat{x}T} = \mathscr{R}_N,\ \mathscr{R}_{+\hat{y}T} = \mathscr{R}_N - \mathscr{R}_{RX},\ \mathscr{R}_{+\hat{x}T} = \mathscr{R}_N,\\ &\mathscr{R}_{-\hat{y}B} = \mathscr{R}_N - \mathscr{R}_{RX},\ \mathscr{R}_{-\hat{x}B} = \mathscr{R}_N,\ \mathscr{R}_{+\hat{y}B} = \mathscr{R}_N + \mathscr{R}_{RX},\ \mathscr{R}_{+\hat{x}B} = \mathscr{R}_N,\cdot\\ &\mathscr{F}_{+\hat{y}} = 0,\ \mathscr{F}_{-\hat{y}} = 0,\ \mathscr{F}_{+\hat{x}} = 0,\ \mathscr{F}_{-\hat{x}} = 0)\end{aligned} \tag{3.53}$$

The nonlinear and linearized expressions for $\boldsymbol{\Phi_{RX}}$ are similar to those for $\boldsymbol{\Phi_L}$ and are not printed here. The rotationally displaced force vector $\boldsymbol{F_{RX}}$ is, like $\boldsymbol{F_L}$, nonlinear. Linearizing about $\mathscr{R}_{RX} = 0$ gives the approximation:

$$\boldsymbol{F_{RX}} \approx \frac{2}{A\mu_0\mathscr{R}_N}\left(\Phi_{PM}\frac{\mathscr{R}_{PM}}{\mathscr{R}_{PM}+2\mathscr{R}_N}\right)^2 \mathscr{R}_{RX}\begin{bmatrix}-1 & 1 & 0 & 0\end{bmatrix}^T. \tag{3.54}$$

A mental summation of (3.54) confirms the intuition that a pure armature rotation results in zero net force. The same result is found if the nonlinear expression for $\boldsymbol{F_{RX}}$ is summed.

The $\pm\hat{y}$ force elements differ in direction resulting in a torque applied to the armature about the $\hat{x}$-axis. The linearized ($\mathscr{R}_{RX} = 0$) torque is computed per (3.22) and is given in equation (3.55):

$$\begin{aligned}T_{RX} &= r\left(F_{RX,+\hat{y}} - F_{RX,-\hat{y}}\right)\\ &\approx \frac{4r}{A\mu_0\mathscr{R}_N}\left(\Phi_{PM}\frac{\mathscr{R}_{PM}}{\mathscr{R}_{PM}+2\mathscr{R}_N}\right)^2 \mathscr{R}_{RX}.\end{aligned} \tag{3.55}$$

The rotated-armature torque is also non-restoring as the rotation and torque are

in the same direction. Thus, the concept's rotational displacement behavior is like a negative torsion spring.

Similarly, if the armature is rotated about the $\hat{y}$-axis, a torque develops about the $\hat{y}$-axis. Skipping the intermediate steps, the rotated-armature $\hat{y}$-axis torque is shown to be equivalent to the corresponding $\hat{x}$-axis expression:

$$T_{RY} \approx \frac{4r}{A\mu_0 \mathscr{R}_N} \left(\Phi_{PM} \frac{\mathscr{R}_{PM}}{\mathscr{R}_{PM} + 2\mathscr{R}_N} \right)^2 \mathscr{R}_{RY}, \tag{3.56}$$

where $\mathscr{R}_{RY}$ is the change in air gap reluctances at the $\pm\hat{x}$ 'C'-cores due to rotation about the $\hat{y}$-axis.

The identical coefficients preceding the $\mathscr{R}_{RX}$ and $\mathscr{R}_{RY}$ terms in (3.55) and (3.56) are collected into a rotational negative magnetic spring constant K_R.

$$K_R \equiv \frac{4r}{A\mu_0 \mathscr{R}_N} \left(\Phi_{PM} \frac{\mathscr{R}_{PM}}{\mathscr{R}_{PM} + 2\mathscr{R}_N} \right)^2 \tag{3.57}$$

3.3.8 First-Order Behavior Summary

The electromechanical force and moments applied to the ring armature can be summarized as the superposition of the basis functions derived above. The basis functions are approximations based on numerous assumptions, linearizations, and idealities and are thus subject to errors - especially for large armature displacements. However, subsequent magnetic finite element analyzes will show that these simple functions are generally sufficient for a first pass at designing an actuator and can be made fairly accurate if leakage flux is taken into account.

Continuing to use the electromagnetic parameters (reluctance, flux, etc.), the net force in the $\hat{z}$-axes is:

$$\begin{aligned} F &= F_{C,NET} + F_{DX,NET} + F_{DY,NET} + F_{L,NET} \\ &= K_C \mathscr{F}_C + C_D \left(\mathscr{F}_{DX}^2 + \mathscr{F}_{DY}^2 \right) + K_L \mathscr{R}_L, \end{aligned} \tag{3.58}$$

and the torques about the $\hat{x}$ and $\hat{y}$ axes are:

$$\begin{aligned} T_X &= T_{DX} + T_{RX} \\ &= K_D \mathscr{F}_{DX} + K_R \mathscr{R}_{RX} \end{aligned} \tag{3.59}$$

$$\begin{aligned} T_Y &= T_{DY} + T_{RY} \\ &= K_D \mathscr{F}_{DY} + K_R \mathscr{R}_{RY}. \end{aligned} \tag{3.60}$$

The first-order coefficients (K_C,C_D,K_L,K_D,K_R) are derived by magnetic equivalent circuit analysis in the previous section and are repeated in Table 3.1 for convenience. "First-order" is not used in the strictest sense of the phrase as the parabolic term for differentially-driven linear force is modeled. Note that the ring armature concept does not nominally impart any forces in the $\hat{x}$ or $\hat{y}$ directions as long the projection of the 'C'-core openings' faces are contained withing the ring's top and bottom faces.

Table 3.1: Force and Moment First-Order Coefficients (Magnetic Parameters)

Coefficient	Multiplies	Value	
K_C	$\mathscr{F}_C$	$\frac{4}{A\mu_0 \mathscr{R}_N} \Phi_{PM} \frac{\mathscr{R}_{PM}}{\mathscr{R}_{PM}+2\mathscr{R}_N}$	
C_D	$\mathscr{F}_{DX}^2$ & $\mathscr{F}_{DY}^2$	$\frac{1}{A\mu_0 \mathscr{R}_N (\mathscr{R}_{PM}+\mathscr{R}_N)}$	
K_L	$\mathscr{R}_L$	$\frac{8}{A\mu_0 \mathscr{R}_N} \left(\Phi_{PM} \frac{\mathscr{R}_{PM}}{\mathscr{R}_{PM}+2\mathscr{R}_N} \right)^2$	
K_D	$\mathscr{F}_{DX}$ & $\mathscr{F}_{DY}$	$\frac{2r}{A\mu_0 \mathscr{R}_N} \Phi_{PM} \frac{\mathscr{R}_{PM}}{\mathscr{R}_{PM}+2\mathscr{R}_N}$	$= \frac{r}{2} K_C$
K_R	$\mathscr{R}_{RX}$ & $\mathscr{R}_{RY}$	$\frac{4r}{A\mu_0 \mathscr{R}_N} \left(\Phi_{PM} \frac{\mathscr{R}_{PM}}{\mathscr{R}_{PM}+2\mathscr{R}_N} \right)^2$	$= \frac{r}{2} K_L$

The electromagnetic parameters will now be converted to physical variables (e.g. length, area, current), which are more useful for design. First, let l_N be the centered-armature (nominal position) top and bottom air gap length while variable A continues to be the air gap effective area (approximately equal to the 'C'-core cross-sectional area). The nominal air gap reluctance $\mathscr{R}_N$ is thus:

$$\mathscr{R}_N \equiv \frac{l_N}{A\mu_0}. \tag{3.61}$$

If z is the pure translation of the ring armature along the $\hat{z}$-axis, then the change in air gap reluctance $\mathscr{R}_L$ is:

$$\mathscr{R}_L \equiv \frac{z}{A\mu_0}. \tag{3.62}$$

And, if $\theta_{FSM,X}$ and $\theta_{FSM,Y}$ are the armature rotations about the $\hat{x}$ and $\hat{y}$ axes respectively, then the approximate change in air gap reluctance due to the rotations are:

$$\mathscr{R}_{RX} \equiv \frac{r\theta_{FSM,X}}{A\mu_0}, \tag{3.63}$$

$$\mathscr{R}_{RY} \equiv \frac{r\theta_{FSM,Y}}{A\mu_0}, \tag{3.64}$$

where r remains the effective radius from the armature pivot to the 'C'-cores.

The flux generated by the permanent magnet, Φ_{PM}, is the product of its residual magnetization B_r (a material property) and the PM area perpendicular to the magnetization direction A_{PM}:

$$\Phi_{PM} \equiv B_r A_{PM}. \tag{3.65}$$

The permanent magnet reluctance, $\mathscr{R}_{PM}$, is approximated as:

$$\mathscr{R}_{PM} \equiv \frac{l_{PM}}{A_{PM}\mu_0}. \tag{3.66}$$

Here l_{PM} is the permanent magnet length (parallel to the magnetization direction). Magnetic FEA will show that this approximation for $\mathscr{R}_{PM}$ is particularly poor since the PM area is small compared to its length.

And lastly, the coil MMFs are defined as the products of coil currents and number of wire turns:

$$\mathscr{F}_C \equiv Ni_C, \tag{3.67}$$

$$\mathscr{F}_{DX} \equiv Ni_{DX}, \tag{3.68}$$

$$\mathscr{F}_{DY} \equiv Ni_{DY}, \tag{3.69}$$

where N is the number of turns of wire around each 'C'-core, i_C is the current common to all 'C'-cores, i_{DX} is the difference in current between the $\hat{y}$ 'C'-cores, and i_{DY} is the difference in current between the $\hat{x}$ 'C'-cores.

Rewritten as functions of design parameters, the ring armature concept forces and moments are:

$$F = k_C i_C + c_D \left(i_{DX}^2 + i_{DY}^2\right) + k_L z, \tag{3.70}$$

$$T_X = k_D i_{DX} + k_R \theta_{FSM,X}, \tag{3.71}$$

$$T_Y = k_D i_{DY} + k_R \theta_{FSM,Y}. \tag{3.72}$$

The lower-cased coefficients (k_C,c_D,k_L,k_D,k_R) are given in Table 3.2. If the lengths of the permanent magnets are much greater than twice the air gap length and the PM area is smaller or roughly equal to the air gap area, then $l_{PM}A/(l_{PM}A+2l_N A_{PM})$ is about 1 and the coefficients further simply to the approximations given in the rightmost column of Table 3.2.

Table 3.2: Force and Moment First-Order Coefficients (Design Parameters)

Coefficient	Multiplies	Value	Approximation
k_C	i_C	$\frac{4N}{l_N} B_r A_{PM} \frac{l_{PM}A}{l_{PM}A+2l_N A_{PM}}$	$\frac{4N}{l_N} B_r A_{PM}$
c_D	i_{DX}^2 & i_{DY}^2	$\frac{N^2 A_{PM} A \mu_0}{l_N (l_{PM}A+l_N A_{PM})}$	$\frac{N^2 A_{PM} \mu_0}{l_N l_{PM}}$
k_L	z	$\frac{8}{A\mu_0 l_N} \left(B_r A_{PM} \frac{l_{PM}A}{l_{PM}A+2l_N A_{PM}}\right)^2$	$\frac{8}{A\mu_0 l_N} B_r^2 A_{PM}^2$
k_D	i_{DX} & i_{DY}	$\frac{2rN}{l_N} B_r A_{PM} \frac{l_{PM}A}{l_{PM}A+2l_N A_{PM}}$	$\frac{2rN}{l_N} B_r A_{PM}$
k_R	$\theta_{FSM,X}$ & $\theta_{FSM,Y}$	$\frac{4r^2}{A\mu_0 l_N} \left(B_r A_{PM} \frac{l_{PM}A}{l_{PM}A+2l_N A_{PM}}\right)^2$	$\frac{4r^2}{A\mu_0 l_N} B_r^2 A_{PM}^2$

3.4 Alternative Ring Core Topologies

With the basic operating principals of the ring armature concept understood, a number of variations to the electromagnetic topology can be imagined. Two such variations are presented here. Others are shown in Appendix C with limited discussion.

3.4.1 Two-Level Permanent Magnet Ring

Placement of the permanent magnets at the bottoms of the 'C'-cores (as in Figure 3-4) is arbitrary with respect the electromechanical behavior. That is, the equations for the forces and moments developed above are identical[13] if the magnets instead span the 'C'-cores' top segments. However, the equations change slightly if the permanent magnet locations alternate between the tops and bottoms of the 'C'-cores as shown in Figure 3-12. I'll refer to this arrangement as a "two-level PM" variation of the ring armature concept. The corresponding magnetic equivalent circuit is shown in Figure 3-13.

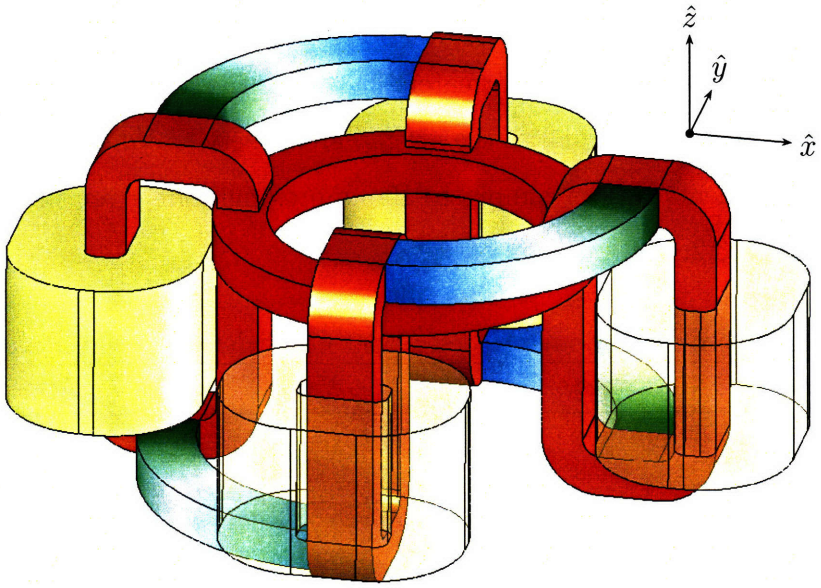

Figure 3-12: "Two-Level PM" Variation of the Ring Armature Concept

The variation's magnetic circuit is analyzed similarly to original concept (i.e. using symbolic modified nodal analysis) with the assumption that the permanent magnets' properties (Φ_{PM}, $\mathscr{R}_{PM}$) are the same for the top PMs as they are for the bottom PMs. The resulting expressions for force and torque as a function of armature $\hat{z}$ translation and $\hat{x}$,$\hat{y}$ rotations are identical to the originals. The resulting equation for force as a function of coil common-mode magnetomotive force (i.e. F_C) is equal to the linearized version in the original topology (eqn. (3.32)). In other words, the small common-mode

[13] Actually, nearly identical. The nonlinear terms' signs reverse.

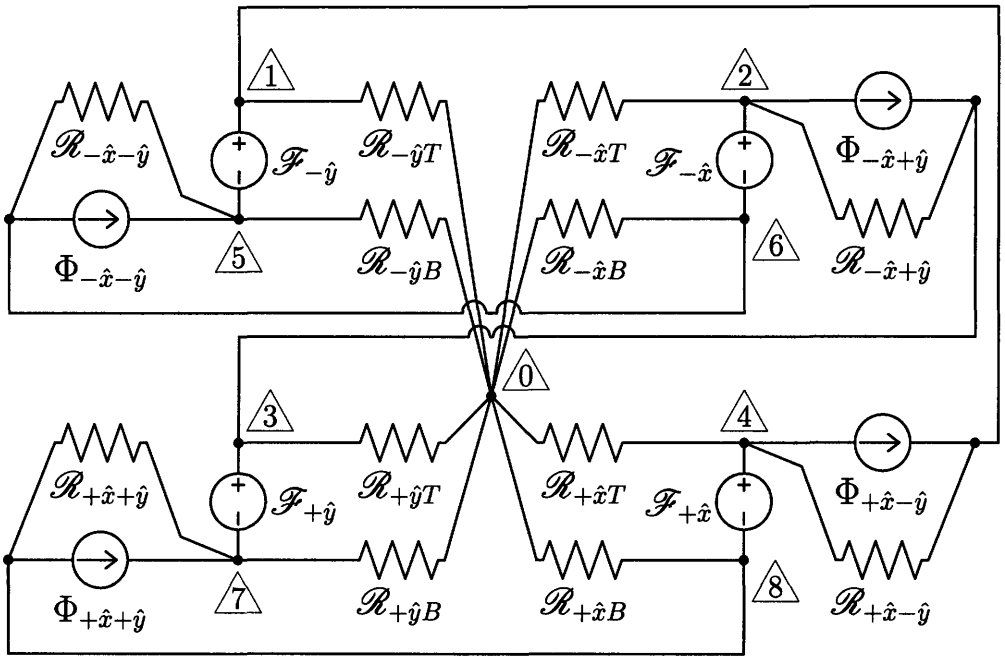

Figure 3-13: "Two-Level PM" Variation Magnetic Equivalent Circuit

nonlinearity disappears entirely in the two-level PM variation. More significantly, however, the nonlinear coupling to a translational force when differentially driving the coils ($F_{DX,NET}$,$F_{DY,NET}$) is also eliminated.

Therefore, the advantage of the two-level PM variation of the ring armature concept is that it makes the control design much simpler as the nonlinearity and off-axis coupling are eliminated. One potential disadvantage, however, is that the top-level permanent magnets may limit the FSM field of view.

In reality[14], the assumption that the PM properties are the same for the top and bottom "levels" of magnets isn't accurate since the geometry is not symmetric about the $\hat{x}-\hat{y}$ plane. Because of their proximity to the ring core, for example, the top permanent magnets will likely "leak" more flux than the bottom PMs, hence lowering their effective reluctance. To see the resulting effect on the nonlinear coupling coefficient, let $\mathscr{R}_{PM-T}$ and $\mathscr{R}_{PM-B}$ be the top and bottom permanent magnet equivalent reluctances (with leakage taken into account). The nonlinear coupling coefficient

[14]Where "reality" is no longer ignoring leakage flux

(akin to C_D for the original topology) is thus:

$$C_D^{'} = \frac{1}{2} \frac{\mathscr{R}_{PM-T} - \mathscr{R}_{PM-B}}{A\mu_0 \mathscr{R}_N \left(\mathscr{R}_{PM-T} + \mathscr{R}_N\right)\left(\mathscr{R}_{PM-B} + \mathscr{R}_N\right)}. \tag{3.73}$$

Comparing (3.73) with (3.47) revels that even if the reluctances are not precisely matched, the "two-level PM" variation reduces the magnitude of the nonlinear force coupling.

3.4.2 Sparse Permanent Magnets

The $+\hat{x}-\hat{y}$ and $-\hat{x}+\hat{y}$ permanent magnets have been deleted in the "sparse PM" concept shown in Figure 3-14. The bias flux supplied by the remaining magnets performs the same linearization function as the four magnets in the original topology. However, the nominal path of the bias flux differs somewhat. After jumping the air gaps from a "north" 'C'-core (e.g. $-\hat{y}$) into the ring core, the flux flows only towards the "south" 'C'-core to which the PM spans (e.g. $-\hat{x}$). Recall per Figure 3-6 that the bias flux branches towards both "south" 'C'-cores in the original (and "two level PM") topology. Thus, two segments of the ring core ($+\hat{x}-\hat{y}$ and $-\hat{x}+\hat{y}$) do no carry any flux in this configuration and could be deleted to reduce armature inertia (as in Figure C-1).

The sparse PM variation is analyzed using the original magnetic equivalent circuit (Figure 3-9) by setting the missing magnets' flux drives (Φ_{+x-y}, Φ_{-x+y}) to zero. The magnet reluctances ($\mathscr{R}_{+x-y}$, $\mathscr{R}_{-x+y}$) are retained; however, because the air that replaces the PMs will have an equivalent reluctance. Instead of symbolically resolving the resulting MNA matrices, a shortcut is employed by recognizing that the permanent magnet flux contribution is half of its former value (i.e. $\Phi_{PM}^{'} = \Phi_{PM}/2$). The half PM flux term is plugged directly into the force and moment coefficient expressions (Table 3.1). We find that the force and torques due to coil MMF are half of their original values (per MMF). The force and torques due to displacements (translational and rotational respectively) are a quarter of their original values (per displacement unit). Interestingly, the nonlinear coupling coefficient (C_D) does not

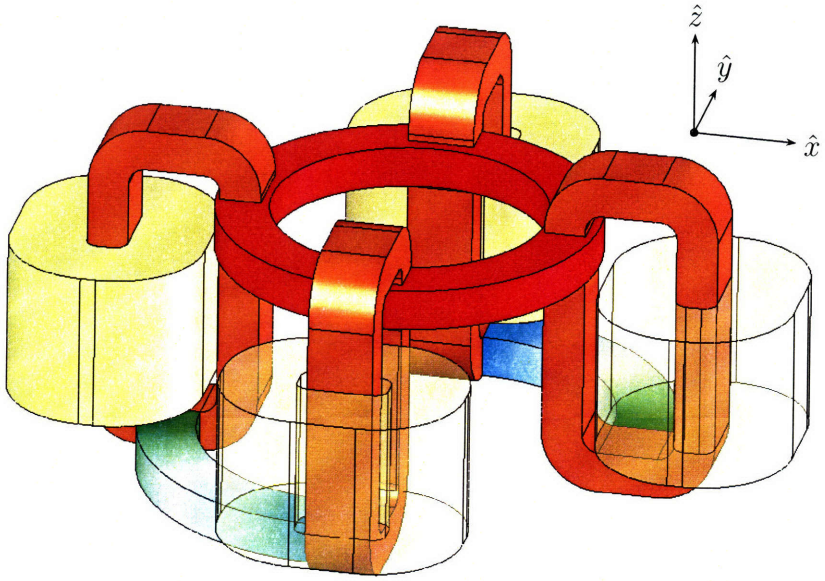

Figure 3-14: "Sparse PM" Variation of the Ring Armature Concept

change from its value for the original topology and hence grows as a fraction of the common-mode flux force constant (K_C).

The sparse PM topology offers two advantages when compared with the original. First, the volume previously occupied by the deleted PMs could be used for other FSM components (e.g. to route sensor wires), reducing the overall FSM size. Secondly, for low bias designs, the PM frontal area (i.e. perpendicular to the magnetization direction) in four-magnet configurations could be too small to manufacture. By deleting half of the magnets, the remaining PMs' frontal areas must double to maintain the same bias level. Thus, the sparse PM variation's magnets could be large enough to manufacture.

THIS PAGE INTENTIONALLY LEFT BLANK

Chapter 4

Mechanical Concept

4.1 Actuator Torque and Bearing Stiffness

Determining actuator torque requirements is crucial to minimizing the size of the fast steering mirror. Overdesigning the actuator wastes valuable volume and mass; yet an underdesigned actuator will fail to meet the performance requirements. Figure 4-1 presents a simple dynamic model of a 2D fast steering mirror with a single angular degree of freedom. The mirror and supporting structure, collectively referred to as the armature, is connected to a mechanical ground through a spring and damper with coefficients K and D respectively. Actuator forces applied at a distance r from the effective pivot impart a torque T on the armature. The mirror dynamics can be described with the following second-order equation:

$$J\ddot{\theta}_{FSM} = T - D\dot{\theta}_{FSM} - K\theta_{FSM}, \tag{4.1}$$

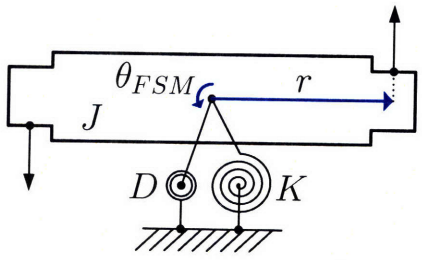

Figure 4-1: Simple Second-Order FSM Model

where J is the mirror body's rotational inertia. Solving (4.1) for torque gives:

$$T = J\ddot{\theta}_{FSM} + D\dot{\theta}_{FSM} + K\theta_{FSM}. \tag{4.2}$$

Equation (4.2) can be used to calculate the torque required to accelerate the mirror with the disturbance rejection profile determined in Section 2.4 if constants J, K, and D are known.

Reasonably accurate estimates for rotational inertia J are easily calculated with a solid modeling program. Preliminary armature designs have rotational inertias between 1×10^{-6} and 1.6×10^{-6} kg·m^2. To be conservative, $J = 2\times10^{-6}$ kg·m^2 is assumed. Spring constant K is a design parameter and is varied by adjusting the size of the bearing (see Section 4.2.2). Damping constant D is a weakly controlled design parameter is that principally affected by the choice of bearing materials, and by the frequency-dependent damping of the elastomeric bearing material.

Selecting an optimal range[1] of values for K is a very important design decision. If K is high, meaning the bearing is stiff, then a large torque will be required to point the mirror at the edges of the required range. However, decreasing K in the actuated direction tends to reduce stiffness in the constrained degrees of freedom. Also, small K values allow spurious toques to easily displace the armature. Thus, the powered-off armature position might not settle in the nominal center. If K is negative[2], then the problem is exacerbated as any disturbance from center will cause the armature to accelerate towards the 'C'-core cut faces (possible causing damage to the cores). Thus, the plant stiffness, i.e. K, should be set as high as possible without reducing performance due to the actuator's torque limitations.

Figure 4-2 is a plot of the torque required to move the mirror at several acceleration scenarios as a function of armature spring constant. The black and blue "disturbance rejection" curves give the 3×RMS torque value when the armature is accelerated with random noise with a power spectrum given in Figure 2-13. The disturbance rejection

[1] Predicting an exact value for the spring constant is difficult in practice. To be conservative, this thesis designates an acceptable range of values and verifies performance at the endpoints.

[2] A negative magnetic spring rate is possible because the magnetics act to pull the armature towards the 'C'-core faces; see Section 3.3.6.

profiles are simulated with a pointing offset of zero degrees (i.e. centered) and at the far extent of the FSM's required range (i.e. 10 mrad). The red and green "scanning" curves depict the peak torque required to perfectly track a sinusoidal displacement command at 160 Hz and 1 kHz respectively. The scanning amplitudes are set to give a peak acceleration of $10\,^{\mathrm{krad}}/_{\mathrm{s}^2}$ (approximately full range at 160 Hz, ≈2% of full range at 1 kHz). The solid traces are simulated with a critical damping ratio (i.e. $\zeta = 1$) while the dashed lines represent underdamped systems ($\zeta = 0.3$). A thin, positively-slopped purple line illustrates the torque required to statically point to the edge of the sAFSM range.

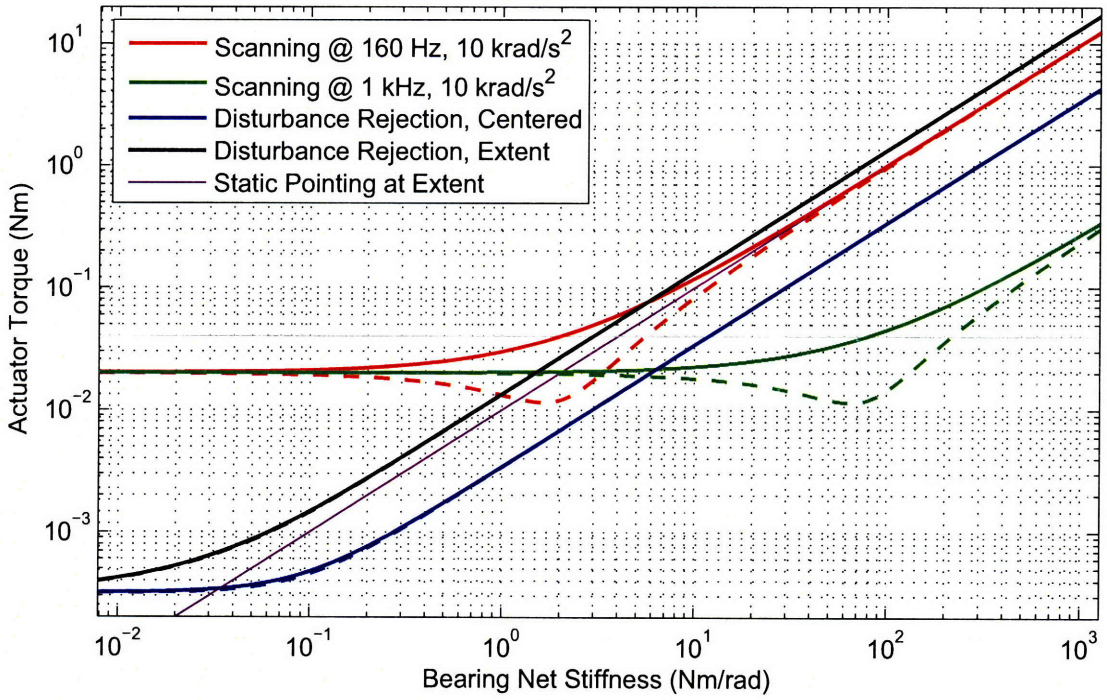

Figure 4-2: Required Actuator Torque vs. Plant Stiffness

Examining the torque versus stiffness plot leads to specifications for both the actuator's torque requirement and for the bearing stiffness. The plot shows that the actuator torque is dominated by armature inertial acceleration when the bearings are relatively compliant. Thus, a lower bound for the required torque is equal to the product of anticipated armature inertia and the maximum specified angular acceleration. As the bearings increasingly stiffen beyond $\approx 1\,^{\mathrm{N\cdot m}}/_{\mathrm{rad}}$, the torque requirement rises.

In general, greater actuator torque necessitates physically larger actuators. Consequently, a tradeoff exists between ease of control due to stiffer bearings and overall FSM size. Because of the emphasis on minimizing FSM size, I've chosen to favor a fairly compliant, moderate torque system. The sAFSM actuator minimum torque requirement is specified at 0.04 N·m, roughly twice the inertial acceleration load, and is indicated with a thin, horizontal, gray line in Figure 4-2. The corresponding value for maximum stiffness is therefore $\approx 3\,^{\text{N·m}}/_{\text{rad}}$.

Finally, note that the larger stiffness values in Figure 4-2 are ridiculous for the fast steering mirror application. For example, the maximum stiffness of $10^3\,^{\text{N·m}}/_{\text{rad}}$ is equivalent to torsion of a 12.5 mm diameter, 50 mm long aluminum rod. The smaller stiffness values are, however, realizable because magnetic actuator's negative spring could cancel the part or all of the bearing's mechanical stiffness.

Table 4.1: Actuator Torque and Net Angular Stiffness Specifications

Actuator Torque	>0.04 N·m
Net Angular Stiffness	$1\,^{\text{N·m}}/_{\text{rad}}$ to $3\,^{\text{N·m}}/_{\text{rad}}$
Rotational Natural Frequency	110 Hz to 200 Hz

4.2 Bearing Design

As discussed in the previous section, a primary role of the bearings is to oppose, within a specified stiffness range, displacements along the articulated degrees of freedom (tip and tilt). More importantly, the bearings must oppose armature displacements in the four other rigid body degrees of freedom (translation in $\hat{x}$, $\hat{y}$, and $\hat{z}$, plus rotation about $\hat{z}$). Spurious forces from a variety of source will act upon the armature from any potential angle. For example, if the actuator is meant for a space application, launch forces will accelerate the armature at multiples of the Earth's gravity. Ideally the bearing resistance to such unintentional forces would be infinite so that the armature's resulting displacement with respect to the FSM body is zero. In reality, designing a support that is relatively compliant in actuated degrees of freedom but very stiff in the constrained degrees of freedom is quite difficult.

4.2.1 AFSM Bearing Concept

Dan Kluk's Advanced Fast Steering Mirror bearing design employs multiple components to provide the bearing function. A two-dimensional version of the bearing concept is sketched in Figure 4-3. A metal cylindrical flexure resists armature $\hat{z}$-axis translation through axial strain. Since the flexure is long relative to its diameter, its bending mode stiffness only minimally resists armature rotations and transverse displacements. A set of rubber pads (two in the 2D drawing, four in the actual 3D implementation) oppose armature translations along the $\hat{x}$ and $\hat{y}$ axes as the compression modulus of constrained, thin rubber sheets is surprisingly large. The high elastic modulus is a result of the sheet's uniaxial strain condition[3] and rubber's nearly incompressible nature (i.e. a nearly 0.5 Poisson ratio). The rubber sheets are, however, relatively compliant in shear relative to their normal modulus. Therefore, the mechanical impedance to small armature rotations, which impart a shear stress upon the rubber pads, is, as desired, relatively low.

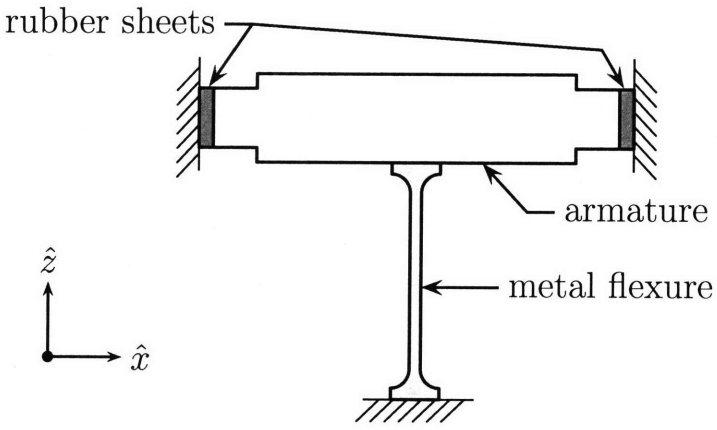

Figure 4-3: AFSM Bearing Concept

Kluk showed[22] that his bearing solution worked well with the exception that the net tip and tilt stiffness was about 25 times the expected value. Kluk's subsequent investigation identified that magnetically-generated compressive forces acting on the rubber bearings increased their effective modulus significantly, leading to the higher

[3]Uniaxial strain applies because the sheet's geometry (small thickness relative to width and height dimensions) and constraints (normal surfaces affixed to relatively stiff structures) prevent rubber material near the center of the pad from displacing transversely in response to normal stress.

resistance to actuator displacements. Unfortunately, the AFSM bearing concept, specifically the axial flexure's length, does not scale down to the sAFSM size. At 45.5 mm, the overall length of Kluk's flexure, including mounting features and gentle fillets, is even longer than the sAFSM's 36 mm overall thickness goal. The actual bending section of the AFSM flexure is 25 mm. Integrating the axial flexure in the sAFSM design would require reducing the flexure's overall length to ≈22 mm and the bending section to ≈13 mm - about half of the Kluk flexure length.

Kluk's thesis and just about any mechanics or machine design textbook, Section 4.4 of [15] for example, give the maximum bending stress of the cylindrical flexure as:

$$\sigma_{max} = \frac{K_t \theta E d}{2L}. \tag{4.3}$$

Where K_t is a stress concentration factor, E is the flexure material's elastic modulus, d is the cylindrical diameter, L is the flexure length, and θ is the rotation angle of the armature. Let's assume that Kluk's material selection and maximum design stress are optimal; that is, they can not be reasonably improved. Hence, K_t and E have the same values as in Kluk's analysis. Also, the AFSM actuator range is equal to the sAFSM range objective - meaning θ's value is similarly retained. Therefore, reducing the flexure length by $1/2$ requires a diameter reduction by an equal factor to maintain an equivalent stress level. However, halving the diameter is problematic because at 1.5 mm [60 mils], Kluk's flexure is already at the small end of conventional machining capability. A smaller flexure might be prohibitively difficult to machine and, if successfully fabricated, could be easily damaged during handling and installation.

Additionally, reducing the diameter lowers the axial stiffness and critical buckling load. The axial stiffness is given by:

$$k_{ax} = \frac{AE}{L} = \frac{\pi d^2 E}{4L}. \tag{4.4}$$

Substituting in a half-diameter, half-length flexure results in half of the axial stiffness due to the diameter-squared term. Assuming the elastomer pads do not contribute to the $\hat{z}$-axis stiffness, deflection due to spurious $\hat{z}$ forces are thus twice as large and

the armature's axial mode frequency decreases by 29%. Similarly, the buckling load is reduced by a factor of four, although it is not a concern as the expected loads are far below the critical level.

4.2.2 sAFSM Bearing Concept

Instead of relying upon the axial flexure to provide high stiffness in the mirror normal direction, the small advanced fast steering mirror will actively control the $\hat{z}$-axis degree of freedom with the same sensors and actuators that control mirror tip and tilt. Thus, the sAFSM design trades increased controller complexity and risk for reduced system size. The $\hat{z}$-axis displacement is controllable by driving the coils with a common current (see Section 3.3.5) and is observable by averaging the outputs of local position sensors (see Section 5.2). The performance of the active $\hat{z}$ position controller, that is, the equivalent stiffness, is largely variable by adjusting controller gain and is limited by the maximum bandwidth of the actuator/local sensor system and by sensor resolution and drift.

Additionally, the sAFSM bearing concept retains the rubber bearings from the AFSM design to provide armature rotational and radial stiffness. The rubber bearings also supply limited axial stiffness that will augment the active control when the FSM is powered and supplement it when the FSM is off. The elastomeric bearing analysis presented in this section is very similar to Kluk's, which, in turn, is based on earlier work by Lu[26], Cuff[10], and Barton[27] and Lindley's 1970 rubber technical manual[24].

Before analyzing the mechanical impedance of the sAFSM bearing system, let's first investigate the stiffness of a single elastomer sheet. Assume a rubber sheet has dimensions $w \times h \times t$. By the very definition of "sheet", the thickness, t, is significantly smaller than either the width, w, or height, h. The product of width and height is, of course, an area, which is commonly referred to as either the "loaded area"[4] or "bearing area" and is assigned the variable A_b. The small sides of the sheet are called the "force free areas". Imagine that one of the loaded areas is affixed to an

[4]Lindley's[24] nomenclature.

ideal mechanical ground and the opposite face is cemented to a stiff, hypothetical test block. The purpose of the test block in this thought exercise is to uniformly apply loads to the elastomer pad across the entire bearing area.

Applying a force parallel to the sheet's thickness dimension imparts a normal stress upon the elastomer sheet. The rubber responds as any linear-elastic solid would and resists the force with a stiffness given in equation (4.5) as:

$$k_n = \frac{F_n}{x_n} = \frac{A_b E_c}{t}. \tag{4.5}$$

Here E_c is an effective elastic modulus that accounts for partial[5] uniaxial strain and depends upon the elastomer's properties and the proportions of the sheet's shape. E_c is additionally discussed in a paragraph below. If the test block is pushed in any direction perpendicular to the thickness direction, then the rubber pad will be loaded in shear. The rubber pad's resulting shear stiffness for small to moderate strains is:

$$k_s = \frac{F_s}{x_s} = \frac{A_b G}{t}, \tag{4.6}$$

where G is the rubber's shear modulus. Lastly, torques applied to the test block along the thickness vector are opposed by the sheet's torsional stiffness, given by:

$$k_t = \frac{T_t}{\theta_t} = \frac{JG}{t}, \tag{4.7}$$

where J is polar moment of inertia about the torsion axis. For a rectangular sheet, the polar moment about the centroid axis is:

$$J = \frac{wh}{12}\left(w^2 + h^2\right). \tag{4.8}$$

Now consider a system of four such elastomer pads with identical dimensions affixed to four sides of a cuboid test block with dimensions $L \times L \times h$. The rubber sheets are centered on each respective block face and are oriented such that their

[5]Since the material near the force-free areas is able to displace laterally (i.e. bulge), true uniaxial strain exists only when the sheet's width and height are infinite.

height dimensions are all parallel to the block's height dimension. Block length L is larger than the pad width w (otherwise the pads wouldn't fit). As before, the rubber surfaces opposite from those attached to the block are constrained to a mechanical ground.

If a torque is applied to the test block along an axis that pierces the centroids of two of the rubber sheet's loaded areas, then two of the pads will be loaded in torsion (those in line with the torque) while the other two pads are predominately loaded in shear[6]. Computing the net resistance to the torque requires converting the linear shear stiffness, k_s, into an equivalent rotational stiffness. Let's assume that the torque rotates the test block by a small angle θ. At the shear loaded elastomer sheet, the rotation is approximately equivalent to a shear displacement of $\theta \cdot {}^{L}/_{2}$. Similarly, the shear force at the pad is equal to a moment along the torque axis divided by ${}^{L}/_{2}$. For convenience, ${}^{L}/_{2}$ is redefined as a bearing radius and is denoted r_b. The equivalent rotational stiffness due to a single shear-loaded pad is thus:

$$k_{eq} = \frac{M}{\theta} = \frac{F_s}{x_s} r_b^2 = k_s r_b^2, \tag{4.9}$$

and the total rotational stiffness from all four rubber pads is:

$$k_{rot} = 2k_{eq} + 2k_t = 2k_s r_b^2 + 2k_t. \tag{4.10}$$

If a force is applied to the test block parallel to its height dimension, then all four rubber sheets are loaded in shear and the net axial stiffness is:

$$.k_{ax} = 4k_s \tag{4.11}$$

Lastly, if a force is applied to the block parallel to either length dimension, then two of the pads will be loaded in their compression/tension mode and the other two pads

[6]The pads at the block faces perpendicular to the torque axis are also loaded in their normal directions as the top and bottom of the rotation block will tend to push into or away from the pad.

will be loaded in shear. Thus, the total mechanical impedance to radial force is:

$$k_{rad} = 2k_n + 2k_s. \tag{4.12}$$

Returning to a discussion of effective elastic modulus E_c, Lindley[24] created a set of relationships (and a convenient chart) that transform rubber shear modulus into an effective compression modulus as a nonlinear function of a "shape factor". Shape factor is defined as the ratio of the elastomer bearing's loaded area to its force-free area. For a rectangular pad, the shape factor is thus:

$$S = \frac{wh}{2t\,(w+h)}. \tag{4.13}$$

The effective modulus increases with growing shape factors because the material response is increasingly dominated by uniaxial strain. For shape factors greater-than 40, the elastic modulus can approach 1000 times the shear modulus (versus a maximum of 3× for conventional strain). David Cuff's 2006 Master's thesis[10] additionally discusses rubber bearings for precision actuator applications and is a useful resource.

Figure 4-4 illustrates the ranges of possible rotational stiffness values (k_{rot}) for reasonable sizes of elastomer pads. The x-axis discrete values represent readily available combinations of material thickness and durometer (hardness). Bearing radius r_b is set to 16.7 mm as determined by the optimization of the armature's non-stiff natural modes (see Section 5.5.1). The rubber sheets vary in width and height from 4×4 mm to 9.6×6.7 mm; shape factors range from a minimum of 0.16 to a maximum of 5.

The precise specification of the rubber bearing size is reserved for a subsequent chapter. Instead, Figure 4-4 is presented to convey the idea that a wide range of stiffness values are achievable by changing bearing dimensions and durometer. A continuous range of available stiffness values is especially reassuring given Kluk's difficulty achieving the targeted bearing stiffness. If a particular bearing implementation is found to be unsatisfactory in practice, perhaps because the bearing modulus is ele-

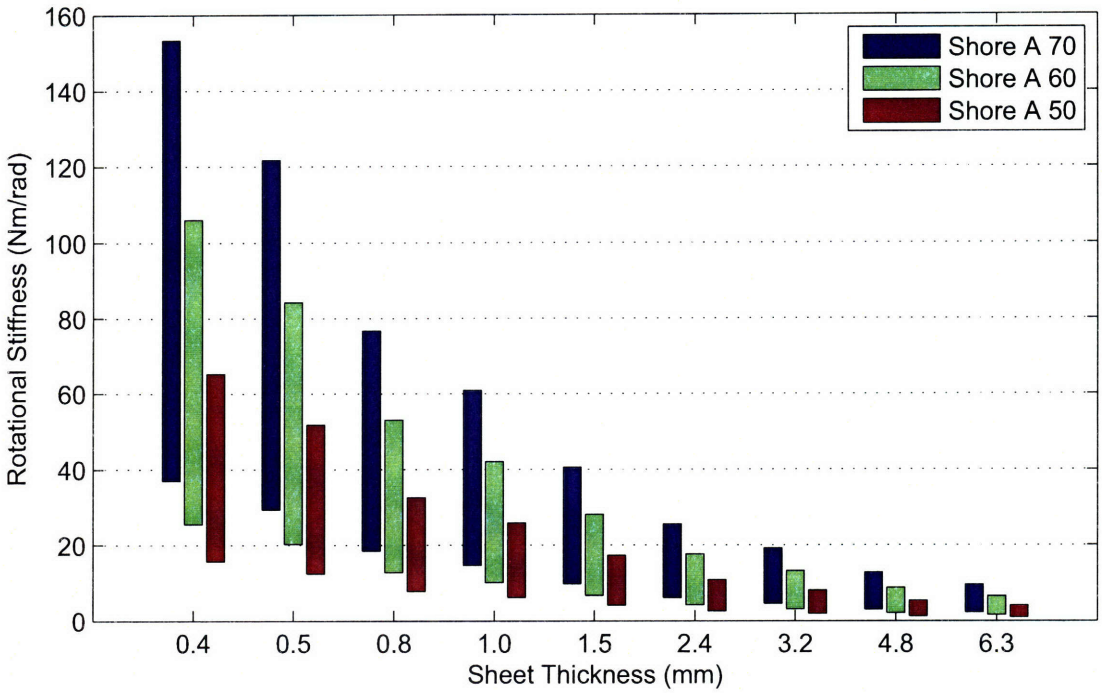

Figure 4-4: Elastomer Bearing Rotational Stiffness Range

vated due to an unexpected normal stress or perhaps because the negative magnetic spring rate is lower than intended, then it should be relatively easy to fabricate a new elastomer bearing with improved properties. Therefore, it is important to design the sAFSM such that the bearings can be swapped with relative ease.

Bearing Placement

In Kluk's (and Lu's) geometry, the bearings are located between the permanent magnets and moving armature cores. Consequently, they are "buried deep" within the assembly and are difficult to replace and nearly impossible to substitute with a bearing of different thickness. A second problem with the Lu/Kluk bearing placement is that it couples the bearing parameters with the magnetic design since the bearing thickness is an air gap in the magnetic path. Increasing the bearing thickness to satisfy a rotational stiffness requirement, for example, would decrease the effectiveness of the permanent magnet. Space permitting, a better location is outside of the magnetic path and away-from the actuators - a suggestion first posed by Jamie

Burnside, a Lincoln staff member and my Lincoln thesis supervisor. In the sAFSM design, the four elastomer sheets are located along the ring core's outside diameter at 45° angles from the actuator positions. Thus, they do not interfere with the magnetic design. Additionally, multiple variations of the parts that hold the rubber sheets to the armature are fabricated to allow easy substitutions between elastomer bearings with different thicknesses.

4.3 Summary

This chapter presented the concept for the sAFSM hybrid elastomer pad and active linear position control bearing system. Assuming a generic second-order mass/spring/-damper model of the moving armature, we discussed the tradeoffs between the reduced torque requirements of a compliant bearing versus greater constrained axis stiffness of a stiff support. Specifications for minimum actuator torque and armature net angular stiffness are derived from a plot of required actuator torque as a function of bearing stiffness. Dan Kluk's AFSM elastomer pad and axial flexure bearing concept was reviewed for applicability to the sAFSM design. However, the axial flexure's length does not scale down to the sAFSM size without compromising stiffness performance. Lastly, design equations for a set of four rubber bearings are presented along with a bar graph showing the range of possible rotational stiffness values as functions of discrete pad thickness.

Chapter 5

Design

5.1 Ring Armature Radius

Choosing the ring armature radius is one of the most important decisions in the actuator design. The armature radius influences the dimensions of almost every actuator part and it is a key factor in the actuator's performance. Generally, the smallest possible radius is advantageous for several reasons. First, the moment of inertia of ring and disc-like shapes increases with the square of the radius whereas the electromagnetic torque applied to the ring only increases linearly with radius. Thus, angular acceleration is maximized for smaller ring radii. Secondly, increasing the radius for a given angular range forces larger air gaps to prevent physical interference between the armature and the 'C'-cores. Lengthy air gaps reduce the torque coefficient (see k_D in Table 3.2), further diminishing acceleration capability. Lastly, decreasing the armature radius typically deceases the overall actuator size.

For the sAFSM design, I found that the minimum ring armature radius is limited by the mirror size and field of view requirements. It is possible to design actuator geometries where the ring armature is smaller than the mirror. However, such designs require elevating the mirror surface above the actuator's 'C'-cores. The increased armature thickness partially or completely offsets the inertia benefit from a smaller radius and introduces new challenges for armature balance and stiffness. The sAFSM ring armature's inside radius is set at 10.7 mm [0.421 in], a little more than one and

a third times the mirror radius. The increase in ring armature radius with respect to the mirror radius behaves more like an offset than a gain. For example, a sAFSM with a 30 mm mirror diameter could be designed with an armature that is only 20% larger than the mirror.

5.2 Local Sensor Selection and Placement

The actuators' integrated sensors provide signals proportional to armature (and hence mirror) displacement with respect to the FSM body. These position signals are transformed into tip and tilt angles and are used for feedback control. Non-contact displacement sensors are principally considered because they minimally interfere with the plant dynamics and they typically have higher bandwidths than contacting-type alternatives. The sensors are selected based on their performance (bandwidth and resolution), size, mass, and cost. Complexity of the sensor processing electronics is also a factor.

Many types of non-contact position sensors exist, utilizing numerous physical principals. Two sensor technologies have been previously used in fast steering mirror implementations: inductive and capacitive. Capacitive sensor technology was ultimately selected for the sAFSM because its calibration is largely independent of target material properties, as long as the target is conductive[1]. Additionally, I wanted to avoid any potential interference issues due to the eddy current (inductive) sensors' close proximity to the electromagnetic actuators.

Small capacitive sensor probes generally have a cylindrical shape with a sensing head at one of the flats and a cable exiting from the opposite flat. Larger diameter sensors tend to give better resolution for a desired range and standoff distance. Resolution performance from the analog sensors is also a function of bandwidth. Thus, selecting a sensor model is a tradeoff between resolution, bandwidth, and size requirements. Note that capacitive sensors require a target diameter that is approximately 20% larger than the probe body. Therefore, resolution requirements can actually

[1] Aluminum, Beryllium, and gold-plated ceramics were initially considered for the target surface.

drive armature size and geometry in applications requiring very high precision.

If the armature target is assumed to be a stiff plane, a minimum of three sensors, typically arranged in an equilateral triangle, are required to fully resolve the tip and tilt angles plus $\hat{z}$ linear displacement. However, employing four sensors in a square pattern offers a number of benefits. First, since the four-core actuator concept is arranged into quadrants, it is natural to arrange the sensors in a similar pattern. Secondly, the calculation of tip and tilt angles, or rather a voltage proportional to angle, is simpler for a square-patterned sensor arrangement than for a triangle formation. For the square-patterned sensors, the angles are derived by averaging the sensor outputs and inverted outputs - a linear operation that is easily implemented in analog circuitry. If the sensor noise is uncorrelated, the averaging has the convenient side effect of improving noise performance by a factor of two (the square root of the number of sensors averaged).

The sAFSM design includes a provision for an optional fifth sensor in the center of the pattern, nominally aligned with the FSM's effective pivot. The fifth sensor permits the measurement of the armature $\hat{z}$ translation independently of rotation. Additionally, the range of the 5^{th} sensor can be set differently from the other four. For the sAFSM, the center sensor's range is set greater than the air gap length so that if the negative magnetic spring pulls the armature outside of the range of the outer four sensors, then the fifth sensor can be used as a feedback source to recenter the armature. Figure 5-1 shows the five sensor pattern with annotations detailing relevant sensor probe diameters.

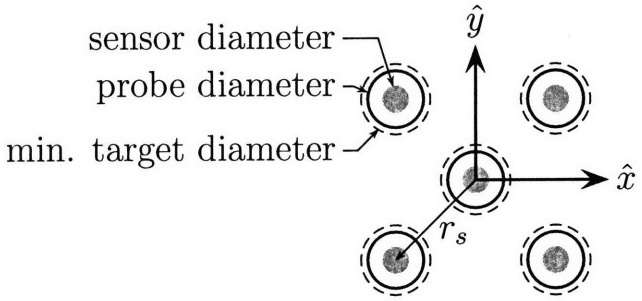

Figure 5-1: Sensor Pattern

Angular sensing performance depends upon the separation distance between the square-patterned sensors in addition to the individual sensor's performance. Assume that the sensor pattern centroid is aligned with the armature's effective pivot. Defining a sensor radius r_s as the distance from the pivot to an outside probe centerline (as in Figure 5-1), the sensor system resolution and range are:

$$\eta_{\hat{x}} = \eta_{\hat{y}} = \frac{\eta_s}{r_s}\frac{\sqrt{2}}{2}, \tag{5.1}$$

$$R_{\hat{x}} = R_{\hat{y}} = \frac{R_s\sqrt{2}}{r_s}, \tag{5.2}$$

where $\eta_{\hat{x}}$ and $\eta_{\hat{y}}$ are angular resolutions with respect to rotations about the $\hat{x}$ and $\hat{y}$ axes respectively, η_s is the individual sensors' linear resolution, $R_{\hat{x}}$ and $R_{\hat{y}}$ are angular rotation ranges, and R_s is the individual sensors' linear range. I've assumed that the sensor noise is uncorrelated; thus, averaging improves the resolution by a factor of two and hence the '2' in the denominator of the resolution expression.

Additionally, r_s must be large enough so that the sensor bodies are sufficiently separated so that they don't electrically interfere with each other. The sensor radius must also be large enough such that the change in target displacement over the sensor diameter is small compared with the change displacement over the sensor radius (see Figure 5-2). Since the sensor probe bodies posses few integrated mounting features, the sensor separation distance must be large enough to leave room for clamps or other fixturing features. And finally, the radius shouldn't drive the overall dimensions of the armature. That is, the sensor radius should be roughly equal-to or smaller-than the ring core radius determined in Section 5.1.

ADE Technologies model 2837 capacitive sensor probes with model 8800 conditioning electronics were selected for the sAFSM application. Individual sensor and sensing system performance estimates are given in Table 5.1 below.

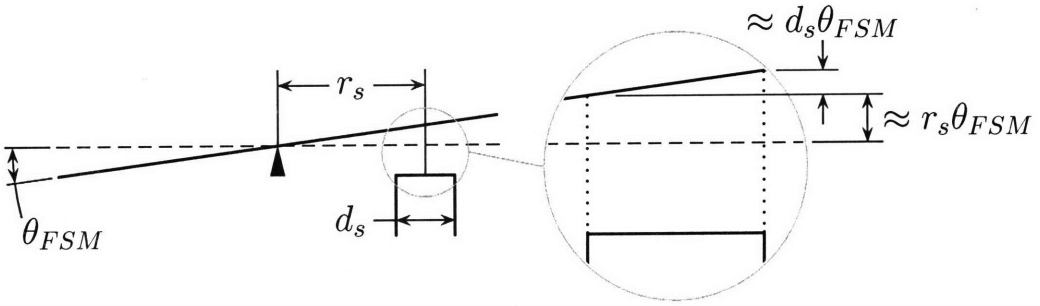

Figure 5-2: Sensor Side View

Table 5.1: ADE 2837/8800 Sensor and Sensing System Expected Performance

Sensor diameter		3 mm
Probe (outside) diameter		6 mm
Linear resolution	η_s	7 nm
Linear range	R_s	$\pm 150\,\mu$m
Sensor pattern radius	r_s	11.5 mm
Angular resolution	$\eta_{\hat{x}}$, $\eta_{\hat{y}}$	0.43 μrad
Angular range	$R_{\hat{x}}$, $R_{\hat{y}}$	± 18.4 mrad

5.3 Soft Magnetic Material Selection

Soft magnetic materials direct the magnetic flux in an actuator, analogous to conductors (e.g. copper) in electrical circuits. A number of material properties are key considerations in selecting the sAFSM soft magnetic materials. Permeability is the ease with which a magnetic flux is established within a material. More precisely, permeability is the ratio of flux density to magnetizing force[14]. Permeability is a similar concept to conductance in electrical circuits except that permeability is associated with energy storage rather than energy dissipation. High permeability is desired for the sAFSM actuator components because it reduces the magnetomotive force required to drive a quantity of flux through the magnetic circuit. Thus, the coil, permanent magnet, and core cross sections can be made smaller. Also, high permeability materials reduce the tendency for flux to leave (i.e. leak from) the magnetic conduit. Leakage flux causes actuator nonlinearities. Using high permeability materials also simplifies magnetic circuit analysis since the magnetomotive force dropped through the material becomes insignificant compared to that dropped in the air gaps.

In most "magnetic" materials, including the ferrous metals considered for the sAFSM design, permeability is nonlinear and hysteretic. Magnetic hysteresis is a consequence of an energy loss mechanism associated with changing the alignments of magnetic domains within the material. Thus, for soft magnetic materials that guide alternating flux, materials with smaller hysteresis loops are preferred to minimize losses.

Permeability at low levels of applied MMF is usually quite high (e.g. up to 100,000 times the permeability of a vacuum) but decreases significantly at higher magnetomotive force levels. At some point, continuing to increase magnetizing force results in only a small increase in the flux through the material. The flux density at such a point is called the saturation induction. Materials with high saturation induction are desired for the sAFSM design. The UFM force expression (3.3) (and similarly the ring core actuator torque expression) suggests that for a given top and bottom flux levels, force can be increased by reducing the pole area. However, saturation limits the amount of flux that can effectively flow through an area and thus, the pole area cannot be arbitrarily reduced. Higher saturation induction materials permit smaller pole areas and therefore increase the actuator's force / acceleration capability. Additionally, high saturation materials reduce overall actuator size since the magnetic components can be made smaller.

A time-varying magnetic flux in electrically conductive materials induce eddy currents that, per Lenz's law, oppose the change in flux. These eddy currents dissipate power through ohmic (i.e. I^2R) heating. The power loss is, of course, undesirable because it requires additional input power to overcome and raises the temperature of the core material. Resistive soft magnetic materials limit the eddy current magnitude and thus reduce the loss. Unfortunately, materials with high permeability and saturation induction tend to be reasonably good conductors. A commonly used "trick" to increase effective resistance is to divide the core into many slices separated by thin resistive layers. Such "laminated" or "tape-wound" cores can reduce eddy current effects by factors exceeding 500,000[11]. Laminated cores work by reducing the integral on the right-hand-side of Faraday's law, resulting in a smaller electric potential,

and by squeezing the eddy current into a smaller cross sectional area, increasing the effective resistance (i.e. $R = \rho \cdot l/A$).

5.3.1 Alternating Flux Material

Alternating flux cores, consisting of the 'C'-cores and the section of the ring core within the 'C'-cores' cut, must efficiently conduct flux at frequencies exceeding 5 kHz. Therefore, the laminated core construction mentioned above is essential to limit losses due to eddy currents. Several tape-wound core vendors commonly produce 'C' and ring shapes for high-performance electrical inductors and transformers. Standard vendor options for base metal materials include silicon-steel, various nickel-iron (Ni-Fe) alloys, cobalt-iron (Co-Fe), and amorphous iron. Furthermore, each metal is typically available in multiple strip thicknesses ranging from 10 to 300 μm [0.5 to 12 mils]. Each lamination is separated from its neighbor by a thin (4 to 20 μm) layer of insulating epoxy. This non-permeable epoxy occupies a significant fraction of cores constructed from thin laminations and reduces the effective saturation induction by up to 35%.

At 2.4 T, cobalt-iron's saturation induction is the highest amongst known materials and is one and a half times that of nickel-iron. Since actuator force is a function of flux density squared, an actuator constructed from cobalt-iron will have about 2.4 times more steady-state force capability than an identically sized actuator with nickel-iron cores. Equivalently, and more importantly for the sAFSM design, a Co-Fe actuator's core components could be less-than one-half the size of a Ni-Fe actuator for the same steady-state force output. Note the deliberate use of the "steady-state" qualification in the preceding sentences. Co-Fe is significantly more lossy for varying magnetic flux than Ni-Fe (a factor >5 at 400 Hz) dues to lower resistivity and a larger hysteresis loop (higher coercivity). Referring back to Section 2.4, the disturbance rejection power spectrum is dominated by low-frequency content. Additionally, much of the actuator's torque capacity is needed at low frequencies to overcome bearing stiffness when pointing away from the actuator's center. Thus, the size and low-frequency force advantages of a cobalt-based actuator could outweigh the high-frequency power

loss penalty in disturbance rejection applications.

I strongly considered using Co-Fe in the sAFSM design. However, I ultimately decided to specify 50 μm Ni-Fe tape after learning that the pricing and lead times premiums for Co-Fe cores were excessive for a Master's thesis project. Note that Kluk successfully used a 25 μm Ni-Fe tape-wound core in his fast steering mirror implementation[22]. I chose thicker laminations to improve the effective saturation induction (i.e. from 1.28 T to 1.38 T) at the expense of increased power loss at higher frequencies. Table 5.2 lists the magnetic properties of the 'C'-core and ring core component material.

Table 5.2: Tape-Wound Core Magnetic Properties[30][9]

Material	50%-50% Ni-Fe "Deltamax"
Saturation Induction	1.55 T
Relative DC Permeability	7,000 to 100,000
Lamination Thickness	50 μm [2 mils]
Stacking Factor	0.89
Effective Saturation Induction	1.38 T
Power Loss	121 $W/_{kg}$ (5 kHz,1 T)

5.3.2 Direct Flux Material

The ring armature concept figures (e.g. 3-5) show curved permanent magnets spanning adjacent 'C'-cores. While curved permanent magnets are theoretically manufacturable, they are not readily available. Instead, conventional cuboid (rectangular box) magnets are used with machined soft magnetic material completing the span between 'C'-cores. I've named these parts "direct flux (DF) pieces" because the PM flux flowing through them does not vary with time. Figure 5-3 is a bottom view of ring armature concept with gray direct flux pieces. Note that the DF pieces are segmented to facilitate actuator assembly.

Nominally, the DF pieces are not subjected to alternating flux and thus material resistance and magnetic hysteresis are not a concern. In fact, high conductivity is somewhat advantageous since eddy currents will resist any leaking alternating flux from traveling between 'C'-cores via the direct flux path. Selection of the material

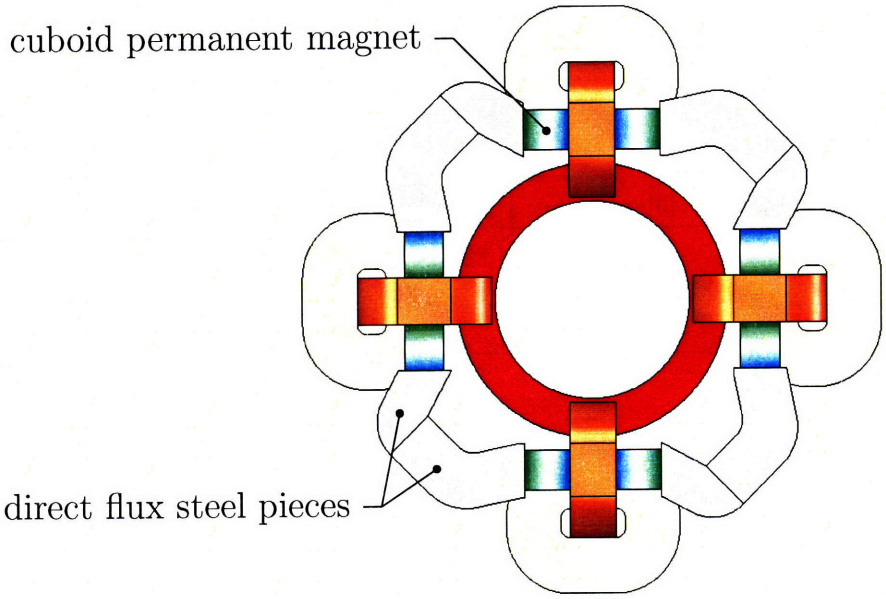

Figure 5-3: Direct Flux Steel Pieces (viewed from actuator bottom)

for the DF pieces proved surprisingly difficult despite, or perhaps because-of, the large number of materials that posses the desired magnetic properties. Nickel-iron alloys are the most permeable of any metal with maximum relative permeability exceeding 100,000 and, for alloys with approximately 50% nickel, have saturation inductance values of about 1.5 T[9]. After contacting several distributors I learned, unfortunately, that Ni-Fe is expensive in prototype quantities, not readily available in convenient forms, and is supplied in an anneal condition for machining. Optimizing the material for magnetic properties would require a post-machining anneal in a dry hydrogen atmosphere at 1175 °C [2150 °F]. Although local vendors are able to provide acceptable annealing services, I decided that the expense and effort were not worth the superior permeability.

Low carbon steels and martensitic stainless steels are easily obtained and have reasonable magnetic properties for non-alternating flux conduits. Annealed 1010 steel, for example, has a maximum relative permeability of 3,800 and type 410 and 416 stainless steels have relative permeabilities between 700 and 1000[1]. Saturation inductions for the metals typically exceed 1.5 T. I specified either type 410 or 416 stainless steel in the sAFSM design because I preferred its corrosion resistance and

because Montesanti had successfully used the material in his actuator design. Table 5.3 summarizes the direct flux material's magnetic properties.

Table 5.3: Direct Flux Pieces Magnetic Properties

Material	Type 410 or 416 stainless steel
Saturation Induction	1.7 T
Relative DC Permeability	700 to 1,000

5.4 Electromagnetic Components

5.4.1 Actuator Sizing

For now, let's ignore the differences between the AFSM and the ring core magnetic arrangement and only consider the flux in the armature top and bottom air gaps. The expression for AFSM torque, (3.7), from Section 3.2 is repeated below for convenience:

$$T = 2rF_Z = \frac{r}{A\mu_0}\left(\Phi_T^2 - \Phi_B^2\right).$$

The expression is a function of flux which, as explained above, is somewhat misleading because material properties effectively limit the maximum flux that can flow through a surface. Using $B = \Phi A$, (3.7) is converted into a function of flux density:

$$T = \frac{Ar}{\mu_0}\left(B_T^2 - B_B^2\right). \tag{5.3}$$

In order to preserve torque versus current and armature position linearity, the top and bottom net flux cannot change directions. Thus, the maximum possible torque occurs when the flux density in one gap is equal to the soft magnetic material maximum, B_{max}, and the flux density in the other is zero. Solving (5.3) for pole area at the maximum torque condition gives:

$$A = \frac{T\mu_0}{rB_{max}^2}. \tag{5.4}$$

Conservatively assuming the actuator torque radius r is equal to the ring core inside radius and using 1.38 T as the saturation induction results in a minimum area of $2.5\,\text{mm}^2$ to meet the 0.04 N·m torque requirement.

However, achieving a peak flux density difference of 1.38 T is difficult in practice because it requires a precise permanent magnet bias flux of half the core saturation induction. While a continuous range of permanent magnet flux is achievable by incrementally changing the permanent magnet area, a number of unpredictable or difficult to measure factors strongly affect the ultimate bias level. Such factors include the PM's as-manufactured residual magnetization, unintentional air gaps in the bias flux path, leakage flux, and differences from the expected soft magnetic permeabilities. Therefore, significant margin is added to the pole area; the as-designed size is 3×5 mm ($15\,\text{mm}^2$).

Knowing the pole area, it is possible to find the ring core outside diameter with simple geometry since the projection of the 'C'-core pole faces must lie completely with the ring core's flat, i.e. top and bottom, surfaces. Adding some tolerance for imperfect alignment during assembly, the ring core's outside radius is 4.8 mm longer than the inside radius for a total ring nominal OD of 29.7 mm. The ring core height is set just tall enough to avoid material saturation from the bias flux traveling between 'C'-cores. For the sAFSM, the height is slightly more than 3 mm.

The length of the air gap between the centered ring core and the 'C'-cores' cut faces must be, at a minimum, equal to the ring cores' outside radius multiplied by the armature's maximum angular range to prevent physical interference between the components. Thus, the air gap length must be greater-than 0.15 mm (14.8 mm×10 mrad). Generous margin is applied to the air gap length for alignment errors and as a hedge against accidentally driving the ring core into the 'C'-cores. The air gap length is specified at 0.3 mm [12 mils].

Ideally, the product of permanent magnet area and residual magnetization ($B_r A_{PM}$) is set to result in a pole face flux density of half the 'C'-core's saturation induction when the armature is centered with zero coil currents. The permanent magnet bias flux equation, (3.26b), is converted to physical design variables in the expression

below:

$$\boldsymbol{\Phi}_{\boldsymbol{N,PM}} \equiv B_r A_{PM} \frac{l_{PM} A}{l_{PM} A + 2 l_N A_{PM}} \begin{bmatrix} 1 & 1 & 1 & 1 & -1 & -1 & -1 & -1 \end{bmatrix}^T. \quad (5.5)$$

Solving the above for A_{PM} such that each value in the flux vector is $\pm B_{max} A/2$ yields:

$$A_{PM} = \frac{B_{max} A l_{PM}}{2 (B_r l_{PM} - B_{max} l_N)}. \quad (5.6)$$

The lengths of the permanent magnets shown in Figure 5-3 sum to 10 mm between 'C'-cores. Assuming a PM residual magnetization of 1.2 T (approximately valid for 35 MGOe grade neodymium-iron-boron magnets), the ideal permanent magnet frontal area for either the original or "two-level PM" configurations is 9 mm^2. Leakage flux is expected to significantly reduce the permanent magnet's effectiveness. As a hedge, the PM area is increased by 50% - to 13.7 mm^2 (3.2×4.3 mm).

Similarly, the minimum magnetomotive force is specified to drive the bias flux at the poles to either zero or B_{max}. Using the flux equations derived from the magnetic equivalent circuit in Chapter 3, a coil MMF of approximately 180 A·t is sufficient to drive the pole flux density to its material maximum.

Table 5.4: Actuator Size

Ring Core	21.3 mm ID, 29.7 mm OD, 3.2 mm height
'C'-core Cross Section	3.2×5.1 mm (16.1 mm^2)
Air Gap Length	0.3 mm
Permanent Magnet Grade	35 MGOe
PM Residual Magnetization	1.2 T
PM Frontal Area	3.2×4.3 mm (13.7 mm^2)
PM Length	10 mm
Coil Magnetomotive Force	180 A·t

5.4.2 Coil Windings

The magnetic equivalent circuit diagrams shown in Chapter 3 assume that an infinite quantity of coil-generated magnetomotive force is available to drive flux through the magnetic circuit. In reality, however, MMF is limited by current amplifier perfor-

mance and by thermal effects. Current flowing through finite conductance copper generates heat that will increase the temperature of the wires and surrounding material. For a properly designed coil, the I^2R energy will balance the actuator's capacity to conduct the heat away from the coil and the system will reach an elevated but reasonable steady state temperature under continuous operation. If the resistive heat input is excessive, high temperatures could melt the wire insulation, causing shorts between coil turns, or demagnetize the permanent magnets by surpassing their Curie temperature.

In lieu of creating a thermal model to asses the actuator's net thermal admittance, I've instead relied upon Prof. Trumper's rule of thumb that coil current density should be limited to $\approx 4\,{}^{A}/_{mm^2}$ in copper at DC (equivalent to a power density of 137 to $300\,{}^{kW}/_{m^3}$ for copper temperatures between 20 and 120 °C respectively). Higher current densities are sustainable only with special cooling effort like circulating water. The quantity of MMF available to the actuator is therefore a function of the physical volume devoted to the coils. Actually, the area reserved for the coils must be larger than the minimum area calculated from the current density limit because wire insulation and imperfect circular wire packing reduce the fraction of copper in the coil volume.

Linear amplifier outputs are typically limited by a maximum voltage and a maximum current. If an amplifier is already selected to drive the actuator, as is the case for the sAFSM, it is important to design the coils to remain within the amplifier's power envelope. Alternatively, if an amplifier is being procured or designed specifically for the actuator, it is important to predict the coil's electrical characteristic to optimize the amplifier selection. Conveniently, the ratio of voltage to current required from amplifier can be changed by adjusting the number of coil turns.

At low frequencies the coil voltage is simply equal to the product of the current and the wire's conventional ohmic resistance. But at high frequencies, the voltage is dominated by reactance, generated by a varying magnetic flux encircled by the coil. Applying Faraday's law along the coil wire path results in the following expression

for coil voltage:

$$v_c = N\frac{\mathrm{d}\Phi_c}{\mathrm{d}t}, \tag{5.7}$$

where v_c is the coil voltage, N is the number of turns, Φ_C is flux enclosed by the coil, and t is time. To keep from exceeding the amplifier's voltage limit, the maximum anticipated value for the time derivative of coil flux must be computed. The computation is somewhat trickier for the sAFSM than for an inductor or transformer because the flux, and hence its time derivative, depends not only upon the current in the coil but also upon armature position and currents in the other three coils. Using the flux relationships developed from the magnetic equivalent circuit (Section 3.3.4), simulations of the coil flux for both disturbance rejection and scanning acceleration profiles result in a maximum $^{\mathrm{d}\Phi_c}/_{\mathrm{d}t}$ of $0.22\,^{\mathrm{Wb}}/_{\mathrm{s}}$. Therefore, in order to keep the coil voltage below the amplifier's 33 V rating, the number of turns must be less-than 150. Likewise, the number of turns must be greater-than 12 to keep the per-turn current below the 16 A amplifier maximum.

If a single long wire is driven with a high frequency alternating current, where the meaning of "high frequency" depends on the wire's diameter, then the current will tend to flow near the conductor's perimeter. This phenomena, known as the "skin effect", is caused by eddy currents induced within the wire that reinforce the current flow at the surface and retard current flowing in the center. Similarly, if a group of closely packed wires is driven with an alternating current, then each wire's magnetic field will interact with its neighbors and the current density will additionally concentrate in portions of some of the wires. This phenomena is called the "proximity effect". Dixon provides an introduction to skin and proximity effects in [12] while others, such as Butterworth's 1922 paper[8], detail the mathematical basis for the phenomena. The consequence of the locally elevated current density is increased effective wire resistance because the current flows through a smaller area (i.e. A decreases in the $R = {}^{\rho \cdot l}/_{A}$ resistance expression). Therefore, the ohmic heating load will increase, exacerbating the thermal design problem.

Figure 5-4 is the output of a 2D magnetic finite element analysis study[2] showing the current density profile in an sAFSM-like actuator when driven with a 1 A peak, 50 kHz sinusoidal current (i.e. $i = \sin(2\pi f \cdot t)$, where $f = 50,000$). The coil consists of 32 series-connected windings of 16 gauge wire in a tight square-packed configuration. The DC (i.e. $f = 0$) current density is about 0.77 A/mm^2. When driven with the high frequency signal, the current density exceeds 20 A/mm^2 in some portions of the wires - an increase by over 25 times. Interestingly, the FEA program predicts that, for some of the wires, the current will actually flow in both directions (into and out-of the page) within the same wire! At 50 kHz, the coil's overall resistance increases by a factor of 60. Thus, if the coil was designed to dissipate the thermal power of, say, 1 A at DC, it must now cope with the equivalent of 30 A^3 of ohmic heating when driven with a 1 A amplitude, 50 kHz sine wave. Note that the FSM application is not expected to require a continuous, 50 kHz, full-torque driving current.

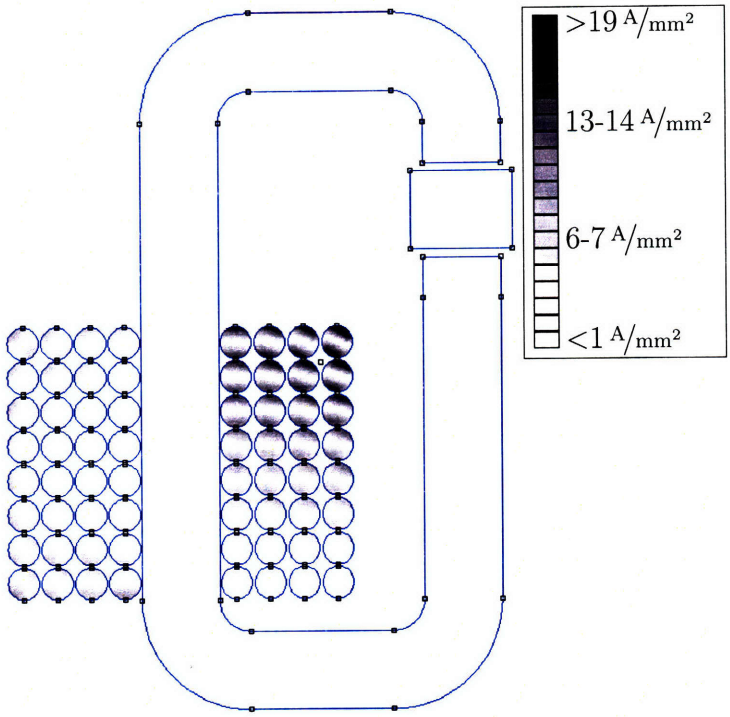

Figure 5-4: Solid Wire Current Density Magnitude at 50 kHz

[2]Produced with FEMM - Finite Element Method Magnetics[28]

[3]Alternating current resistive power is 1/2 DC resistive power assuming that the AC current amplitude is equal to the DC current value.

A common skin / proximity effect mitigation strategy is to decrease the diameter of the wire while increasing the number of parallel strands. Kluk, in his thesis, cited the skin effect as a secondary reason for switching to more turns of thinner (28 gauge) wire. Montesanti used Litz cables, which are prefabricated bundles of individually insulated thin wires, in his actuator coils to counteract skin and proximity losses. Ideally the copper area in the multiple parallel wire strands will sum to equal the copper area in the original single-strand coil, yielding an equivalent DC resistance. However, the packing efficiency of very small gauge wire is significantly reduced since the insulation occupies a greater fraction of the coil area (insulation requires a minimum thickness to be effective). For example, a coil built from square-packed, 16 AWG, heavy insulation wire is 72% copper but a coil constructed from 53×33 AWG Litz wire is only 48% copper. If the overall coil volume is not permitted to grow in size, then fewer parallel strands of the thin wire can be used and the coil's DC resistance will increase.

Figure 5-5 is a plot of solid and Litz wire resistance with respect to driving frequency for the sAFSM-like geometry in Figure 5-4. The "y" axis unit is resistance relative to the solid wire resistance at DC. The solid wire is 16 AWG and the Litz wire is 32 strands of 33 AWG. The Litz wire outside diameter is roughly equal to the OD of the insulated solid wire so that the coil volumes are the same. The solid and Litz wire traces are produced with the same magnetic FEA program that generated Figure 5-4. A third trace (green) shows the relative increase in resistance of a 16-gauge wire driven with alternating current in isolation, that is, without the proximity effect. Comparing the "solid" trace with the "skin-effect only" trace reveals that most of the solid wire AC resistance is caused by the proximity effect.

Figure 5-5 clearly shows Litz wire's superior performance above 2 kHz. If the actuator was expected to operate continuously at high frequencies, perhaps for a scanning application, coils constructed from Litz wire would be optimal. For the disturbance rejection application, however, much of the required MMF is at DC or relatively low frequencies. Therefore, the solid wire's low frequency resistance is advantageous. Table 5.5 summarizes the sAFSM coil parameters and characteristics.

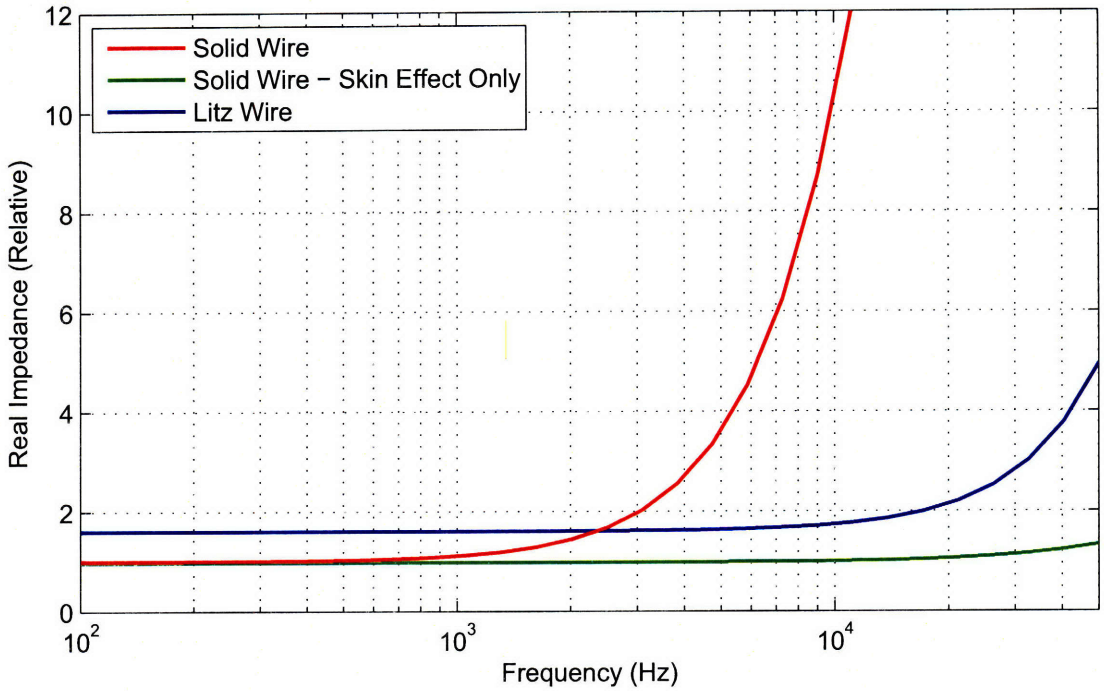

Figure 5-5: Coil Winding Relative Resistance vs. Frequency

5.4.3 Electromagnetic Finite Element Analysis

In order to validate the magnetic equivalent circuit (MEC) model of the sAFSM concept, I created a three-dimensional finite element model of the "two level PM" variation (Figure 3-13) using Maxwell® 3D by Ansoft. Fortunately, the actuator geometry is easily imported into the FEA application from the solid model files. Steady-state magnetic properties are then assigned to each component and a finite-

Table 5.5: Coil Parameters and Characteristics

Wire	16 AWG Solid Round
Number of Turns	32 (8×4)
Total Copper Area	41.8 mm^2
Coil Area	66.2 mm^2 (11.7×5.6 mm)
Coil DC Resistance	24 mΩ
Designed Max. Current Density	4 $^{A}/_{mm^2}$
Designed MMF	167 A·t
Maximum Current	5.2 A
Maximum Terminal Voltage	7.1 V
Coil Inductance	1.1 μH

sized "universe" with a vacuum permeability is created around the actuator to limit the problem domain. Lastly, an electric "circuit" is simulated at each of the coils by assigning a current density to a sheet inside of the 'C'-cores. Figure 5-6 is a screen-shot of Maxwell® 3D with the actuator model. Note that the model's coordinate convention does not match the conventions used throughout the rest of this thesis (i.e. $\hat{z}$ is normal to the mirror surface). The software's outputs have been manually remapped to the thesis coordinate conventions to avoid confusion.

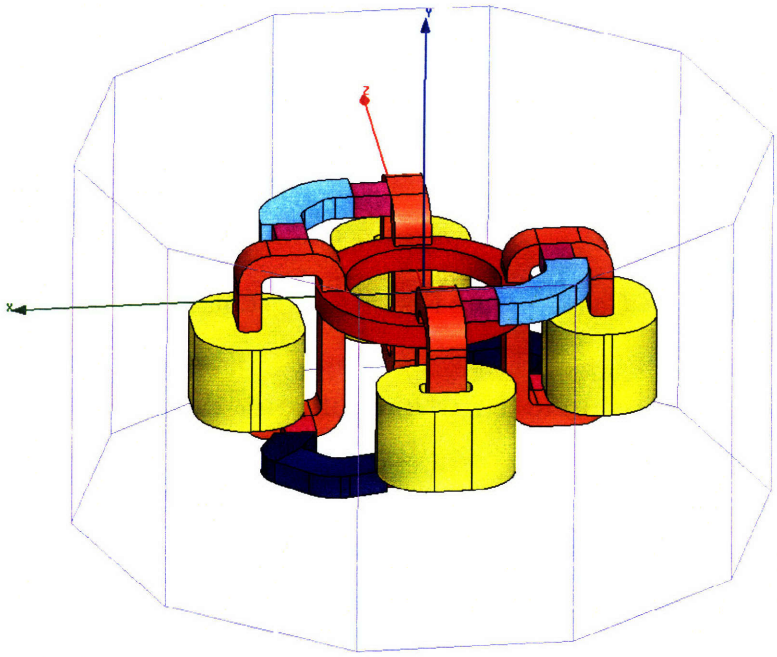

Figure 5-6: Magnetic Finite Element Analysis Model

Ansoft's meshing algorithm is iterative. That is, it repeatedly solves the system of equations and then refines the mesh based on the solution. The iterations stop when an output variable, like the force on the armature, converges sufficiently. The final mesh for the full sAFSM design (as opposed to a half or quarter model) requires between 60,000 and 100,000 tetrahedral 3D elements. Each FEA datapoint typically requires 10 to 40 minutes of computation time, depending on whether the application needs to re-iterate the mesh.

I had the FEA application compute a large number of solutions with varying values of coil common current, coil differential current, armature rotation, and armature $\hat{z}$

translation. The FEA outputs are three-element ($\hat{x}$, $\hat{y}$, $\hat{z}$) vectors of the force and torque applied to the ring core, a 4×4 inductance matrix, and the flux density at a set of models surfaces. Plots 5-7 through 5-11 show the FEA-computed and expected (from the magnetic equivalent circuit) forces and torques versus currents and displacements.

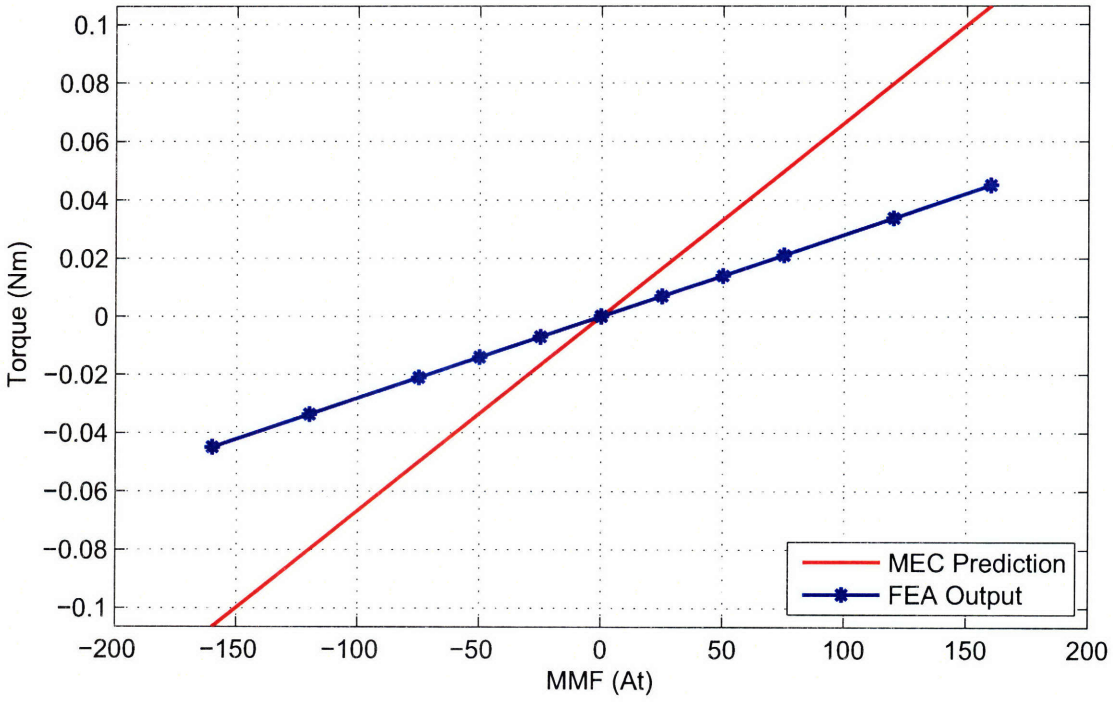

Figure 5-7: Torque versus Differentially Driven Coil Current

Figure 5-7 shows the centered-armature torque versus differentially driven coil current corresponding to the linear expression for T_{DX} in Section 3.3.5. The FEA computed curve confirms that the torque/current relationship is linear; however, the slope is a little less than one-half the expected value. The primary reason for the reduced torque constant is that the permanent magnet bias level in the finite element 'C'-core is 0.4 T, whereas the MEC estimate is 0.99 T. And, as the MEC equations predict, reducing the PM bias will linearly decrease the torque constant. The armature torque constant could be improved by using bigger (additional frontal area), longer, or stronger permanent magnets, decreasing air gap length, or by selecting higher permeability soft magnetic materials. However, even with the diminished torque constant,

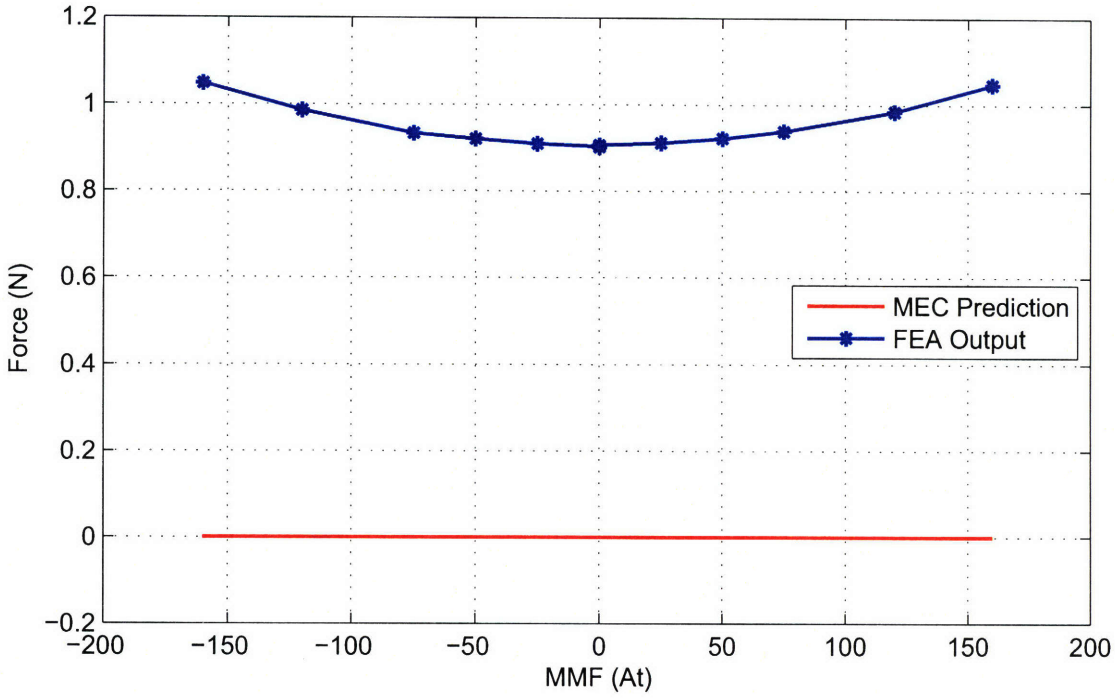

Figure 5-8: Mirror-Normal Force versus Differentially Driven Coil Current

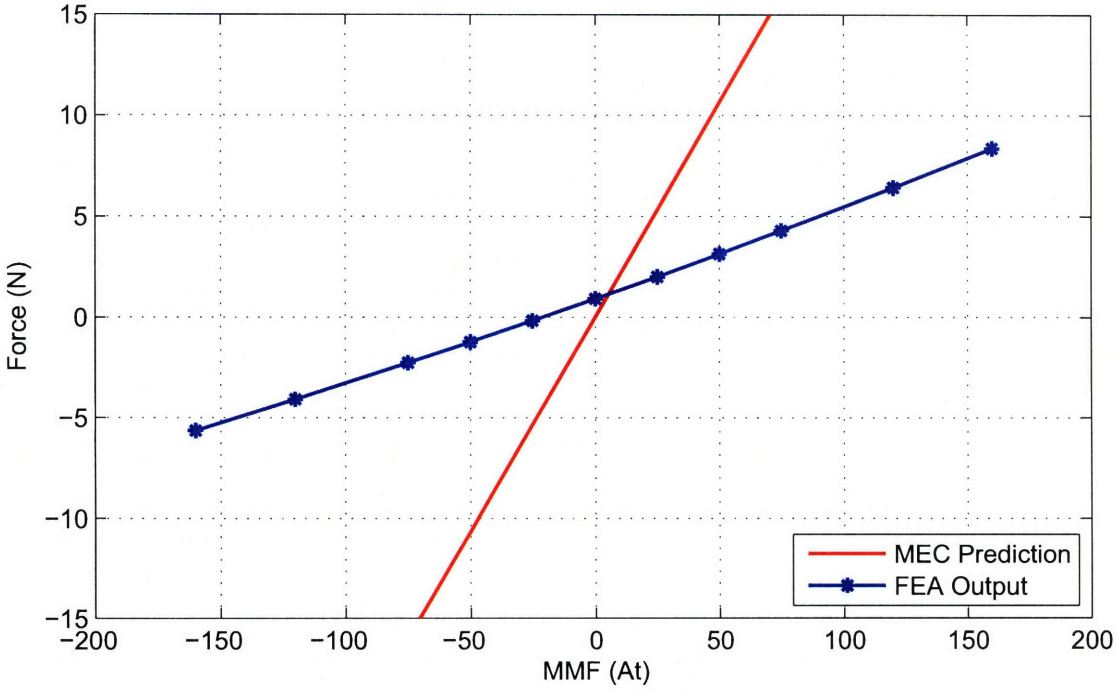

Figure 5-9: Mirror-Normal Force versus Commonly Driven Coil Current

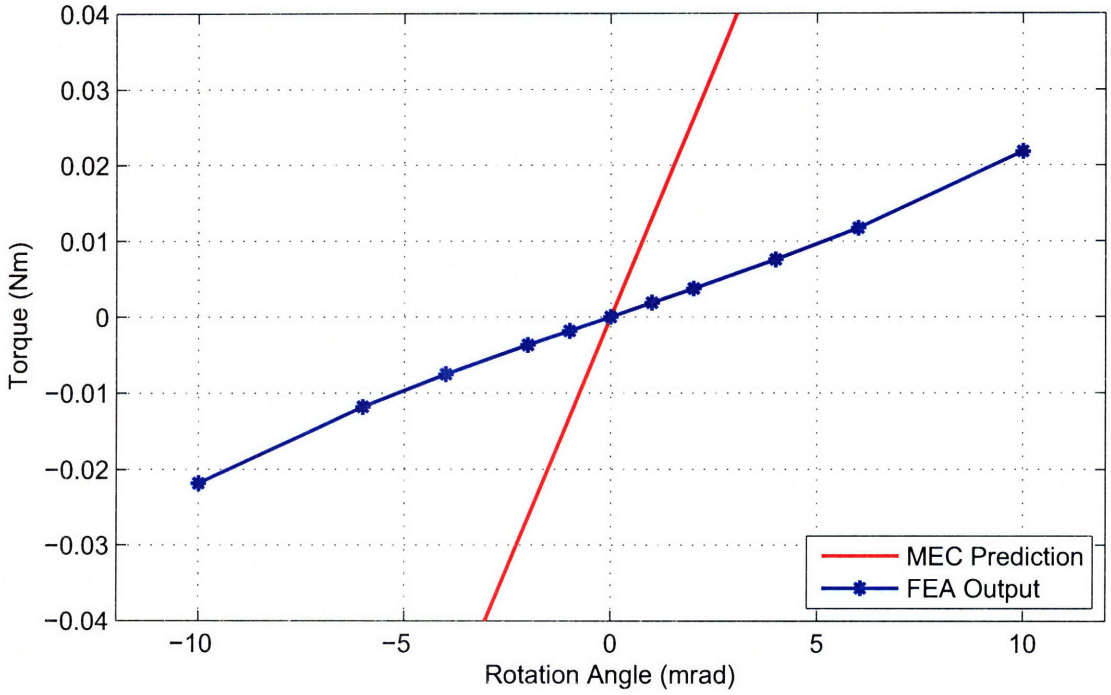

Figure 5-10: Torque versus Rotation Angle

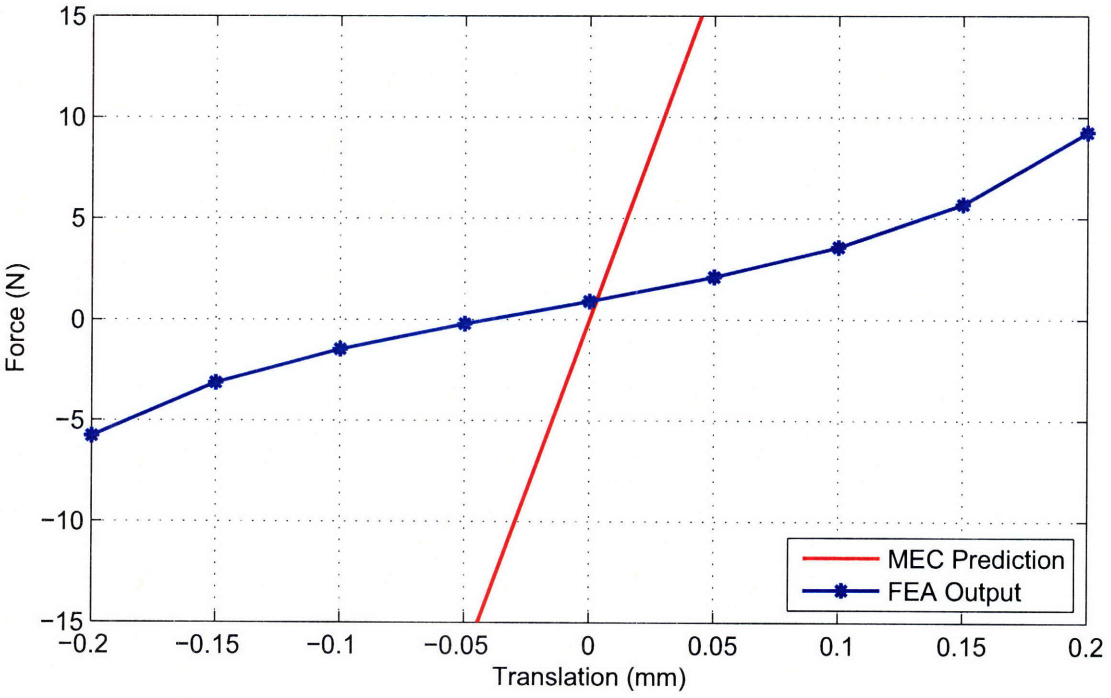

Figure 5-11: Mirror-Normal Force versus $\hat{z}$ Translation

the actuator meets the 0.04 N·m requirement.

Where has all the permanent magnet biasing flux gone? Well, a significant portion of it returns to the PM's south pole through the surrounding air and low-permeability housing material. Such flux, which doesn't flow through the 'C' and ring cores as the magnetic circuit assumes, is called leakage flux. The leakage flux can be illustrated with a planar flux density plot. Figure 5-12 shows the magnitude of the flux density along the plane identified in Figure 5-13. In this plot, the armature is centered and coil currents are zero. The FEA-computed flux density is color-encoded with warm hues representing areas with relatively high flux density while cool hues denote low flux density. The high flux density (red) rectangles are cross sections of the ring core and permanent magnets. Any area outside the rectangles is material with near-unity relative magnetic permeability. Thus, the green and yellow blobs surrounding the permanent magnets is leakage flux.

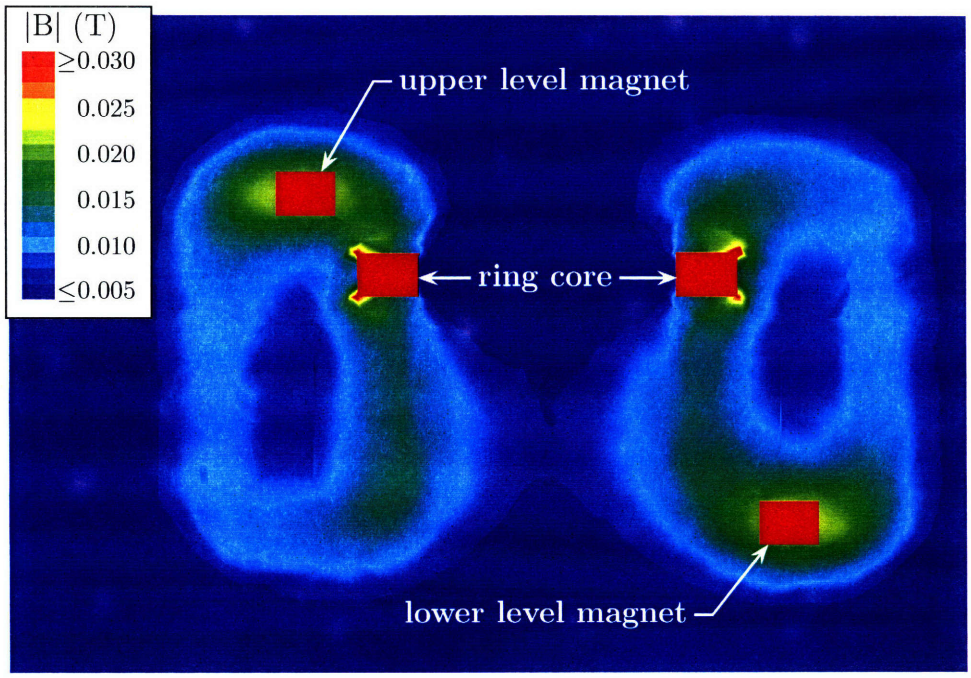

Figure 5-12: Flux Density Slice Bisecting Permanent Magnet

Figure 5-8 is the mirror normal ($\hat{z}$) force versus differentially driven coil current, i.e. $F_{DX,NET}$ in Section 3.3.5. In the plot, the zero current force has an offset of ≈0.9 N. The offset is caused by a small difference between the top and bottom air gap

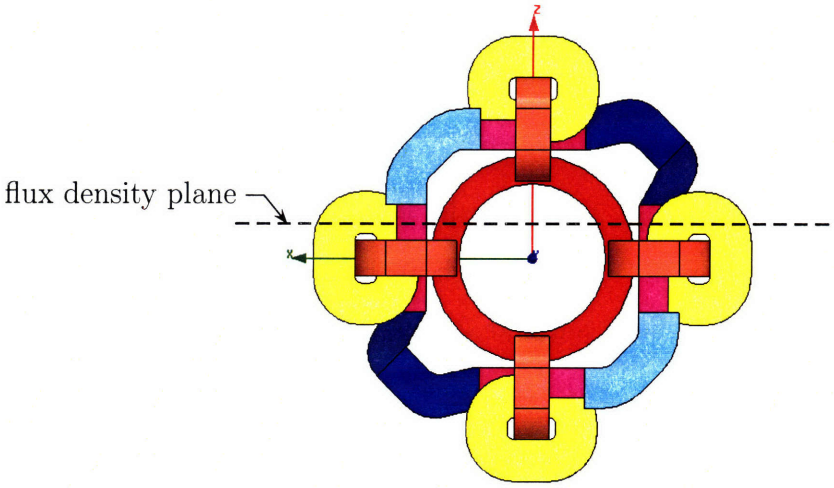

Figure 5-13: Flux Density Plane

flux density. Since the path length from the top magnets to the top gap is smaller than the bottom magnet to gap length, flux flows more readily to the top gap. The offset can be reduced or eliminated by adjusting the top or bottom permanent magnet size until the air gap flux densities equalize. Also, the force exhibits a nonlinear dependence upon differential current but, as shown in Section 3.4.1, the "two-level" variation should be immune to the troublesome but manageable nonlinearity. The cause is differences between the top and bottom magnet relative reluctances. Note that the magnitude of the nonlinearity is substantially reduced from what it would be with the original magnetic configuration (all bottom magnets).

Figure 5-9, showing force versus common coil current, Figure 5-10, showing applied torque versus armature rotation, and Figure 5-11, showing force versus armature translation, are all similar to Figure 5-7 in that the torque and force coefficients are less than expected due to the reduced PM bias level. Actually, the FEA curves in the displacement plots (Figs. 5-10 & 5-11) have slopes that are less-than one-fourth of the predicted values. Referring back to the MEC equations in Section 3.3.8, the rotational displacement toque coefficient (k_R) and the translational displacement force coefficient (k_L) both depend upon the square of the bias flux. Thus, for a FEA calculated PM bias level that is under half of the expected amount, the factor of 4+ difference in slopes is logical. Also, note that some nonlinearities are visible in

the displacement plots since the air gap reluctance is not truly linear with armature translation and rotation.

Lastly, an FEA-generated plot showing flux density vectors as color-encoded arrows is given in Figure 5-14. The armature is centered and the coils are not excited. Although the plot does not provide much analysis value, it is useful for visualizing the flux flow and the actuator's general operating principals.

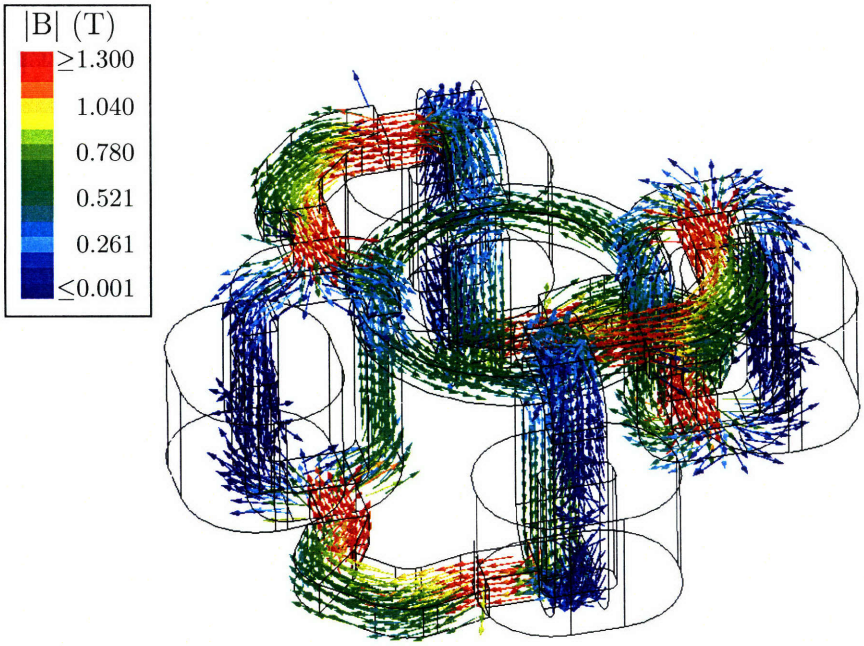

Figure 5-14: Flux Density Vector Plot

5.5 Mechanical Components

5.5.1 Armature Finite Element Analysis

Structural resonances, even those outside of the actuator to sensor load path, frequently limit maximum control bandwidth. In fact, decoupled structural modes constrain the bandwidth in the Lincoln heritage HBSM[20]. The resonances cause magnitude peaks in the sensor to actuator frequency response that, if severe enough, can "poke-though" 0-dB at frequencies above the -180° phase crossover and drive the system unstable. That is, the resonances reduce or eliminate the system's gain margin.

Control schemes exist to compensate for such resonances. However, they complicate the control design, possibly forcing the use of a digital controller, and they tend to be less robust. When the mechanical design is new, as with the armature, maximizing the frequency and damping of the first non-stiff, observable structural resonance is preferable to relying upon complex control strategies to maximize control bandwidth.

Finite element analysis is employed to predict and then optimize the resonant frequencies of the sAFSM armature. The optimization goal is to achieve a first resonant frequency above 18 kHz, about three times the open-loop unity magnitude crossover frequency requirement. The armature is modeled with free-free (i.e. unsupported) boundary conditions. In reality, of course, the armature is supported by elastomeric bearings. However, the bearings have a negligible effect on the structural mode frequencies because the rubber material separating the armature from the hard constraint (ground) is much softer[4] than the relatively stiff armature metal.

Figure 5-15 shows an exploded view of an early iteration of the complete armature assembly. The tape-wound ring core is encapsulated between two shells (a top shell and a bottom shell). The shells provide four flat faces for interfacing with the supporting elastomeric bearings, serve as a mounting surface for the mirror, and provide the target surface for the capacitance probe sensors. An epoxy layer with a 0.1 mm nominal thickness (not shown) bonds the core, top shell, bottom shell, and mirror to each other. Note that the shells' perimeter is retracted at four places to expose the top and bottom surfaces of the ring core for the actuator interface. Figure 5-16 is the corresponding unexploded view of the armature finite element model. The FEA model consists of 10,948 six-sided, 8-node, isoparametric (HEXA) elements. The mirror is excluded from the FEA model.

FEA Material Parameters

Determining material properties for the laminated ring core is somewhat challenging because it is a composite material of nickel-iron and epoxy. A considerable fraction of the composite is epoxy; and, since epoxy's modulus is significantly lower than that of

[4]The rubber effective elastic modulus is about 1/2000'th of the elastic modulus of aluminum.

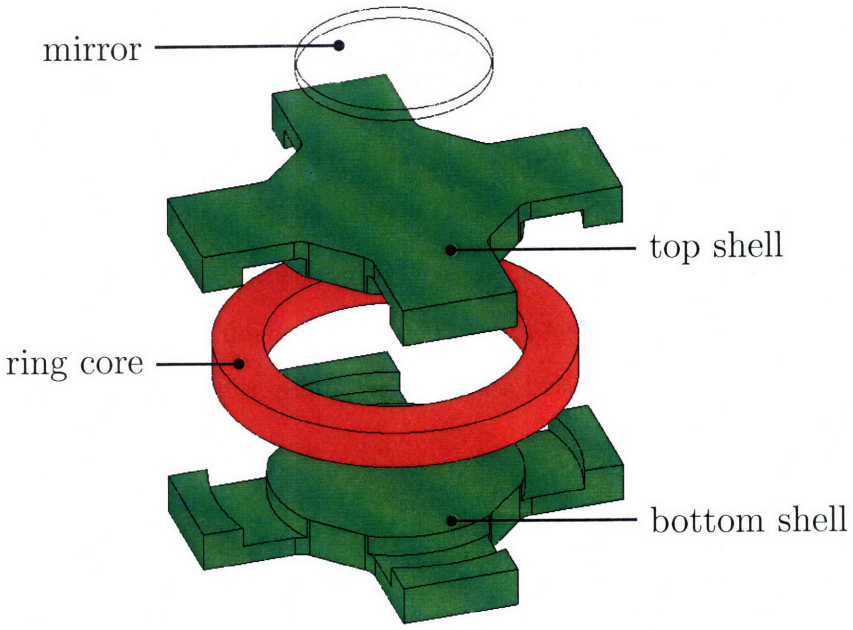

Figure 5-15: Initial Armature Model (exploded view)

Ni-Fe, the overall elastic modulus is likely less stiff than solid Ni-Fe. Additionally, the composite's ordered structure of alternating layers of metal and epoxy suggests that the composite material's stiffness has some directionality (anisotropy). Rick Montesanti faced a similar problem when he analyzed the stiffness of a laminated rotor for his 2005 PhD thesis project[31]. Following Montesanti's example, I've chosen to model the material as a transversely isotropic composite. The following development of elemental material properties is nearly identical to Montesanti but with some ad-

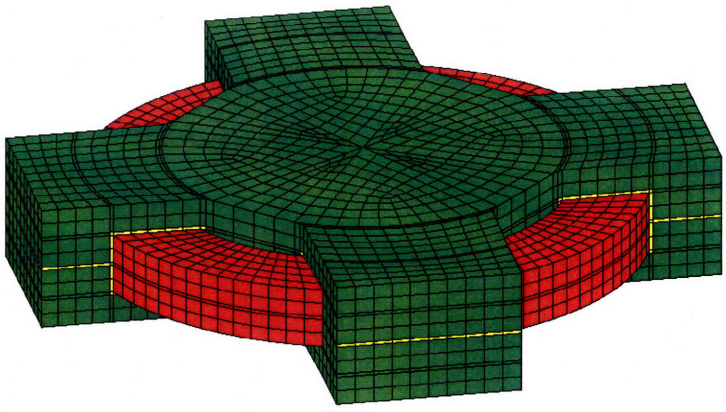

Figure 5-16: Initial FEA model with Material Colors

ditional derivations and a change due to differences in our respective FEA packages' compliance matrix axes conventions.

Figure 5-17 is a depiction of the tape-wound ring core from which a small cubic sample of material has been withdrawn. The figure also identifies the Cartesian coordinate system definition used in this analysis. The thin dark bands represent the layers of epoxy. Thus, the '1'-axis is perpendicular (normal) to the laminations while unit vectors '2' and '3' are both parallel to the laminations.

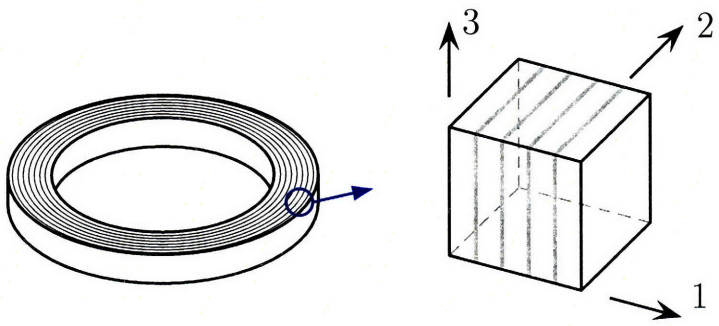

Figure 5-17: Laminated Composite

The material can be considered transversely isotropic because the material properties are independent of direction in the '2'-'3' plane at any point along the '1'-axis (with discontinues at the constituent material boundaries). The compliance matrix, relating the three-dimensional strain to 3D stress, is a function of five variables for transversely isotropic materials.[5] The compliance matrix is given in equation (5.8), where E_N is the net elastic modulus is the normal direction, E_P is the net modulus in the parallel directions, ν_{PN} is the Poisson ratio for a strain in the normal direction in response to a parallel direction stress, ν_{NP} is Poisson ratio for a parallel strain in response to a normal stress, and, if the subscript convention isn't clear yet, ν_{PP} is Poisson's ratio for a parallel strain in response to a stress in the other parallel direction. The values for the compliance matrix variables are computed from the

[5]A reduction from 9 variable for orthotropic and from 27 for fully anisotropic materials

constituent isotropic material properties according to equations developed below.

$$\begin{bmatrix} \epsilon_1 \\ \epsilon_2 \\ \epsilon_3 \\ \gamma_{12} \\ \gamma_{23} \\ \gamma_{31} \end{bmatrix} = \begin{bmatrix} \frac{1}{E_N} & \frac{-\nu_{PN}}{E_P} & \frac{-\nu_{PN}}{E_P} & \cdot & \cdot & \cdot \\ \frac{-\nu_{NP}}{E_N} & \frac{1}{E_P} & \frac{-\nu_{PP}}{E_P} & \cdot & \cdot & \cdot \\ \frac{-\nu_{NP}}{E_N} & \frac{-\nu_{PP}}{E_P} & \frac{1}{E_P} & \cdot & \cdot & \cdot \\ \cdot & \cdot & \cdot & \left(\frac{1+\nu_{PN}}{E_P} + \frac{1+\nu_{NP}}{E_N}\right) & \cdot & \cdot \\ \cdot & \cdot & \cdot & \cdot & \frac{2(1+\nu_{PP})}{E_P} & \cdot \\ \cdot & \cdot & \cdot & \cdot & \cdot & \left(\frac{1+\nu_{PN}}{E_P} + \frac{1+\nu_{NP}}{E_N}\right) \end{bmatrix} \begin{bmatrix} \sigma_1 \\ \sigma_2 \\ \sigma_3 \\ \tau_{12} \\ \tau_{23} \\ \tau_{31} \end{bmatrix} \tag{5.8}$$

The stacking factor[6], S, gives the volume fraction of metal in the composite and is easily calculated from the iron and epoxy layer thicknesses t_i and t_e respectively.

$$S = \frac{t_i}{t_i + t_e} = \frac{A_i}{A_i + A_e} \tag{5.9}$$

For the 0.05 mm [0.002 in] thick nickel-iron tape wound ring core used in this thesis, the vendor specified stacking factor is 0.89[30], which implies an epoxy layer thickness of about 6 μm. Since the lamination strip widths are equal, the stacking factor also relates the cross sectional iron material area (A_i) to the epoxy area (A_e) where the cross section is cut perpendicularly to the laminations. The epoxy volume fraction is simply one minus the stacking factor:

$$(1 - S) = 1 - \frac{t_i}{t_i + t_e} = \frac{t_e}{t_i + t_e} = \frac{A_e}{A_i + A_e}. \tag{5.10}$$

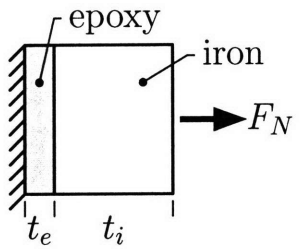

Figure 5-18: Single Layer Laminated Composite - Normal Force

[6]Called a "space factor" by some tape-wound magnetic core vendors.

The composite's net modulus of elasticity in response to a force normal to the laminations is found by analyzing the single composite layer (i.e. single lamina) shown in Figure 5-18. Equation (5.11) gives the familiar Hooke's law for the simple composite.

$$\frac{F_N}{A_N} = \sigma_N = E_N \frac{\Delta t_N}{t_N} \tag{5.11}$$

The total change in thickness (Δt_N) is equal to the iron's change in thickness (Δt_i) plus the change in thickness of the epoxy (Δt_e).

$$\Delta t_N = \Delta t_i + \Delta t_e \tag{5.12}$$

Applying Hooke's law to the iron layer provides an expression for the change in iron thickness:

$$\Delta t_i = \frac{t_i \sigma_i}{E_i}. \tag{5.13}$$

Montesanti identifies that the thick, stiff iron material constrains the thin epoxy layer's deformation in the directions parallel to the laminations. The epoxy, therefore, behaves according to uniaxial strain theory and it's effective elastic modulus stiffens by a factor of $\approx$1.78 per (5.14).

$$E_e^* = E_e \left(\frac{1 - \nu_e}{1 - \nu_e - 2\nu_e^2} \right) \tag{5.14}$$

And the resulting expression for the change in epoxy thickness is:

$$\Delta t_e = \frac{t_e \sigma_e}{E_e^*}. \tag{5.15}$$

Since the problem is static, the stress exerted on the epoxy is equal to the stress exerted on the iron, which is, in turn, equal to the overall normal stress.

$$\sigma_i = \sigma_e = \sigma_N \tag{5.16}$$

Equations (5.16), (5.15), and (5.13) are plugged into (5.12) to give:

$$\Delta t_N = \frac{t_i \sigma_N}{E_i} + \frac{t_e \sigma_N}{E_e^*} = \frac{E_i t_e + E_e^* t_i}{E_i E_e^*} \sigma_N. \tag{5.17}$$

Solving for E_N in (5.11) and plugging (5.17) in for Δt_N yields:

$$E_N = \frac{\sigma_N t_N}{\Delta t_N} = \frac{t_N E_i E_e^*}{E_i t_e + E_e^* t_i}. \tag{5.18}$$

Dividing the numerator and denominator of the above by the total thickness t_n, which is equal to the sum of the epoxy and iron thicknesses $(t_i + t_e)$, gives a final expression for normal composite modulus in terms of the stacking factor and constituent moduli.

$$E_N = \frac{E_i E_e^*}{E_i \frac{t_e}{t_i + t_e} + E_e^* \frac{t_i}{t_i + t_e}} = \frac{E_i E_e^*}{E_i(1 - S) + E_e^* S} \tag{5.19}$$

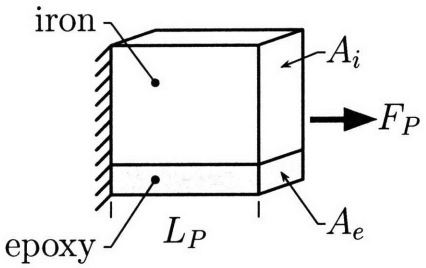

Figure 5-19: Single Layer Laminated Composite - Parallel Force

Figure 5-19 is an illustration of a single-layer iron-epoxy composite element with a stress in the parallel direction. Hooke's law for the simple element is given in equation (5.20).

$$\frac{F_P}{A_P} = E_P \frac{\Delta t_P}{t_P} = E_P \epsilon_P \tag{5.20}$$

The applied parallel force is opposed by the sum of the iron and epoxy elastic material forces F_i and F_e. The individual material forces are found by applying Hooke's law to the each constituent material:

$$F_P = F_i + F_e = E_i A_i \epsilon_i + E_e A_e \epsilon_e. \tag{5.21}$$

The parallel lamination geometry causes the iron and epoxy strains to be equal to each other and equal to the overall strain (i.e. $\epsilon_i = \epsilon_e = \epsilon_N$). Thus, the above expression for material forces simplifies to:

$$F_P = (E_i A_i + E_e A_e)\,\epsilon_P. \tag{5.22}$$

Solving (5.20) for E_P and plugging in (5.22) gives:

$$E_P = \frac{F_P}{A_P \epsilon_P} = \frac{E_i A_i + E_e A_e}{A_P}. \tag{5.23}$$

Recognizing that A_P, the elemental area facing the applied stress, is equal to the sum of the iron and epoxy areas gives a final expression for parallel composite modulus in terms of the stacking factor and constituent moduli.

$$E_P = \frac{E_i A_i + E_e A_e}{A_i + A_e} = E_i S + E_e\,(1 - S) \tag{5.24}$$

When the simple composite is stretched in the parallel direction, it will, like almost every other material[7], contract in the other two directions. The strain in the normal direction in response to a parallel stress (ϵ_{PN}) is equal to the parallel strain scaled by Poisson ratio ν_{PN}.

$$\epsilon_{PN} = \frac{\Delta t_{PN}}{t_N} = -\nu_{PN}\epsilon_P \tag{5.25}$$

The change in normal thickness due to the parallel stress is the sum of the change in iron and epoxy layer thicknesses:

$$\Delta t_{PN} = \Delta t_{PN,i} + \Delta t_{PN,e} = -t_i \nu_i \epsilon_P - t_e \nu_e \epsilon_P. \tag{5.26}$$

Solving (5.25) for ν_{PN} and plugging the above in for Δt_{PN} gives an expression for the Poisson ratio in terms of the constituent material individual thicknesses and

[7]The exception being rare polymers with negative Poisson ratios

homogeneous Poisson ratios.

$$\nu_{PN} = \frac{-\Delta t_{PN}}{t_N \epsilon_P} = \frac{t_i \nu_i + t_e \nu_e}{t_N} \tag{5.27}$$

As before, the total normal thickness t_n is the sum of the layer thicknesses and the expression for ν_{PN} can be rewritten as a function of the stacking factor.

$$\nu_{PN} = \frac{t_i \nu_i + t_e \nu_e}{t_i + t_e} = \nu_i S + \nu_e (1 - S) \tag{5.28}$$

The strain in the other parallel direction in response to a parallel stress is dominated by the iron strain, and thus:

$$\nu_{PP} = \nu_i. \tag{5.29}$$

Lastly, enforcing compliance matrix symmetry yields the expression for ν_{NP}:

$$\nu_{NP} = \nu_{PN} \left(\frac{E_N}{E_P} \right). \tag{5.30}$$

The assumed epoxy and iron isotropic material properties used in the analysis are given in Table 5.6. Note that the values I use for nickel-iron's properties differ slightly from Montesanti's. The computed composite material properties are given in Table 5.7.

Table 5.6: Composite Constituent Isotropic Properties

Material	Elastic Modulus	Poisson's Ratio	Density
Nickel-Iron (50%-50%)[9]	155 GPa	0.49	8180 $^{kg}/_{m^3}$
Epoxy	3 GPa	0.37	1300 $^{kg}/_{m^3}$

Table 5.7: Composite Material Properties

E_N	E_P	ν_{PP}	ν_{PN}	ν_{NP}	Density
21 GPa	138 GPa	0.49	0.48	0.07	7350 $^{kg}/_{m^3}$

Applying the transversely isotropic properties to the ring core elements in the finite element analysis software (MSC NASTRAN) is somewhat tricky because of ar-

mature's curved shape (as opposed to a convenient rectangular box shape like Montesanti's armature). By default, the orientation of anisotropic materials is determined by each element's particular material coordinate system. The material coordinate system (MCS) is, in turn, based on the locations and ordering of the element's nodes according to a complex set of geometric rules[33]. For HEXA-type elements, the material's '1'-axis is roughly parallel with line segment between the element's first and second nodes. Therefore, when I constructed the armature FEA model, I was careful to order the nodes such that the resulting '1'-axis generally pointed away-from (or, equivalently, towards) the armature center. However, accurately modeling the armature profile precluded the ideal orientation of the MCS for a number of elements (see Figure 5-20), resulting in errors of up to 30°. Fortunately, NASTRAN includes the capability for orienting the material with a global cylindrical coordinate system.[8] By setting the composite material orientation to a cylindrical coordinate system with its origin at the ring center, the '1'-axis (normal to the laminations) is aligned with the radial coordinate as desired.

The epoxy selected for bonding the armature shells and ring core is Hysol® 9394. This particular epoxy was chosen for several reasons. First, Lincoln Laboratory has significant experience working with 9394, including using it on previous spaceflight applications with low outgassing requirements. Additionally, Todd Mower, a Lincoln Laboratory staff member, has tested the material in a dynamic mechanical analyzer giving confidence in the measured properties. And finally, with a relatively high modulus of elasticity, shear strength, and working time, the epoxy's material properties are a good match for the armature structural bonding application.

Ideally, the shell material should have a high specific stiffness[9] and low density in order to maximize the armature's non-stiff modal frequencies and minimize its rotational inertia. High purity engineering ceramics, such as alumina or silicon carbide, posses high specific stiffness (95×10^6 and 130×10^6 $Pa\cdot m^3/kg$ respectively) with moder-

[8]If I had been aware of this feature before building the FEA model, I would not have gone through the hassle of carefully aligning the ring core elemental material coordinate systems with the armature center.

[9]Specific stiffness is the ratio of elastic modulus to density. The units of specific stiffness are $Pa\cdot m^3/kg$, which reduces to m^2/s^2.

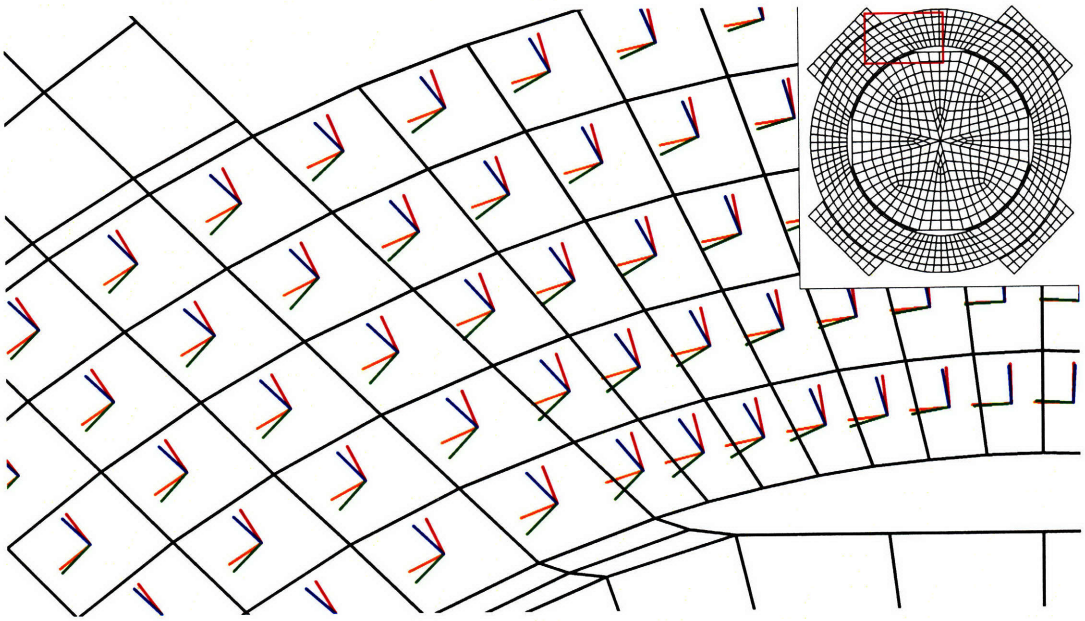

Figure 5-20: Elemental (blue/green) versus Global Cylindrical (red/orange) Material Coordinate Systems

ate densities (3900 and 3150 $^{kg}/_{m^3}$). In fact, Lu successfully used a precision machined alumina tube as the "backbone" in his linear fast tool servo's armature[26]. However, because post-fired ceramics are hard and brittle, they are difficult, and thus expensive, to machine into the small and intricate shell shapes with the required precision. Machinable ceramics exist, such as Macor® and Shapal-M®, but their specific stiffness tend to be lower (30×10^6 $^{Pa\cdot m^3}/_{kg}$). Additionally, the capacitive sensors require an electrically conductive target. Therefore, an insulating ceramic shell would need to be augmented with a conductive layer on its bottom surface. Lower purity alumina (96%, 81×10^6 $^{Pa\cdot m^3}/_{kg}$) ceramic substrates are commonly printed with an electrically conductive thick film for circuit board and heater applications. Such a film would be sufficiently thick to serve as the capacitive target. Alternatively, a conductive sheet could be bonded to the ceramic.

Unalloyed beryllium metal's very high specific stiffness (164×10^6 $^{Pa\cdot m^3}/_{kg}$) and low density (1850 $^{kg}/_{m^3}$) make it a nearly ideal material for the armature shells. Beryllium's toxicity to humans requires safety and environmental precautions during manufacturing, machining, and handling and, as a result, it is expensive and relatively

few machining shops work with the material. Thus, the use of beryllium is inappropriate for this thesis' demonstration hardware but it is a prime candidate for a flight-ready implementation. Aluminum, on the other hand, is readily available and easily machinable. Aluminum's specific stiffness and density properties ($25.5\times10^6\,^{Pa\cdot m^3}/_{kg}$ and $2700\,^{kg}/_{m^3}$) are acceptable but not nearly as supreme as beryllium. An aluminum shell is assumed for most of the structural finite element analysis presented in this thesis. A single FEA output is presented with a beryllium shell to give the normal modes of a flight-like armature.

Table 5.8: Shell Materials Isotropic Properties

Material	Elastic Modulus	Poisson's Ratio	Density
Aluminum	69 GPa	0.33	$2700\,^{kg}/_{m^3}$
Beryllium	303 GPa	0.1	$1844\,^{kg}/_{m^3}$

Structural FEA Results

Figure 5-21 shows the cross-sections of the various armature designs explored in the FEA-based modal analysis optimization. The figure also identifies each designs' first observable[10] resonant frequency (f_1) and rotational inertia (I). Design 'a' is the initial armature model and 'g' is the model selected for the thesis hardware fabrication.

Examining the figure reveals that both increasing the top and bottom shell thickness (design 'f') and decreasing the bearing diameter (i.e. smaller wings, designs 'b' through 'g') increase the first resonant frequency. However, the shells cannot be made arbitrarily thick nor can the bearing diameter be arbitrarily reduced. Thickening the shell increases the armature inertia (roughly by the square of the change) and drives the overall size of the actuator. The bearing diameter minimum dimension is constrained by manufacturing limitations - the thin wall between the bearing and the tape-wound core must be machinable. Hollowing-out the shells (as in designs 'c' and 'd') is a dead-end as it reduces the natural mode response without significant inertia reduction. Note that moving the epoxy bond between the shells from the center of

[10]Observable from either the capacitance probe or from a laser bouncing off of the armature top surface.

the armature to the bottom of the ring core (difference between designs 'b' and 'g') provides a manufacturing and assembly advantage rather than a modal response or inertia benefit.

Table 5.9 gives the first 10 (through 60 kHz) modal frequencies of the unsupported prototype armature (design 'g' with aluminum shells). For comparison, the first resonant frequency of design 'g' with a beryllium shell is 26 kHz, about 4.3 times the desired open-loop crossover frequency, and its rotational inertia is 1.04×10^{-6} kg·m^2. Assuming structural damping is the same and assuming a high frequency open-loop magnitude slope of -40 $^{dB}/_{decade}$, a beryllium-based armature provides an additional 6 dB of gain margin or, for the same gain margin, enables increasing the open-loop crossover frequency to 8.7 kHz. Additionally, the lower inertia of the beryllium armature results in an 18% increase in angular acceleration capability for the same torque level.

Table 5.9: Armature Modal Natural Frequencies

Mode Number	Frequency
1	18,369 Hz
2	22,916 Hz
3	36,571 Hz
4	36,608 Hz
5	36,608 Hz
6	48,293 Hz
7	52,552 Hz
8	54,630 Hz
9	55,071 Hz
10	59,683 Hz

Figures 5-22 through 5-24 show the first three mode shapes. Appendix D contains illustrations of mode shapes 4 through 10. Interestingly, the first few predicted mode shapes are identical to those of Kluk's armature even through the geometries differ significantly.

5.5.2 Rubber Bearing Selection

The negative spring stiffness produced by the PM bias flux is assessed by examining the slope of the magnetic FEA torque verses rotation plot (figure 5-10). The negative spring rate ranges from a minimum of -1.8 $^{N\cdot m}/_{rad}$ near the centered position to -2.5 $^{N\cdot m}/_{rad}$ at the extent. Designing a rubber bearing with a rotational stiffness of 4.8 $^{N\cdot m}/_{rad}$ results in a net stiffness within the desired 1 to 3 $^{N\cdot m}/_{rad}$ range. Table 5.10 gives the nominal dimensions of the elastomer bearing.

Table 5.10: Rubber Bearing Size

Material	Neoprene Rubber
Thickness	2.4 mm
Size	5.4×5.4 mm (29.2 mm^2
Shape Factor	0.56
Rotational Stiffness	4.8 $^{N\cdot m}/_{rad}$
Axial Stiffness	34 $^{N}/_{mm}$
Radial Stiffness	108 $^{N}/_{mm}$

5.6 sAFSM Solid Model

Figure 5-25 depicts the completed solid model of the small Advanced Fast Steering Mirror. Note the model's boundaries exceed the size goals somewhat. Features for vertically mounting the sAFSM to an optical table, such as the side ribs and base standoffs, add to the system size. If the sAFSM was mounted horizontally to a base (i.e. if the sAFSM was "lying down"), then the features would be unnecessary and the sAFSM would meet the size objectives. Table 5.11 summarizes the sAFSM's as-designed geometry and mass parameters. Note that the mass accounting does not include epoxy, coil potting material, or the machine screws to mount the sAFSM to the table.

Table 5.11: sAFSM As-Designed Size Parameters

Parameter	Goal	As-Designed
Size	63.5 × 63.5 × 36 mm	81.3×64.5×41.5 mm
Mass	0.8 kg	0.44 kg
Field of View	±50°	±52°
Aperture	16 mm Circular	16 mm Circular
Mirror	16 mm Circular	19×19 mm Square

5.7 Summary

This chapter presented the rationale for a number of important design decisions, including the diameter of the ring core, the type and arrangement of local feedback sensors, and the size of and material for the electromagnetic components. Unlike the previous "concept" chapters, this chapter considered non-ideal actuator phenomena like leakage flux and magnetic saturation. Such effects strongly influence the design and resulting performance. For instance, a 3D magnetic finite element analysis validated the ring armature electromagnetic principles but also showed that leakage flux greatly reduces the level of bias flux from the value predicted by magnetic equivalent circuit analysis. The lower bias flux results in diminished actuator toque and force constants as well as reduced magnetic spring rates. This chapter also presented a modal analysis optimization of the armature structure, netting an 11% increase in the first non-stiff resonance frequency and a 9% inertia reduction. Lastly, Figure 5-25 showed the solid model of the as-designed fast steering mirror.

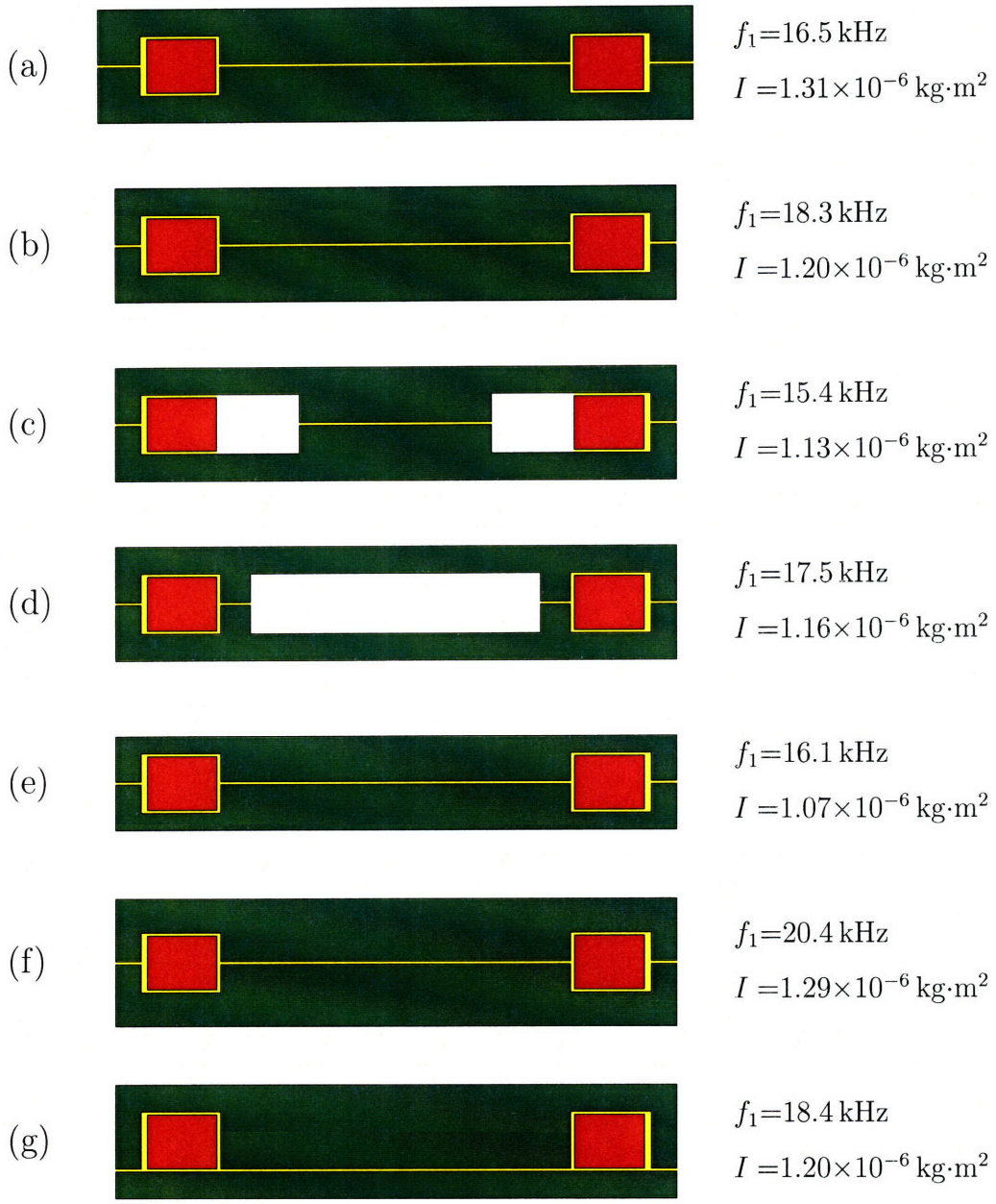

Figure 5-21: Armature Optimization Model Cross Sections

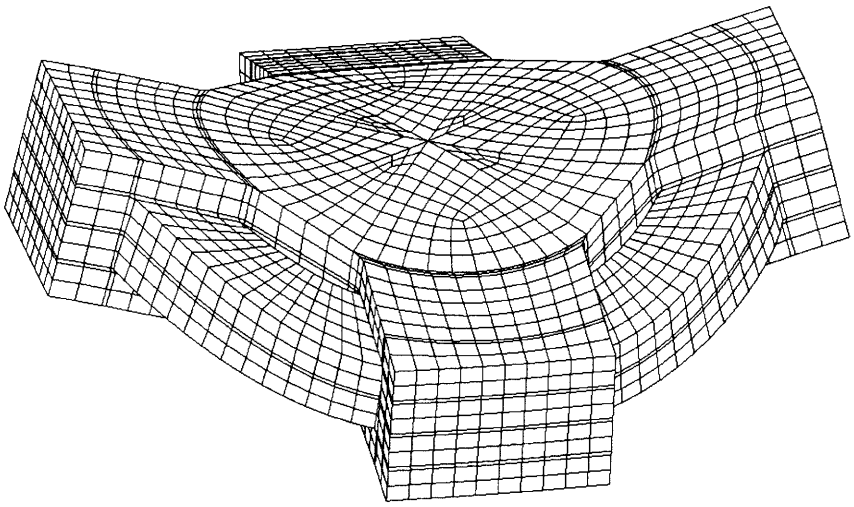

Figure 5-22: Mode 1, Alternately Flapping Wings, 18.4 kHz

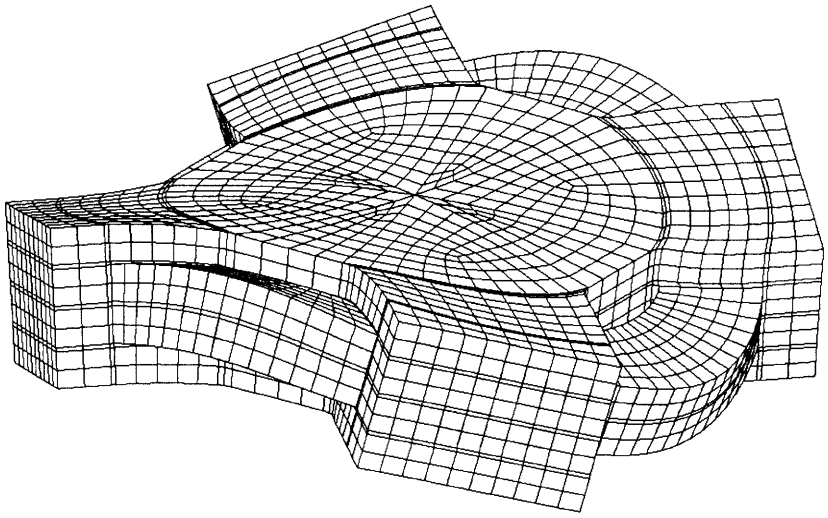

Figure 5-23: Mode 2, Saddle Surface, 22.9 kHz

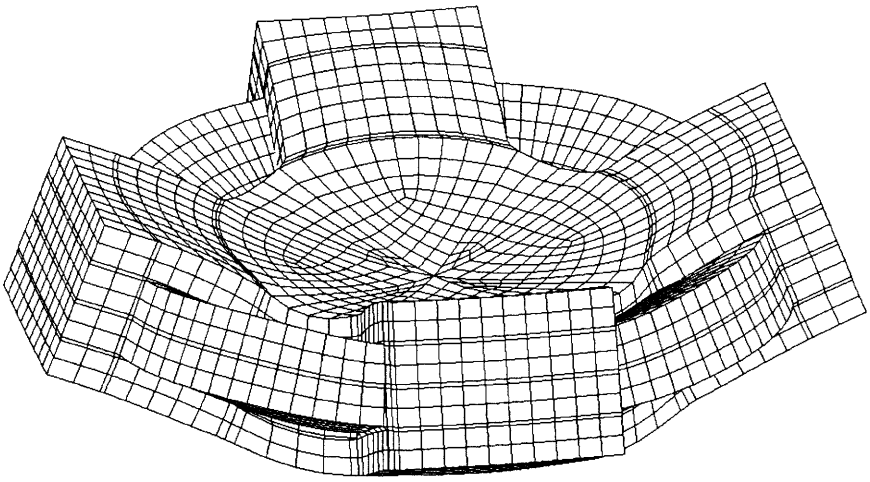

Figure 5-24: Mode 3, Commonly Flapping Wings, 36.6 kHz

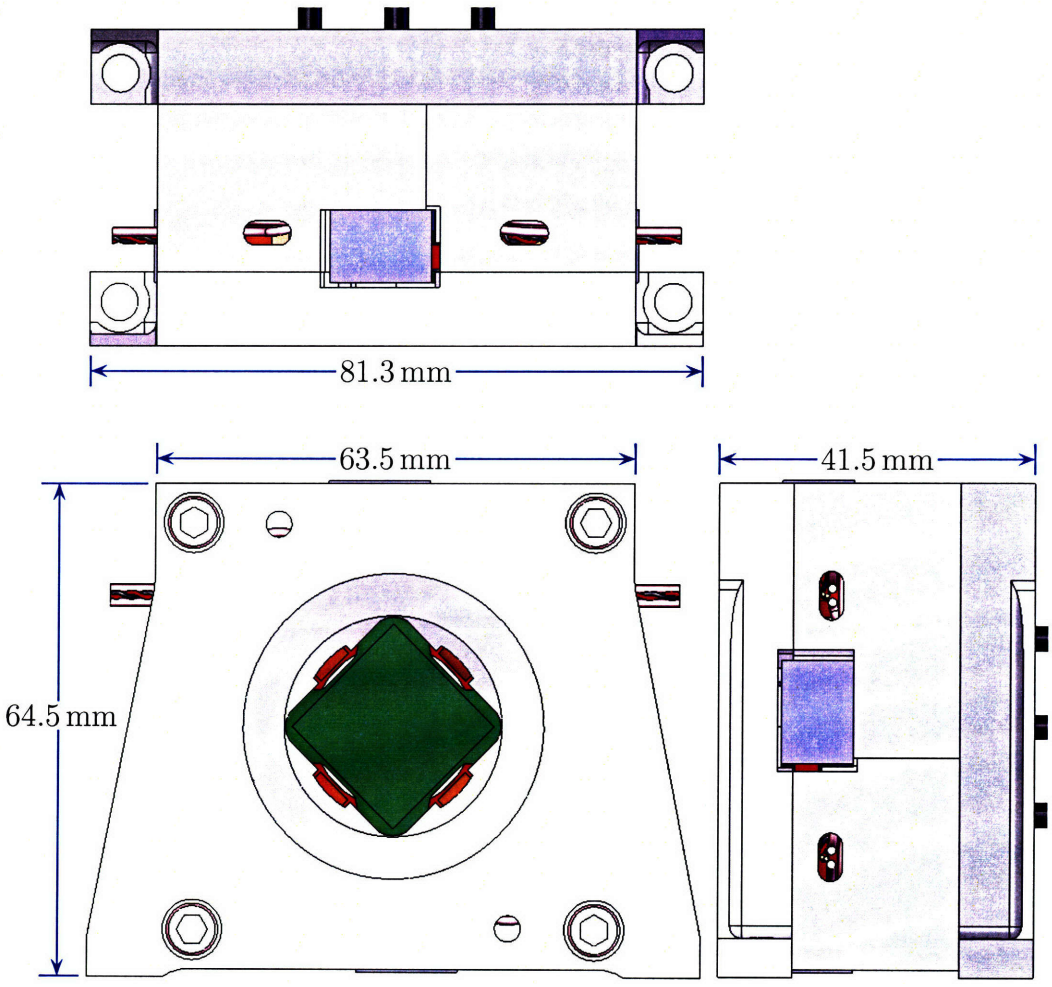

Figure 5-25: sAFSM Solid Model (actual size on 8.5"×11" paper)

Chapter 6

Conclusions and Future Work

In an article covering a NASA competition to improve spacesuit gloves, magazine author Jack Hitt provides the following description of mechanical design:

> Much of mechanical innovation boils down to finding just the right compromises to such puzzles. Many of us think of invention or innovation as a wholly conceived, brand-new, big-leap-forward creation unlike anything that has preceded it. But much of mechanical success involves fiddling with the inherent conflicts within a device until you find a tiny interstice among the countervailing forces, that sweet spot, where the device suddenly does what you want it to do.[17]

Hitt's quote, I think, accurately represents the development of the small advanced fast steering mirror. Like the spaceglove that ultimately won the competition, the sAFSM is very much an evolutionary design with a long ancestry. It is an improvement upon Kluk's AFSM design, incorporating a novel actuator concept that permits a beneficial reduction in size. Kluk's design, in turn, combines elements of Lu's linear fast tool servo and Loney's high bandwidth steering mirror. And, as the article suggests, many aspects of the sAFSM design require careful, and often times frustrating, balances between numerous trade-offs. Examples include bearing rotational stiffness versus mirror normal and lateral stiffness, increased control complexity versus system size, and lower packing efficiencies of small gauge wire versus high frequency

resistance of large diameter wire.

This chapter describes the present state of the sAFSM effort, discusses a couple avenues for future development, and provides a concluding summary.

6.1 Continuing Effort

The sAFSM project is an ongoing effort that we expect will include a hardware demonstration following the completion of this thesis. A parts set has been fabricated, including tape-wound Nickel-Iron cores and custom-sized permanent magnets. Additionally, capacitive probes and associated conditioning electronics for armature displacement sensing have been procured. Figure 6-1 is a photograph of the fabricated and procured parts with the exception of the copper wire coils. Currently, the sAFSM is being assembled. Figure 6-2 shows pictures of the bottom half of the 'C'-core and permanent magnets being dry fitted into an aluminum housing.

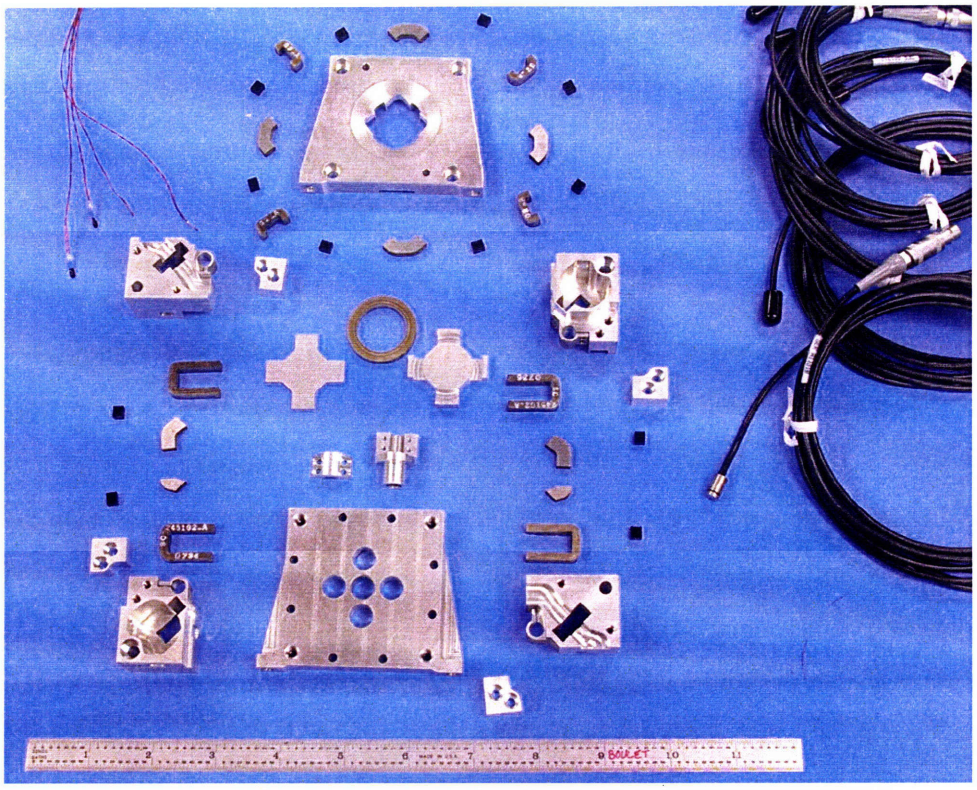

Figure 6-1: sAFSM Fabricated Parts Set, Excluding Coils

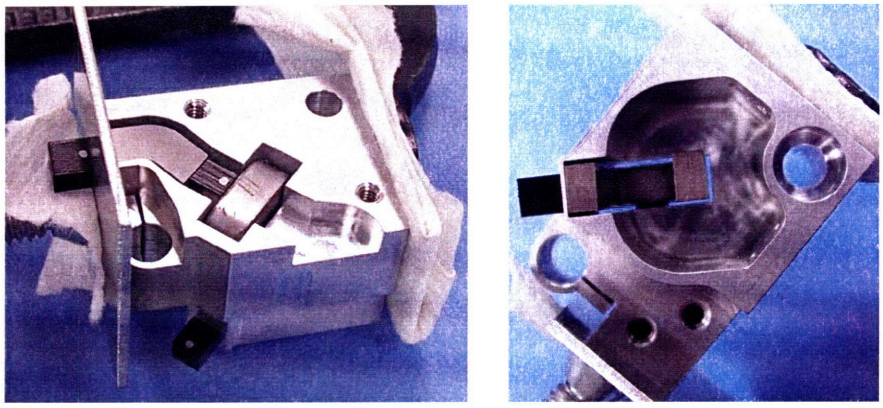

Figure 6-2: Dry Fitting a 'C'-core,Permanent Magnet, and Direct Flux Steel Piece

When the assembly is complete, system identification analysis will be performed by driving the coils with swept sinusoidal and random noise signals while simultaneously monitoring sensor outputs. Based on the resulting transfer functions, analog compensators will be designed to control the mirror tip, tilt, and mirror normal translation degrees of freedom using the capacitance sensors for feedback. A second set of compensators will be designed to control tip and tilt using optical position feedback. Much of the equipment and setup that Dan Kluk utilized for testing the AFSM, including the off-the-shelf linear power amplifiers, will be leveraged for experimenting with the small advanced fast steering mirror.

6.2 Suggestions for Future Work

The sAFSM hardware demonstration will likely generate many paths for future exploration as the ring core actuator concept and analyses are tested. However, a few suggestions for future consideration were identified during the sAFSM design phase.

6.2.1 Improve Acceleration Specification

As detailed in Section 2.4, the FSM's acceleration specification includes a very large margin, i.e. >5000%, as a reserve for unmodeled disturbance motion processes. The extra acceleration is useful if the sAFSM is required to perform a high-frequency

scanning function. However, if the FSM's expected applications are limited to disturbance rejection and low-frequency pointing offsets, then any excessive acceleration margin translates into unnecessary system size and mass. The largest source of disturbance noise not included in the original analysis is the non-rigid vibrations of the telescope structure and, ironically, the passive vibration isolators. Therefore, incorporating a characterization of the optical platform's dynamic behavior into the acceleration specification would decrease the need for high levels of margin. Unfortunately Dolye's finite element based dynamic analysis for the MLCD system[13] was not available when I determined the sAFSM requirements.

6.2.2 Cobalt-Iron Core Actuator

Nickel-iron was ultimately chosen as the tape-wound core material based on its relative availability and cost. However, cobalt-iron's larger saturation induction enables actuator designers to reduce core cross sectional area for similar levels of performance. Future analyses should quantify the potential FSM size reduction by stitching to Co-Fe cores. Additionally, such analyses should consider the ramifications of cobalt-iron's increased alternating flux core losses.

6.2.3 Magnetic Equivalent Circuit With Leakage Flux

The magnetic finite element analysis presented in Section 5.4.3 showed that leakage flux greatly influences actuator performance. Thus, the magnetic equivalent circuit developed in Chapter 3, which does not account for leakage, isn't very useful for accurately predicting actuator forces or torques. However, relying on the magnetic FEA to report actuator outputs for a series of displacement and current permutations, to perform an electromechanical simulation for example, isn't feasible as each FEA datapoint takes significant computation time. A magnetic equivalent circuit that accounts for flux leakage would, therefore, be advantageous.

Developing a "leakage aware" MEC would require adding reluctances modeling the leakage flux effect to the existing magnetic circuit diagram. Specifically, reluc-

tances would be added in parallel with the permanent magnet flux sources, effectively decreasing the value of $\mathscr{R}_{PM}$, and in series with the coil MMF sources. Values for the leakage reluctances could be determined from the flux reported by the finite element analysis software. For example, the PM leakage reluctance could be figured by comparing the quantity of flux flowing through a cross section of a magnet's center with the corresponding return flux in a slice of the ring core. Lu[26] similarly assessed the impact of leakage flux in the UFM design by counting 2D flux lines. Alternatively, the reluctances could be derived by adjusting their values until the force and torque versus current and displacement curves match the FEA output (i.e. Figures 5-7 through 5-11).

6.3 Conclusions

This thesis presents a design for a 16 mm aperture, high performance fast steering mirror that is dramatically smaller than Dan Kluk's prototype AFSM or the Lincoln-heritage HBSM. The size reduction is enabled, in part, by a new ring armature magnetic configuration. The ring armature concept is this thesis' primary contribution to fast steering mirror technology. The concept permits moving the biasing permanent magnets from a crowded section of the FSM to a formerly underutilized volume. The configuration is also advantageous because it eliminates the dependence upon the small area epoxy bond between the armature and mirror structure that failed in Kluk's testing.

The electromagnetic design is analyzed with a leakage-free magnetic equivalent circuit to yield expressions for torque and force as functions of coil current and armature displacement. A three-dimensional magnetostatic finite element analysis validates the MEC model, although leakage flux significantly reduces the torque and force constants from their nominal values. Another noteworthy contribution is this thesis' consideration of the expected coil current frequency profile when selecting coil wire diameter. Lastly, a modal analysis of the moving armature structure gives confidence that the sAFSM will support an open-loop crossover frequency of 6 kHz or higher.

THIS PAGE INTENTIONALLY LEFT BLANK

Appendix A

Power Spectral Density

Power spectral density plots of random disturbance signals are used throughout this thesis. Numerous sources discuss the mathematical basis and properties of the PSD. I've primarily relied upon Section 1.3 of Stoica and Moses[35] and Chapter 3 of Barkat[2]. Additionally, Jabben's 2007 PhD thesis[21] is a useful reference. Jabben provides a nice, concise overview of spectral analysis and subsequently applies it to improve the controller and plant design of a magnetically suspended rotating platform in the presence of stochastic disturbances.

This appendix repeats a subset of the equations given in Jabben's thesis that define power spectral density and, more relevantly, show how the PSDs are used to calculated the average disturbance power. Additionally, a convenient algorithm for integrating a series of straight line segments on a log-scale plots is presented.

A.1 PSD Definition

Signal $x(t)$ is a sample function of a continuous time, real-valued stochastic variable and is valid for all time t. The autocorrelation, $R_{xx}(\tau)$, of $x(t)$ is:

$$R_{xx}(\tau) = \lim_{T\to\infty} \frac{1}{2T} \int_{-T}^{+T} x(t-\tau)x(t)\mathrm{d}t. \tag{A.1}$$

Notice that the autocorrelation function with $\tau = 0$ is the average power of signal $x(t)$. It is also, by definition, equal to the square of the signal's root mean square (RMS) value, x_{RMS}, and it is equal to the sum of the squares of the signal mean, $\bar{x}$, and standard deviation, σ_x:

$$\begin{aligned} R_{xx}(\tau = 0) &= \lim_{T\to\infty} \frac{1}{2T} \int_{-T}^{+T} x^2(t)\mathrm{d}t = P_{ave}, \\ &= x_{RMS}^2, \\ &= \sigma_x^2 + \bar{x}^2. \end{aligned} \tag{A.2}$$

One definition of power spectral density is the Fourier transform of the autocorrelation function:

$$S_{xx}(f) = \int_{-\infty}^{+\infty} R_{xx}(\tau)\mathrm{e}^{-\mathrm{j}2\pi f\tau}\mathrm{d}\tau, \tag{A.3}$$

where f is frequency in hertz. If given a PSD, then the autocorrelation function can be determined with the inverse Fourier transform:

$$R_{xx}(\tau) = \int_{-\infty}^{+\infty} S_{xx}(f)\mathrm{e}^{\mathrm{j}2\pi f\tau}\mathrm{d}f. \tag{A.4}$$

Equation (A.3) produces a two-sided power spectral density, i.e. it is defined for negative values of frequency. However, since $x(t)$ is strictly real, the autocorrelation function and its Fourier transform are even. Hence, PSD values for negative frequencies are redundant. Thus, its possible to redefine the PSD per (A.5) for only positive frequencies, netting a one-sided PSD. Except for this section, power spectral densities in this thesis are exclusively one-sided.

$$S_{xx}^{+}(f) = \begin{cases} S_{xx}(0) & f = 0, \\ 2S_{xx}(f) & f > 0. \end{cases} \tag{A.5}$$

Equation (A.4) is rewritten using the one-sided PSD as:

$$R_{xx}(\tau) = \int_{0}^{+\infty} S_{xx}^{+}(f)\mathrm{e}^{\mathrm{j}2\pi f\tau}\mathrm{d}f. \tag{A.6}$$

Evaluating the above for $\tau = 0$ gives an important result: the average power in the time domain is equal to the integral of the PSD (hence the name "power spectral density"):

$$R_{xx}(\tau = 0) = P_{ave} = \int_0^{+\infty} S_{xx}^{+}(f)\mathrm{d}f. \tag{A.7}$$

Thus, the signal RMS is the square root of the integral of the PSD:

$$x_{RMS} = \sqrt{\int_0^{+\infty} S_{xx}^{+}(f)\mathrm{d}f}. \tag{A.8}$$

And, the cumulative RMS function, used to plot Figure 2-5 for example, is:

$$x_{RMS}(f) = \sqrt{\int_0^{f} S_{xx}^{+}(\gamma)\mathrm{d}\gamma}. \tag{A.9}$$

A.2 Trapezoidal-Like Integration for Log-Scale Plots

Computing the RMS value from a PSD requires integrating the area under the curve (Eqn. (A.8)). PSD plots are often composed of straight-line segments on a log-log plot. Therefore, a function that computes the area under a straight line on a log-scaled plot would prove useful. The following formulates just such an equation and provides a Matlab script implementation. Note the method is akin to trapezoidal integration on a linear-linear scale. A function of the form:

$$y = kx^m \tag{A.10}$$

will produce a straight line on a log-log plot. Consistent with frequency response and PSD plots, we assume here that $x > 0$. The familiar form of a straight line equation, $Y = MX + B$, becomes apparent after taking the logarithm of the left and right sides of the above:

$$\log_{10} y = \log_{10}(kx^m) = m \log_{10} x + \log_{10} k. \tag{A.11}$$

Here $\log_{10} y$ is equivalent to Y, m is equivalent to M, $\log_{10} x$ is equivalent to X, and $\log_{10} k$ is equivalent to B. Given endpoints of the line segment defining the straight

line on the log-log plot: (x_1, y_1) and (x_2, y_2), m and k are found using similar triangles (the same method used to find M and B for linear plots). With reference to figure A-1:

$$\frac{\log_{10} x - \log_{10} x_1}{\log_{10} x_2 - \log_{10} x_1} = \frac{\log_{10} y - \log_{10} y_1}{\log_{10} y_2 - \log_{10} y_1}. \tag{A.12}$$

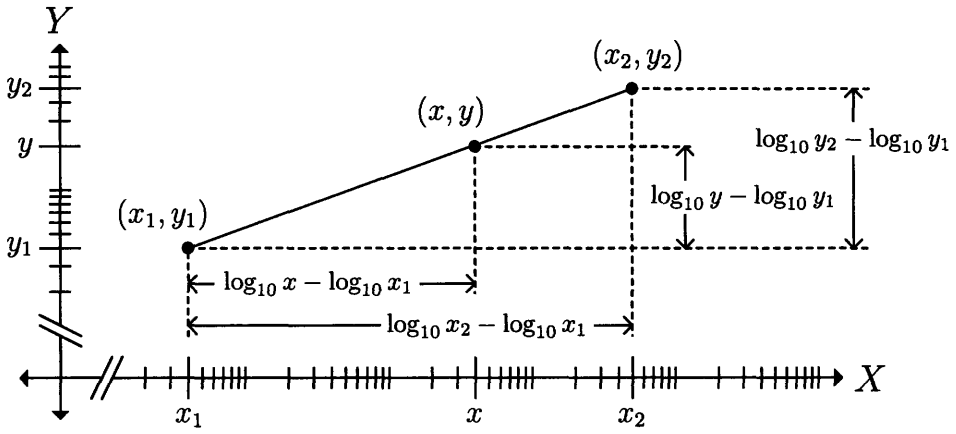

Figure A-1: Log-Log Plot Line Segment

Algebraic manipulation of (A.12) to isolate $\log_{10} y$ on the left-hand side produces:

$$\log_{10} y = \underbrace{\frac{\log_{10} y_2 - \log_{10} y_1}{\log_{10} x_2 - \log_{10} x_1}} \log_{10} x + \underbrace{\log_{10} y_1 - \log_{10} x_1 \frac{\log_{10} y_2 - \log_{10} y_1}{\log_{10} x_2 - \log_{10} x_1}}. \tag{A.13}$$

Note how the underbraced terms in the above correspond to m and $\log_{10} k$ in (A.11). Thus, an equation for m as a function of endpoint coordinates is:

$$m = \frac{\log_{10} y_2 - \log_{10} y_1}{\log_{10} x_2 - \log_{10} x_1}. \tag{A.14}$$

The expression for $\log_{10} k$, which is simplified by plugging in m, is shown below:

$$\begin{aligned} \log_{10} k &= \log_{10} y_1 - \log_{10} x_1 \frac{\log_{10} y_2 - \log_{10} y_1}{\log_{10} x_2 - \log_{10} x_1}, \\ &= \log_{10} y_1 - m \log_{10} x_1. \end{aligned}$$

Solving for k by inverting the log_{10} operator gives:

$$k = 10^{\log_{10} y_1 - m \log_{10} x_1} = y_1 x_1^{-m}. \tag{A.15}$$

Note that k is the value of y when x is 1.

The integral of y, (A.10), is:

$$\int y\,dx = \int kx^m\,dx = \begin{cases} \frac{k}{m+1}x^{m+1} + C & m \neq -1, \\ k \ln|x| + C & m = -1. \end{cases}$$

Thus, the integral under a straight line segment on a log-log plot between x_1 and x_2 is:

$$\int_{x_1}^{x_2} y\,dx = \begin{cases} \frac{k}{m+1}(x_2^{m+1} - x_1^{m+1}) & m \neq -1, \\ k(\ln|x_2| - \ln|x_1|) & m = -1. \end{cases} \tag{A.16}$$

Where m and k are found from (A.14) and (A.15).

In practice, computing the integral using (A.16) with finite precision arithmetic for values of m very close to -1 is somewhat troublesome. Summing -1 with $+1$ in both the denominator of the $K/(m+1)$ term and in the exponents of the x's results in a loss of precision. The numerical error resulting from the loss of precision is then magnified by the division and exponentiation operations. The error is illustrated in Figure A-2 with a plot of the difference between the formulas for the $m \neq 1$ and $m = 1$ cases as a function of $|m + 1|$ with arbitrary values for k, x_1, and x_2. We would expect the difference between the formulas to decrease as m approaches -1. And, it does for $|m + 1|$ greater-than $3{\times}10^{-10}$. But, as the difference between m and -1 approaches the machine's precision limit, the difference stops decreasing and actually grows.

For the purposes of this thesis, a thorough discussion of the numerical properties of (A.16), which would include an investigation of the relative error and its dependence upon variables k,x_1, and x_2, is unnecessary for two reasons. First, the algorithm is used to estimate the integrals of power spectral densities. Slopes of PSD plots on log-

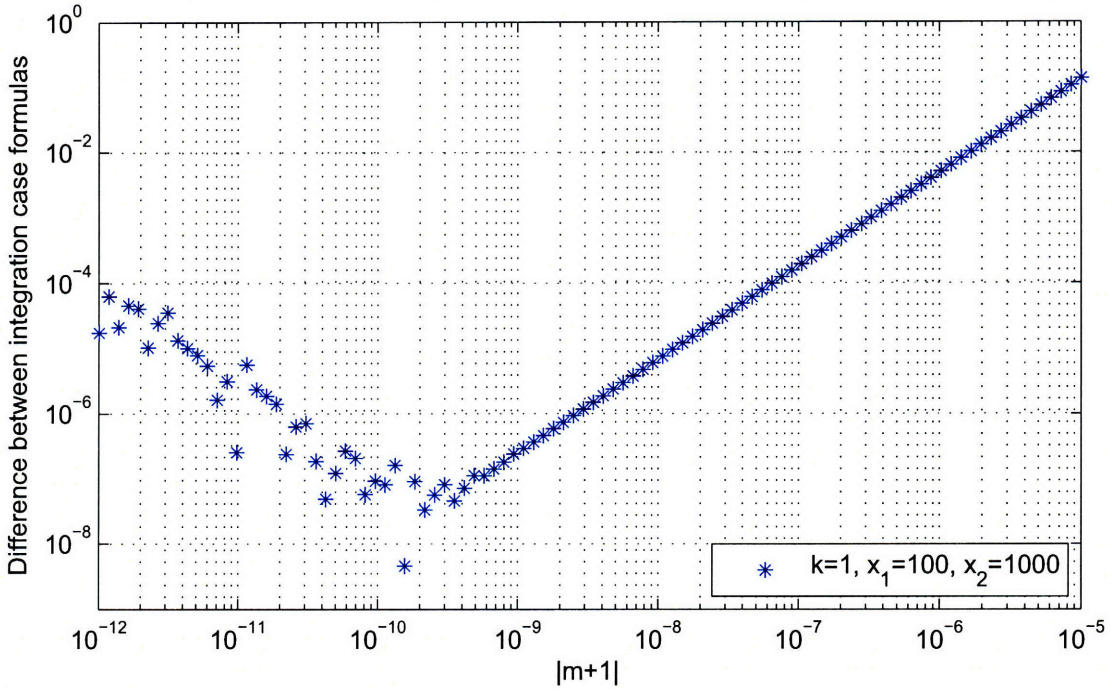

Figure A-2: Illustration of the Algorithm's Numerical Error for m Close to -1

log axes are rarely very close but not exactly equal to -1 over any significant frequency bandwidth. Secondly, the error relative to the integrated value isn't significant for the range of frequencies and values of k considered in this thesis, even if the slope is very nearly -1 over the entire frequency range. In the Matlab implementation (given below), I assume that any value of m closer than 1×10^{-5} to -1 is exactly equal to -1, thereby limiting the potential error. I've found that this results in a maximum relative error of 26 ppm over the 0.01 to 20,000 Hz frequency range.

The following Matlab script is an efficient implementation (i.e. it does not use any scripted for loops) of the formula developed above.

```
1 function z = trapz_loglog(x,y)
2 %TRAPZ_LOGLOG  Trapezoidal-like integration on log-log scale.
3 %   Z = TRAPZ_LOGLOG(X,Y) X and Y must be vectors of the same length.
4 %   X must be sorted and unique.  Function returns a vector with with
5 %   the same length as X and Y.  X and Y must be positive non-zero.
6 %   Each element Z(i) is an approximation of the integral of Y
```

```
7  %   between X(i-1) and X(i).  Element Z(1) is always zero as no
8  %   (X(0),Y(0)) pair exists.  The method of integration assumes that
9  %   the line segment between (X(i-1),Y(i-1)) and (X(i),Y(i)) is a
10 %   straight line on a log-log plot (logarithmic trapezoidal).
11 %
12 %   Z = TRAPZ_LOGLOG(Y) is identical to TRAPZ_LOGLOG(X,Y) where X is
13 %   assumed to be 1:LENGTH(Y) (i.e. unit spacing).
14 %
15 %   Compute the total integral with SUM(TRAPZ_LOGLOG(X,Y)).  Compute
16 %   the cumulative integral with CUMSUM(TRAPZ_LOGLOG(X,Y)).
17
18 if nargin == 2 % trapz(x,y)
19 elseif nargin==1 % trapz(y)
20     y = x;
21     x = 1:length(y);
22 else
23     error('MATLAB:trapz_loglog:numArgs', ...
24         'Invalid number of arguments.');
25 end
26
27 % make input into column vectors
28 if ¬isvector(x)
29     error('MATLAB:trapz_loglog:xNotVector', 'X must be a vector.');
30 elseif size(x,1) == 1
31     x = x.';
32 end
33 if ¬isvector(y)
34     error('MATLAB:trapz_loglog:yNotVector', 'Y must be a vector.');
35 elseif size(y,1) == 1
36     y = y.';
37 end
38 if length(x)≠length(y)
39     error('MATLAB:trapz_loglog:LengthXmismatchY', ...
40         'LENGTH(X) must equal LENGTH(Y)');
41 end
42
```

```
43 % check for negative or zero X and Y
44 if any( x≤0 | y≤0 )
45     error('MATLAB:trapz_loglog:NegOrZeroXY', ...
46         'X and Y must be non-zero and positive valued.');
47 end
48 % check for sorted X
49 if any(diff(x)<0)
50     error('MATLAB:trapz_loglog:UnsortedX', 'X not sorted.');
51 end
52
53 %
54 n = length(x);
55
56 % create log vectors for convenience
57 Lx = log10(x);
58 Ly = log10(y);
59
60 % compute slope on log-log plot
61 m = (Ly(2:n)-Ly(1:n-1))./(Lx(2:n)-Lx(1:n-1));
62
63 % slopes equal-to or near -1 are problematic
64 % TBD: be intelligent about deciding whether slopes are "near" -1
65 use_ln = find(abs(m+1)<1e-5)';
66
67 % compute intercept with x=1
68 k = y(1:n-1).*x(1:n-1).^(-m);
69
70 % compute z assuming all slopes are not -1
71 z = k./(m+1).*(x(2:n).^(m+1)-x(1:n-1).^(m+1));
72 % compute z for slopes near -1
73 z(use_ln) = k(use_ln).*(log(x(use_ln+1))-log(x(use_ln)));
74
75 % prepend leading zero
76 z = [0;z];
```

The following Matlab script illustrates the usage of the trapz_loglog function. It

computes the RMS value for the Marscom base and passively attenuated disturbances. The script also plots the PSD and cumulative RMS of the disturbances.

```
function trapz_loglog_usage_example

% marscom disturbance PSD datapoints
marscom_f = [0.005 0.1   2000 20000];
marscom_s = [117e3 117e3 3e-4 3e-4];
% interpolate disturbance PSD between datapoints
marscom_psd = @(f_) interp_loglog(marscom_f,marscom_s,f_);

% create frequency vector
f_min = 0.005;f_max = 20000;
f = logspace(log10(f_min),log10(f_max),50000)';

% compute the Marscom disturbance PSD using trapz_loglog
marscom_base_rms = sqrt(sum(trapz_loglog(f,marscom_psd(f))));
disp(['Marscom Base RMS: ' num2str(marscom_base_rms,'%.0f')]);

% create a simple passive attenuation frequency response
passive_attenuation = @(f_,omega,q) ...
    ( omega/q*(i*2*pi*f_)+omega^2 )./...
    ( (i*2*pi*f_).^2+omega/q*(i*2*pi*f_)+omega^2 );
% propigate base PSD through passive attenuation freq. resp.
optical_table_psd = @(f_,omega,q) marscom_psd(f_).*...
    (passive_attenuation(f_,omega,q).*...
     conj(passive_attenuation(f_,omega,q)));

% compute the optical table disturbance PSD using trapz_loglog
w_n = 5*2*pi;
Q = 8;
optical_table_rms = sqrt(sum(trapz_loglog(f,...
    optical_table_psd(f,w_n,Q))));
disp(['Optical Table RMS: ' num2str(optical_table_rms,'%.0f')]);

```

```
% make plots of PSD and cumulative RMS
figure();clf();
loglog(f,marscom_psd(f),...
       f,optical_table_psd(f,w_n,Q),...
       'LineWidth',1.5);
xlim([min(f) max(f)]);ylim([1e-4 1e6]);grid on;
xlabel('Frequency (Hz)');
ylabel('Power Spectral Density (\murad^2/Hz)');
legend(['MLCD Base: ' num2str(marscom_base_rms,'%.0f') ' \murad RMS'],...
       ['Optical Table: ' num2str(optical_table_rms,'%.0f') ...
        ' \murad RMS, \omega_n=' num2str(w_n,'%.0f') ...
        ' rad/s, Q=' num2str(Q,'%.0f')],...
       'Location','NorthEast');
figure();clf();
semilogx(f,sqrt(cumsum(trapz_loglog(f,marscom_psd(f)))),...
         f,sqrt(cumsum(trapz_loglog(f,optical_table_psd(f,w_n,Q)))),...
         'LineWidth',1.5);
xlim([min(f) max(f)]);grid on;
xlabel('Frequency (Hz)');ylabel('Cumulative RMS (\murad RMS)');
legend(['MLCD Base'],...
       ['Optical Table, \omega_n=' num2str(w_n,'%.0f')...
        ' rad/s, Q=' num2str(Q,'%.0f')],...
       'Location','SouthEast');

end

function yi = interp_loglog(x,y,xi)
% Straight-line interpolation on a log-log scale
yi = 10.^(interp1(log10(x),log10(y),log10(xi),'linear','extrap'));
end
```

Appendix B

Nodal Analysis Matrix

$$\mathsf{A}\boldsymbol{x} = \boldsymbol{z}$$

$$\begin{bmatrix} \mathsf{Y_R} & \mathsf{B} \\ \mathsf{C} & \mathsf{D} \end{bmatrix} \begin{bmatrix} \boldsymbol{V} \\ \boldsymbol{I} \end{bmatrix} = \begin{bmatrix} \boldsymbol{J} \\ \boldsymbol{F} \end{bmatrix}$$

$$\begin{bmatrix} & & & & & & & & -1 & \cdot & \cdot & \cdot \\ & & & & & & & & \cdot & -1 & \cdot & \cdot \\ & & & & & & & & \cdot & \cdot & -1 & \cdot \\ & & & & & & & & \cdot & \cdot & \cdot & -1 \\ & & & & \mathsf{Y_R} & & & & 1 & \cdot & \cdot & \cdot \\ & & & & & & & & \cdot & 1 & \cdot & \cdot \\ & & & & & & & & \cdot & \cdot & 1 & \cdot \\ & & & & & & & & \cdot & \cdot & \cdot & 1 \\ 1 & \cdot & \cdot & \cdot & -1 & \cdot & \cdot & \cdot & \cdot & \cdot & \cdot & \cdot \\ \cdot & 1 & \cdot & \cdot & \cdot & -1 & \cdot & \cdot & \cdot & \cdot & \cdot & \cdot \\ \cdot & \cdot & 1 & \cdot & \cdot & \cdot & -1 & \cdot & \cdot & \cdot & \cdot & \cdot \\ \cdot & \cdot & \cdot & 1 & \cdot & \cdot & \cdot & -1 & \cdot & \cdot & \cdot & \cdot \end{bmatrix} \begin{bmatrix} \mathscr{F}_1 \\ \mathscr{F}_2 \\ \mathscr{F}_3 \\ \mathscr{F}_4 \\ \mathscr{F}_5 \\ \mathscr{F}_6 \\ \mathscr{F}_7 \\ \mathscr{F}_8 \\ \Phi_{-\hat{y}} \\ \Phi_{-\hat{x}} \\ \Phi_{+\hat{y}} \\ \Phi_{+\hat{x}} \end{bmatrix} = \begin{bmatrix} 0 \\ 0 \\ 0 \\ 0 \\ \Phi_{-\hat{x}-\hat{y}} + \Phi_{+\hat{x}-\hat{y}} \\ -\Phi_{-\hat{x}+\hat{y}} - \Phi_{-\hat{x}-\hat{y}} \\ \Phi_{+\hat{x}+\hat{y}} + \Phi_{-\hat{x}+\hat{y}} \\ -\Phi_{+\hat{x}-\hat{y}} - \Phi_{+\hat{x}+\hat{y}} \\ \mathscr{F}_{-\hat{y}} \\ \mathscr{F}_{-\hat{x}} \\ \mathscr{F}_{+\hat{y}} \\ \mathscr{F}_{+\hat{x}} \end{bmatrix}$$

$$
\mathsf{Y}_{\mathsf{R}} = \begin{bmatrix}
\frac{1}{\mathscr{R}_{-\hat{y}T}} & \cdot & \cdot & \cdot & \cdot & \cdot & \cdot & \cdot \\
\cdot & \frac{1}{\mathscr{R}_{-\hat{x}T}} & \cdot & \cdot & \cdot & \cdot & \cdot & \cdot \\
\cdot & \cdot & \frac{1}{\mathscr{R}_{+\hat{y}T}} & \cdot & \cdot & \cdot & \cdot & \cdot \\
\cdot & \cdot & \cdot & \frac{1}{\mathscr{R}_{+\hat{x}T}} & \cdot & \cdot & \cdot & \cdot \\
\cdot & \cdot & \cdot & \cdot & \frac{1}{\mathscr{R}_{-\hat{x}-\hat{y}}} + \frac{1}{\mathscr{R}_{+\hat{x}-\hat{y}}} + \frac{1}{\mathscr{R}_{-\hat{y}B}} & -\frac{1}{\mathscr{R}_{-\hat{x}-\hat{y}}} & \cdot & -\frac{1}{\mathscr{R}_{+\hat{x}-\hat{y}}} \\
\cdot & \cdot & \cdot & \cdot & -\frac{1}{\mathscr{R}_{-\hat{x}-\hat{y}}} & \frac{1}{\mathscr{R}_{-\hat{x}-\hat{y}}} + \frac{1}{\mathscr{R}_{-\hat{x}+\hat{y}}} + \frac{1}{\mathscr{R}_{-\hat{x}B}} & -\frac{1}{\mathscr{R}_{-\hat{x}+\hat{y}}} & \cdot \\
\cdot & \cdot & \cdot & \cdot & \cdot & -\frac{1}{\mathscr{R}_{-\hat{x}+\hat{y}}} & \frac{1}{\mathscr{R}_{-\hat{x}+\hat{y}}} + \frac{1}{\mathscr{R}_{+\hat{x}+\hat{y}}} + \frac{1}{\mathscr{R}_{+\hat{y}B}} & -\frac{1}{\mathscr{R}_{+\hat{x}+\hat{y}}} \\
\cdot & \cdot & \cdot & \cdot & -\frac{1}{\mathscr{R}_{+\hat{x}-\hat{y}}} & \cdot & -\frac{1}{\mathscr{R}_{+\hat{x}+\hat{y}}} & \frac{1}{\mathscr{R}_{+\hat{x}-\hat{y}}} + \frac{1}{\mathscr{R}_{+\hat{x}+\hat{y}}} + \frac{1}{\mathscr{R}_{+\hat{x}B}}
\end{bmatrix}
$$

$$
\begin{bmatrix}
\frac{1}{\mathscr{R}_{-\hat{y}T}} & \cdot & \cdot & \cdot & \cdot & \cdot & \cdot & \cdot & -1 & \cdot & \cdot & \cdot \\
\cdot & \frac{1}{\mathscr{R}_{-\hat{x}T}} & \cdot & \cdot & \cdot & \cdot & \cdot & \cdot & \cdot & -1 & \cdot & \cdot \\
\cdot & \cdot & \frac{1}{\mathscr{R}_{+\hat{y}T}} & \cdot & \cdot & \cdot & \cdot & \cdot & \cdot & \cdot & -1 & \cdot \\
\cdot & \cdot & \cdot & \frac{1}{\mathscr{R}_{+\hat{x}T}} & \cdot & \cdot & \cdot & \cdot & \cdot & \cdot & \cdot & -1 \\
\cdot & \cdot & \cdot & \cdot & \frac{2}{\mathscr{R}_{PM}} + \frac{1}{\mathscr{R}_{-\hat{y}B}} & -\frac{1}{\mathscr{R}_{PM}} & \cdot\cdot & -\frac{1}{\mathscr{R}_{PM}} & 1 & \cdot & \cdot & \cdot \\
\cdot & \cdot & \cdot & \cdot & -\frac{1}{\mathscr{R}_{PM}} & \frac{2}{\mathscr{R}_{PM}} + \frac{1}{\mathscr{R}_{-\hat{x}B}} & -\frac{1}{\mathscr{R}_{PM}} & \cdot & \cdot & 1 & \cdot & \cdot \\
\cdot & \cdot & \cdot & \cdot & \cdot & -\frac{1}{\mathscr{R}_{PM}} & \frac{2}{\mathscr{R}_{PM}} + \frac{1}{\mathscr{R}_{+\hat{y}B}} & -\frac{1}{\mathscr{R}_{PM}} & \cdot & \cdot & 1 & \cdot \\
\cdot & \cdot & \cdot & \cdot & -\frac{1}{\mathscr{R}_{PM}} & \cdot & -\frac{1}{\mathscr{R}_{PM}} & \frac{2}{\mathscr{R}_{PM}} + \frac{1}{\mathscr{R}_{+\hat{x}B}} & \cdot & \cdot & \cdot & 1 \\
1 & \cdot & \cdot & \cdot & -1 & \cdot & \cdot & \cdot & \cdot & \cdot & \cdot & \cdot \\
\cdot & 1 & \cdot & \cdot & \cdot & -1 & \cdot & \cdot & \cdot & \cdot & \cdot & \cdot \\
\cdot & \cdot & 1 & \cdot & \cdot & \cdot & -1 & \cdot & \cdot & \cdot & \cdot & \cdot \\
\cdot & \cdot & \cdot & 1 & \cdot & \cdot & \cdot & -1 & \cdot & \cdot & \cdot & \cdot
\end{bmatrix}
\begin{bmatrix}
\mathscr{F}_1 \\ \mathscr{F}_2 \\ \mathscr{F}_3 \\ \mathscr{F}_4 \\ \mathscr{F}_5 \\ \mathscr{F}_6 \\ \mathscr{F}_7 \\ \mathscr{F}_8 \\ \Phi_{-\hat{y}} \\ \Phi_{-\hat{x}} \\ \Phi_{+\hat{y}} \\ \Phi_{+\hat{x}}
\end{bmatrix}
=
\begin{bmatrix}
0 \\ 0 \\ 0 \\ 0 \\ 2\Phi_{PM} \\ -2\Phi_{PM} \\ 2\Phi_{PM} \\ -2\Phi_{PM} \\ \mathscr{F}_{-\hat{y}} \\ \mathscr{F}_{-\hat{x}} \\ \mathscr{F}_{+\hat{y}} \\ \mathscr{F}_{+\hat{x}}
\end{bmatrix}
$$

THIS PAGE INTENTIONALLY LEFT BLANK

Appendix C

Alternative Ring Armature Topologies

The figures below show potential variations of the ring armature concept.

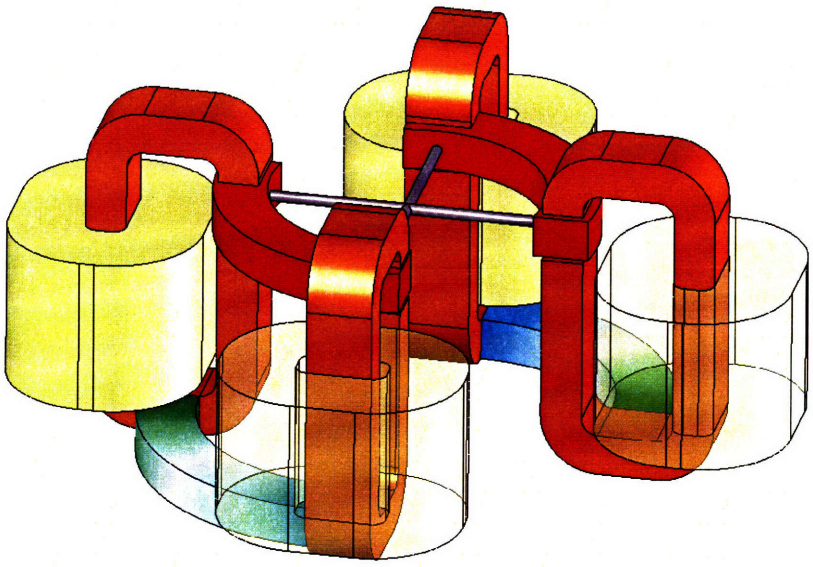

Figure C-1: "Sparse PM" With Deleted Ring Core Segments

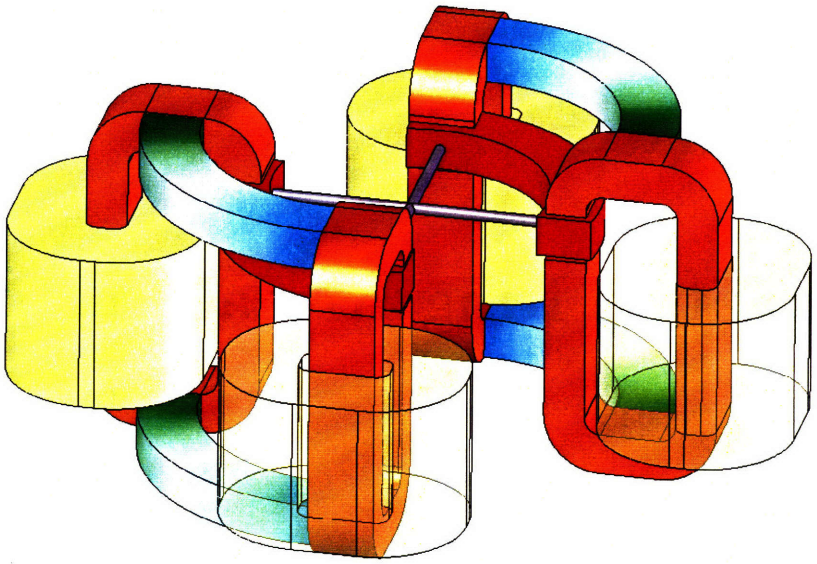

Figure C-2: "Sparse, Two-Level PM" With Deleted Ring Core Segments

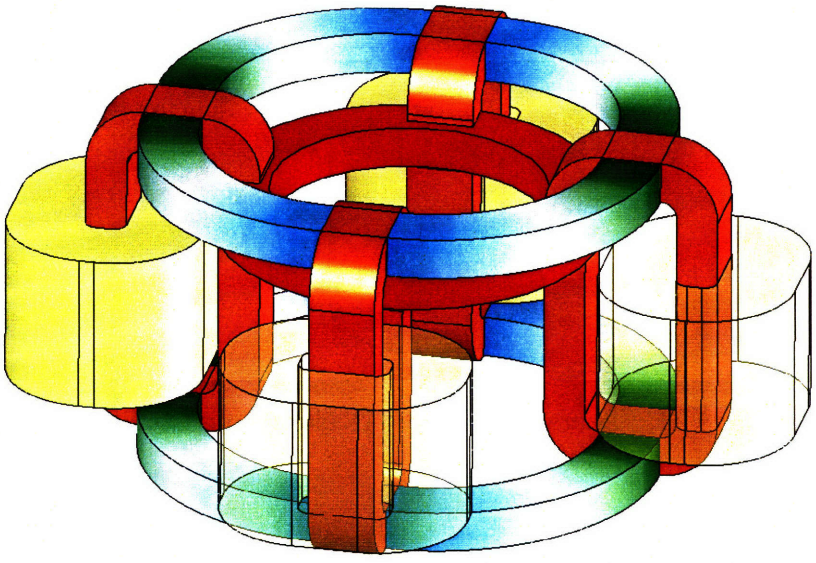

Figure C-3: "Full Two Level PM"

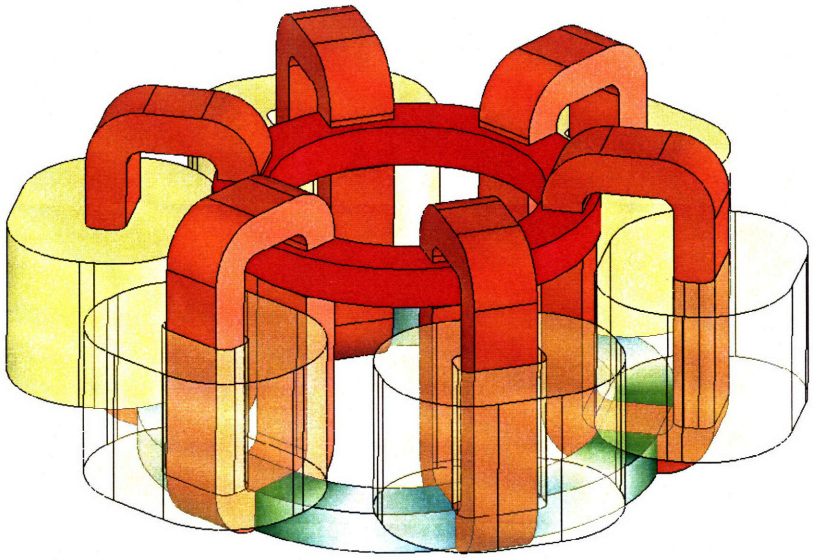

Figure C-4: "Six Pole"

THIS PAGE INTENTIONALLY LEFT BLANK

Appendix D

Armature Mode Shapes

This appendix includes figures of the fourth through the tenth armature mode shapes from the normal modes finite element analysis presented in section 5.5.1.

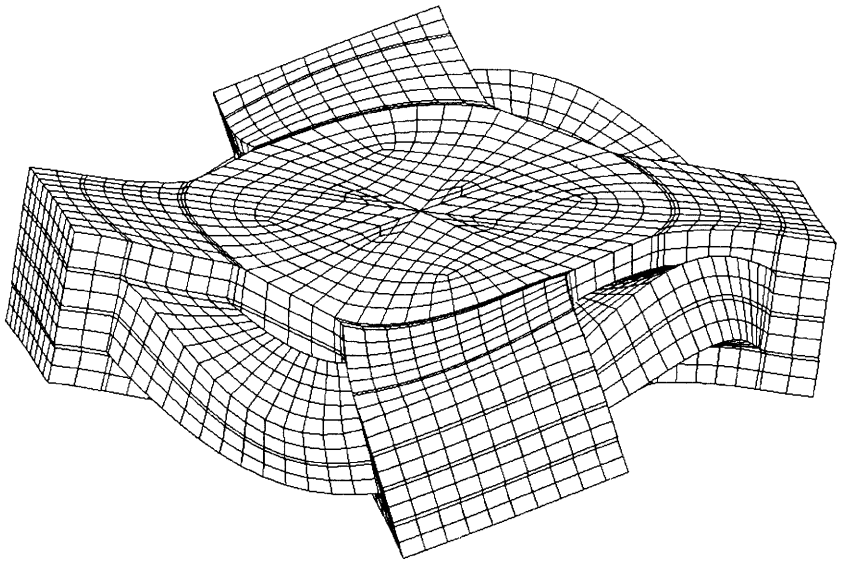

Figure D-1: Modes 4 and 5 (symmetric), Alternately Rotating Wings, 36.6 kHz

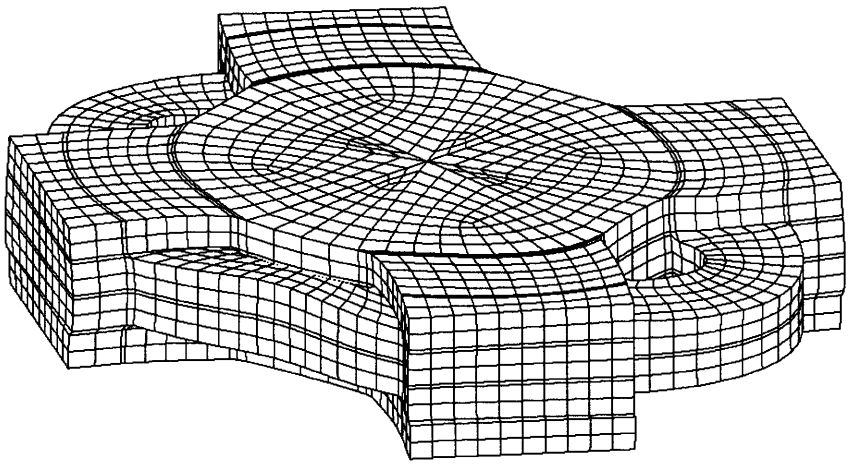

Figure D-2: Mode 6, Squishing About Actuator Axes, 48.3 kHz

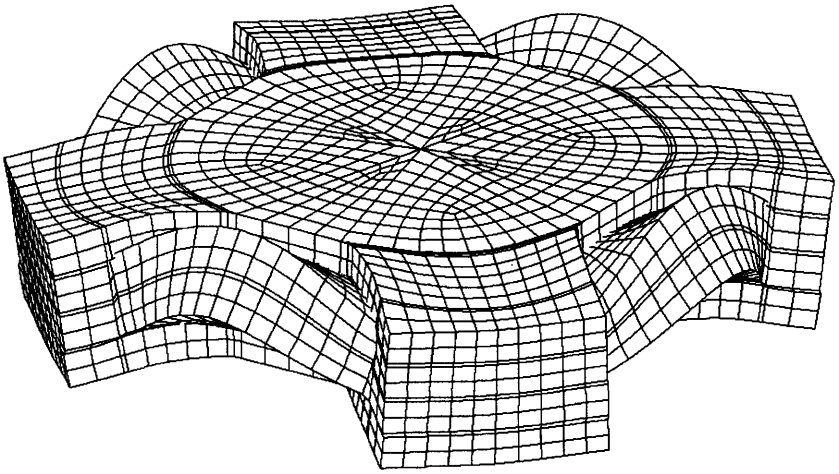

Figure D-3: Mode 7, First Compliant Ring Core Shape, 52.5 kHz

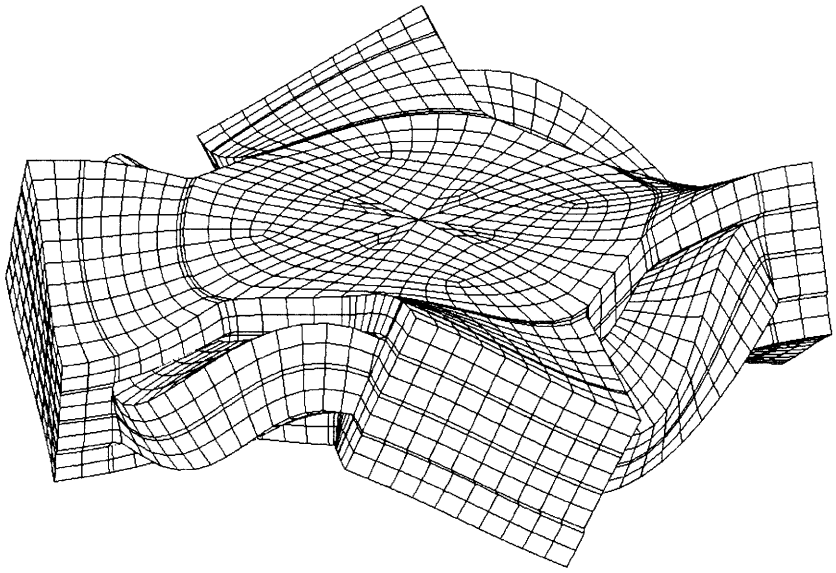

Figure D-4: Mode 8, Commonly Rotating Wings, 54.6 kHz

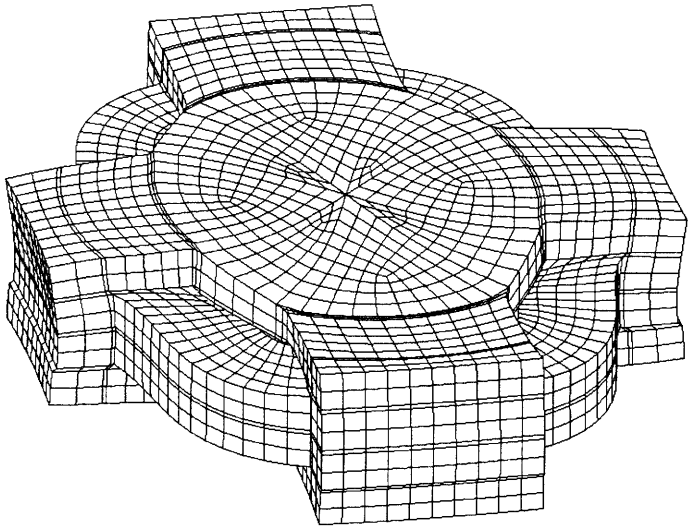

Figure D-5: Mode 9, Squishing About Bearing Axes, 55.1 kHz

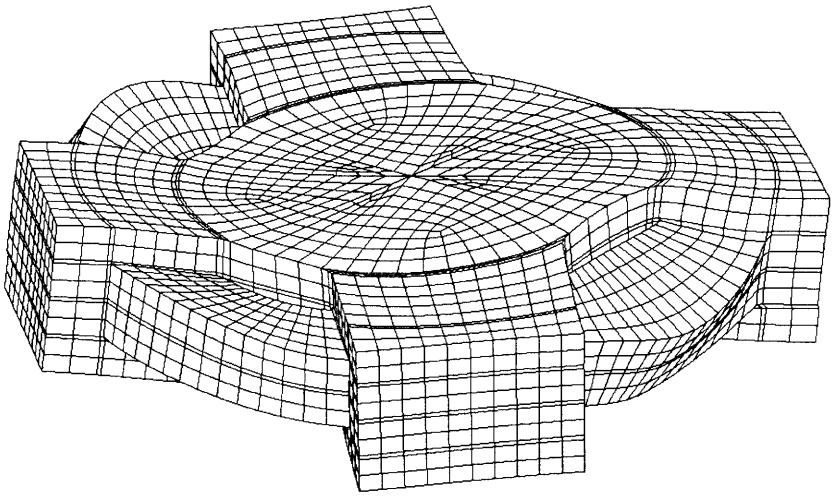

Figure D-6: Mode 10, Second Compliant Ring Core Shape, 59.7 kHz

Bibliography

[1] ASM International. *Properties and Selection: Irons, Steels, and High-Performance Alloys*, 1997.

[2] Mourad Barkat. *Signal Detection and Estimation, Second Edition.* Artech House, 2005.

[3] A. Biswas, D. Boroson, and B. Edwards. Mars laser communication demonstration: what it would have been. In *Free-Space Laser Communication Technologies XVIII*, volume 6105 of *Proceedings of the SPIE*, March 2006.

[4] A. Biswas and S. Piazzolla. Deep-space optical communications downlink budget from mars: System parameters. In Joseph H. Yuen, editor, *The Telecommunications and Data Acquisition Progress Report 42-154, April through June 2003.* Pasadena, August 15 2003. `http://tmo.jpl.nasa.gov/progress_report/42-154/154L.pdf`.

[5] Don M. Boroson, Abhijit Biswas, and Bernard L. Edwards. MLCD: Overview of NASA's Mars laser communications demonstration system. In *Free-Space Laser Communication Technologies XVI*, volume 5338 of *Proceedings of the SPIE*, pages 16–28, June 2004.

[6] Jamie W. Burnside. personal communication, 2006.

[7] J.W. Burnside, D.V. Murphy, F.K. Knight, and F.I. Khatri. A hybrid stabilization approach for deep-space optical communications terminals. *Proceedings of the IEEE*, 95(10):2070–2081, October 2007.

[8] Stephen Butterworth. Eddy-current losses in cylindrical conductors, with special applications to the alternating current resistances of short coils. In *Philosophical Transactions of the Royal Society of London*, volume 222 of *A*, pages 57–100. 1922.

[9] Carpenter Technology Corporation, Wyomissing, PA. *Carpenter High Permeability "49" Alloy.*

[10] David P. Cuff. Electromagnetic nanopositioner. Master's thesis, Massachusetts Institute of Technology, June 2006.

[11] Lloyd Dixon. *2001 Magnetics Design Handbook*, chapter Magnetic Core Characteristics. Texas Instruments, 2001. `http://focus.ti.com/lit/ml/slup124/slup124.pdf`.

[12] Lloyd Dixon. *2001 Magnetics Design Handbook*, chapter Eddy Current Losses in Transformer Windings and Circuit Wiring. Texas Instruments, 2001. `http://focus.ti.com/lit/ml/slup197/slup197.pdf`.

[13] Keith B. Doyle. Structural line-of-sight jitter analysis for MLCD. volume 6665. SPIE, 2007.

[14] Edward P. Furlani. *Permanent Magnet and Electromechanical Devices.* Electromagnetism. Academic Press, San Diego, 2001.

[15] Bernard J. Hamrock, Bo Jacobson, and Steven R. Schmid. *Fundamentals of Machine Elements.* WCB/McGraw-Hill, 1999.

[16] Hamid Hemmati, editor. *Deep Space Optical Communications.* Deep Space Communications and Navigation Series. Jet Propulsion Laboratory, October 2005.

[17] Jack Hitt. The amateur future of space travel. *The New York Times Magazine*, July 1, 2007. `http://www.nytimes.com/2007/07/01/magazine/01nasa-t.html`.

[18] Chung-Wen Ho, A. Ruehli, and P. Brennan. The modified nodal approach to network analysis. *Circuits and Systems, IEEE Transactions on*, 22:504–509, June 1975.

[19] Thanh Hoang, Robert Zwissler, Eric Wiswell, Kenton Ho, and Steve Kuester. TRW's T310 spacecraft bus, a stable alternative for broadband spotbeam. In *20th AIAA International Communications Satellite Systems Conference and Exhibit.* AIAA, May 2002.

[20] Larry Edward Hawe II. Control of a fast steering mirror for laser-based satellite communication. Master's thesis, Massachusetts Institute of Technology, February 2006.

[21] Leon Jabben. *Mechatronic Design of a Magnetically Suspended Rotating Platform.* PhD thesis, Delft University of Technology, December 2007.

[22] Daniel Joseph Kluk. An advanced fast steering mirror for optical communication. Master's thesis, Massachusetts Institute of Technology, June 2007.

[23] FlightStrata 1553E/G. `http://www.lightpointe.com/downloads/datasheets/FlightStrata155E_G.pdf`.

[24] P. B. Lindley. Engineering design with natural rubber. Technical report, The Malaysian Rubber Producers' Research Association, 1970.

[25] Gregory C. Loney. Design and performance of a small two-axis high-bandwidth steering mirror. In *Beam Deflection and Scanning Technology*, volume 1454 of *Proceedings of the SPIE*, pages 198–206, February 1991.

[26] Xiaodong Lu. *Electromagnetically-Driven Ultra-Fast Tool Servos for Diamond Turning.* PhD thesis, Massachusetts Institute of Technology, September 2005.

[27] Augusto E. Barton Martinelli. Rubber bearings for precision positioning systems. Master's thesis, Massachusetts Institute of Technology, September 2005.

[28] David Meeker. Finite element method magnetics version 4.0.1. http://femm.foster-miller.net/wiki/HomePage.

[29] John Lester Miller and Ed Friedman. *Optical Communications Rules of Thumb.* McGraw-Hill, 2003.

[30] MK Magnetics Inc., Adelanto, CA. *Core Specifications.* http://www.mkmagnetics.com/dataSheets/coreSpec.html.

[31] Richard Clement Montesanti. *High Bandwidth Rotary Fast Tool Servos and a Hybrid Rotary=Linear Electromagnetic Actuator.* PhD thesis, Massachusetts Institute of Technology, September 2005.

[32] Normal S. Nise. *Control Systems Engineering.* John Wiley & Sons, 1999.

[33] Harry G. Schaeffer. *MSC/NASTRAN Primer; Static and Normal Modes Analysis.* Wallace Press, Milford, NH, 1982.

[34] J.J. Scozzafava, D.M. Boroson, R.S. Bondurant, Pillsbury A.D., J.W. Burnside, N.W. Spellmeyer, P.L. Ward, F.K. Knight, M.L. Stevens, and D.R. Bold. The Mars lasercom terminal. *LEOS Summer Topical Meetings, 2005 Digest of the,* 25-27 July 2005.

[35] Petre Stoica and Randolph Moses. *Introduction to Spectral Analysis.* Prentice-Hall, 1997.

[36] V. A. Vilnrotter. The effects of pointing errors on the performance of optical communications systems. In N. A. Renzetti, editor, *The Telecommunications and Data Acquisition Progress Report 42-63, March and April 1981*, pages 136–146. Pasadena, June 15 1981. http://tmo.jpl.nasa.gov/progress_report/42-63/63S.PDF.

[37] W. Dan Williams, Michael Collins, Don M. Boroson, James Lesh, Abihijit Biswas, Richard Orr, Leonard Schuchman, and O. Scott Sands. RF and optical communications: A comparison of high data rate returns from deep space in the

2020 timeframe. Technical Report NASA/TM-2007-214459, National Aeronautics and Space Administration, 2007.

[38] Paul Wooster. personal communication, 2007.